Supplementary Information (SI) for Inorganic Chemistry Frontiers.
This journal is © the Partner Organisations 2025

Supporting Information

Mixed Addenda Polyoxometalates by Cooperative Self-Assembly and Modulation of their Optoelectronic Properties

Ganga Singh, Ruchika Choudhary and Debaprasad Mandal*

Department of Chemistry, Indian Institute of Technology Ropar, Rupnagar, Punjab 140001, India
Email: dmandal@iitrpr.ac.in

Experimental Details and Characterizations

$Na_{14}[Fe_4(H_2O)_2(FeW_9O_{34})_2].21H_2O$ (1)

$Na_2WO_4.2H_2O$ (4.00 g, 12.12 mmol) was dissolved in 15 mL DI water. , the pH of the solution was fixed at 7.26 using 6M HCl (precipitate formed during HCl addition were dissolved with vigorous stirring), the resultant solution was placed in a 100 mL Teflon microwave vials of volume and microwave irradiated under controlled pressure with a power ramp for 15 min and power hold for 45 min at 85 °C under 400 W maximum power. To this solution, $FeCl_2.4H_2O$ (0.80 g, 4.04 mmol) was added and irradiated again in the microwave for 1 h at 85 °C following the previous parameters. The orange solution thus obtained was filtered hot, and filtrate was kept for crystallization. After one day, block-shaped orange-colored crystals appeared, which were collected by filtration and dried at 60 °C under vacuum. Yield: 0.84 g (22.8%). FT-IR (cm^{-1}): 931 (W=O_t), 839 (W-O_c-W), 661 (W-O_e-W).

$Na_{10}[Fe_4(H_2O)_2(FeMo_xW_{9-x}O_{34})_2].20H_2O$ (1-M)

A mixture of $Na_2WO_4.2H_2O$ (2.67 g, 8.08 mmol) and $Na_2MoO_4.2H_2O$ (0.98 g, 4.04 mmol) was dissolved in 15 mL DI water. Using 6M HCl, the pH of the solution was fixed at 6.6, the resultant solution was put in Teflon microwave vials of 100 mL volume and microwave irradiated under controlled pressure with a power ramp for 15 min and power hold for 45 min at 85 °C under 400 W maximum power. To this solution, $FeCl_2.4H_2O$ (0.80 g, 4.04 mmol) was added and irradiated again in the microwave for 1 h at 85 °C following the previous parameters. The orange solution thus obtained was filtered hot, and 0.3 g of KCl was added to the filtrate with vigorous stirring. A small amount of precipitate thus formed was filtered, and the final pH of the filtrate was found to be 5.6. After 15 days, block-shaped orange-colored crystals appeared, which were collected by filtration and dried at 60 °C under vacuum. Yield: 0.45 g (13.1%). FT-IR (cm^{-1}): 911 (M=O_t), 832 (M-O_c-M), 678 (M-O_e-M) (M=Mo/W).

$Na_{14}[Zn_2Fe_2^{3+}(H_2O)_2(ZnW_9O_{34})_2].23H_2O$ (2)

$Na_2WO_4.2H_2O$ (4.00 g, 12.12 mmol) was dissolved in 15 mL DI water completely to which 0.5 mL nitric acid was added dropwise (precipitates formed during HNO_3 addition were dissolved with vigorous stirring), the resultant solution was put in Teflon microwave vials and microwave irradiated under controlled pressure with a power ramp for 15 min and hold for 45 min at 85 °C under 400 W maximum power. $Zn(NO_3)_2.6H_2O$ (0.80 g, 2.68 mmol) followed by $Fe(NO_3)_3.9H_2O$ (0.54 g, 1.34 mmol) was added to the above solution with vigorous stirring and irradiated again in the microwave for 1 h at 85 °C, maintaining the previous parameters. The light orange solution thus obtained was filtered hot and filtrate was kept for crystallization. The pH of the final solution was found to be 7.7. After 2 h, block-shaped yellow-colored crystals appeared, which were collected by filtration and dried at 60 °C under vacuum. Yield: 0.73 g (19.6%). FT-IR (cm^{-1}): 917 ($W=O_t$), 839 ($W-O_c-W$), 635 ($W-O_e-W$).

$Na_{14}[Zn_2Fe_2^{3+}(H_2O)_2(ZnMo_xW_{9-x}O_{34})_2].23H_2O$ (2-M)

A mixture of $Na_2WO_4.2H_2O$ (2.00 g, 6.06 mmol) and $Na_2MoO_4.2H_2O$ (1.47 g, 6.06 mmol) in 15 mL DI water was dissolved completely. Using nitric acid, the pH of the solution was fixed at 6.5, the resultant solution was put in Teflon microwave vials and microwave irradiated under controlled pressure with a power ramp for 15 min and power hold for 45 min at 85 °C under 400 W maximum power. $Zn(NO_3)_2.6H_2O$ (0.80 g, 2.68 mmol) followed by $Fe(NO_3)_3.9H_2O$ (0.54 g, 1.34 mmol) was added to the above solution with vigorous stirring and irradiated again in the microwave for 30 min at 85 °C, maintaining the previous parameters. The dark orange solution thus obtained was filtered hot, and filtrate was kept for crystallization. The pH of the final solution was found to be 6.25, from which block-shaped orange-colored crystals appeared after 2 days. These crystals were collected by filtration and dried at 60 °C under vacuum. Yield: 0.67 g (19.3%). FT-IR (cm^{-1}): 913 ($M=O_t$), 840 ($M-O_c-M$), 656 ($M-O_e-M$) (M=Mo/W).

$Na_{14}[Co_2Fe_2^{3+}(H_2O)_2(CoW_9O_{34})_2].15H_2O$ (3)

The synthetic procedure of compound **(2)** was followed with slight modification. In place of $Zn(NO_3)_2.6H_2O$, $Co(NO_3)_2.6H_2O$ (0.78 g, 2.68 mmol) was used. The dark green solution thus obtained was filtered hot, and the filtrate was kept for crystallization. After 2 h, dark green long needle-shaped crystals appeared, which were collected by filtration and dried at 60 °C under vacuum. Yield: 0.89 g (24.7%). FT-IR (cm^{-1}): 904 ($W=O_t$), 838 ($W-O_c-W$), 699 ($W-O_e-W$).

$Na_{14}[Co_2Fe_2^{3+}(H_2O)_2(CoMo_xW_{9-x}O_{34})_2].19H_2O$ (3-M)

The synthetic procedure of compound **(2-M)** was followed with slight modification. $Co(NO_3)_2.6H_2O$ (0.78 g, 2.68 mmol) was used instead of $Zn(NO_3)_2.6H_2O$. The pH of the final solution was found to be 6.3, from which dark colored crystals appeared after 5 days. The crystals were collected by filtration and dried at 60 °C under vacuum. Yield: 0.58 g (17.0%). FT-IR (cm^{-1}): 911 ($M=O_t$), 832 ($M-O_c-M$), 678 ($M-O_e-M$) (M=Mo/W). FT-IR (cm^{-1}): 915 ($M=O_t$), 834 ($M-O_c-M$), 634 ($M-O_e-M$) (M=Mo/W).

$Na_{14}[Zn_2Mn_2^{3+}(H_2O)_2(ZnW_9O_{34})_2].24H_2O$ (4)

A solution of $Na_2WO_4.2H_2O$ (4.00 g, 12.12 mmol) in 15 mL DI water was dissolved completely. Using glacial acetic acid, the pH of the solution was fixed at 7.2, the resultant solution was put in Teflon microwave vials and microwave irradiated under controlled pressure with a power ramp for 15 min and held for 45 min at 85 °C under 400 W maximum power. $Zn(OAc)_2.2H_2O$ (0.58 g, 2.68 mmol), followed by $Mn(OAc)_3.2H_2O$ (0.36 g, 1.34 mmol) was added to the above solution with vigorous stirring and irradiated again in the microwave for 30 min at 85 °C, following previous parameters. The purple solution thus obtained was filtered hot, and filtrate was kept for crystallization. After 2 h, block-shaped purple-colored crystals appeared, which were collected by filtration and dried at 60 °C under vacuum. Yield: 1.13 g (30.3%). FT-IR (cm^{-1}): 918 (W=O_t), 839 (W-O_c-W), 681 (W-O_e-W).

$Na_{14}[Zn_2Mn_2^{3+}(H_2O)_2(ZnMo_xW_{9-x}O_{34})_2].22H_2O$ (4-M)

A mixture of $Na_2WO_4.2H_2O$ (2.67 g, 8.08 mmol) and $Na_2MoO_4.2H_2O$ (0.98 g, 4.04 mmol) was dissolved in 15 mL DI water. The pH of the solution was fixed at 6.5 using glacial acetic acid. The resultant solution was put in Teflon microwave vials and microwave irradiated under controlled pressure with a power ramp for 15 min and power hold for 45 min at 85 °C under 400 W maximum power. $Zn(OAc)_2.2H_2O$ (0.58 g, 2.68 mmol) followed by $Mn(OAc)_3.2H_2O$ (0.36 g, 1.34 mmol) was added to the above solution with vigorous stirring and irradiated again in the microwave for 30 min at 85 °C, maintaining the previous parameters. The resultant solution was filtered hot and the pH of the final solution was found to be 5.8, which was further fixed to 4.5 using glacial acetic acid, then heated at 85 °C with stirring for 30 min. The dark-colored solution gives pink needle-shaped crystals after 1 day. These crystals were collected and dried at 60 °C under vacuum. Yield: 0.82 g (22.9%). FT-IR (cm^{-1}): 914 (M=O_t), 833 (M-O_c-M), 681 (M-O_e-M) (M=Mo/W).

$Na_{14}[Co_2Mn_2^{3+}(H_2O)_2(CoW_9O_{34})_2].22H_2O$ (5)

The synthetic procedure of compound **(4)** was followed with slight modification. In place of $Zn(OAc)_2.2H_2O$, $Co(OAc)_2.2H_2O$ (0.66 g, 2.68 mmol) was used. The pH of the final solution was found to be 6.3, from which dark colored crystals appeared after 5 days. The crystals were collected by filtration and dried at 60 °C under vacuum. Yield: 0.94 g (25.5%). FT-IR (cm^{-1}): 930 (W=O_t), 836 (W-O_c-W), 677 (W-O_e-W).

$Na_{14}[Co_2Mn_2^{3+}(H_2O)_2(CoMo_xW_{9-x}O_{34})_2].19H_2O$ (5-M)

The synthetic procedure of compound **(4-M)** was followed with slight modification. In place of $Zn(OAc)_2.2H_2O$, $Co(OAc)_2.2H_2O$ (0.66 g, 2.68 mmol) was used. The dark green solution thus obtained was filtered hot, and the filtrate was kept for crystallization after fixing the pH of the final solution to 4.5, which gave dark green block-shaped crystals. These crystals were collected by filtration and dried at 60 °C under vacuum. Yield: 0.62 g (17.6%). FT-IR (cm^{-1}): 914 (M=O_t), 834 (M-O_c-M), 677 (M-O_e-M) (M=Mo/W).

$Na_{12}[Fe_4(H_2O)_2(ZnW_9O_{34})_2].23H_2O$ (6)

$Na_2WO_4.2H_2O$ (2.67 g, 8.08 mmol) was dissolved in 15 mL DI water. Using 6M HCl, the pH of the solution was fixed at 7.2, and the resultant solution was put in Teflon microwave vials and irradiated under controlled

pressure with a power ramp for 15 min and power hold for 30 min at 85 °C under 400 W maximum power. $ZnCl_2$ (0.36 g, 2.68 mmol) followed by $FeCl_2.2H_2O$ (0.53 g, 2.68 mmol) was added to the above solution with vigorous stirring and irradiated again in the microwave for 30 min at 85 °C, maintaining the previous parameters. The dark orange solution thus obtained was filtered hot, and filtrate was kept for crystallization. After 1 day, orange-colored octahedral crystals appeared. These crystals were collected by filtration and dried at 60 °C under vacuum. Yield: 0.57 g (15.5%). FT-IR (cm^{-1}): 927 ($W=O_t$), 841 ($W-O_c-W$), 680 ($W-O_e-W$).

$Na_2ZnMo_2[Fe_4(O)_2(ZnMo_xW_{9-x}O_{34})_2].21H_2O$ (6-M)

$Na_2WO_4.2H_2O$ (2.67 g, 8.08 mmol) and $Na_2MoO_4.2H_2O$ (0.97 g, 4.04 mmol) were dissolved in 15 mL DI water. Using 6M HCl, the pH of the solution was fixed at 6.8, and the resultant solution was put in Teflon microwave vials and microwave irradiated under controlled pressure with a power ramp for 15 min and power hold for 30 min at 85 °C under 400 W maximum power. $ZnCl_2$ (0.36 g, 2.68 mmol) followed by $FeCl_2.2H_2O$ (0.53 g, 2.68 mmol) was added to the above solution with vigorous stirring and irradiated again in the microwave for 30 min at 85 °C, maintaining the previous parameters. The dark orange solution thus obtained was filtered hot, and the filtrate was kept for crystallization. After 1 day, block-shaped orange-colored crystals appeared. These crystals were collected by filtration and dried at 60 °C under vacuum. Yield: 0.85 g (24.6%). FT-IR (cm^{-1}): 920 ($M=O_t$), 836 ($M-O_c-M$), 680 ($M-O_e-M$) (M=Mo/W)

$Na_2Fe_6[Co_2Fe_2(H_2O)_2(CoW_9O_{34})_2].20H_2O$ (7)

$Na_2WO_4.2H_2O$ (4.00 g, 12.12 mmol) was dissolved in 15 mL DI water. Using 6M HCl, the pH of the solution was fixed at 7.25, the resultant solution was put in Teflon microwave vials and microwave irradiated under controlled pressure with a power ramp for 15 min and hold for 30 min at 85 °C under 400 W maximum power. $CoCl_2.6H_2O$ (0.63 g, 2.68 mmol) followed by $FeCl_2.4H_2O$ (0.51 g, 2.68 mmol) was added to the above solution with vigorous stirring and irradiated again in the microwave for 30 minutes at 85 °C, maintaining the previous parameters. The dark green solution thus obtained was filtered hot, and filtrate was kept for crystallization. After 2 h, block-shaped green colored crystals appeared, which were collected by filtration and dried at 60 °C under vacuum. Yield: 0.58 g (15.6%). FT-IR (cm^{-1}): 904 ($W=O_t$), 838 ($W-O_c-W$), 699 ($W-O_e-W$).

$ZnMn_5[MnWZn_2(H_2O)_2(ZnW_9O_{34})_2].12H_2O$ (8)

$Na_2WO_4.2H_2O$ (4.00 g, 12.12 mmol) was dissolved in 15 mL DI water. Using 6M HCl, the pH of the solution was fixed at 7.25, the resultant solution was put in Teflon microwave vials and microwave irradiated under controlled pressure with a power ramp for 15 min and hold for 30 min at 85 °C under 400 W maximum power. $ZnCl_2$ (0.36 g, 2.68 mmol) followed by $MnCl_2.4H_2O$ (0.53 g, 2.68 mmol) was added to the above solution with vigorous stirring and irradiated again in the microwave for 30 minutes at 85 °C, maintaining the previous parameters. The orange solution thus obtained was filtered hot, and the filtrate was kept for crystallization. After 2 h, block-shaped purple-colored crystals appeared, which were collected by filtration and dried at 60 °C under vacuum. Yield: 0.74 g (20.5%). FT-IR (cm^{-1}): 914 ($W=O_t$), 862 ($W-O_c-W$), 682 ($W-O_e-W$)

$Na_{14}[(TM_e)_2Fe_2^{3+}(H_2O)_2(ZnW_9O_{34})_2].nH_2O$ (2a/2b/2c/2d for TM_e = Mn/Co/Ni/Cu, n=42/16 for 2c/2d)

$Na_2WO_4.2H_2O$ (4.00 g, 12.12 mmol) was dissolved in 15 mL DI water to which 0.5 mL nitric acid was added dropwise (precipitates formed during HNO_3 addition were dissolved with vigorous stirring). The resultant solution was put in Teflon microwave vials and microwave irradiated under controlled pressure with a power ramp for 15 min and hold for 45 min at 85 °C under 400 W maximum power. $Zn(NO_3)_2.6H_2O$ (0.39 g, 1.34 mmol) was added to the vial with stirring followed by a mixture of $Fe(NO_3)_3.9H_2O$ (0.54 g, 1.34 mmol) and $(TM)Cl_2.xH_2O$(1.34 mmol) (TM=Mn/Co/Ni/Cu) was added to the above solution with vigorous stirring and irradiated again in the microwave for 1 h at 85 °C maintaining the previous parameter. The solution thus obtained was filtered hot, and the filtrate was kept for crystallization. After one day, crystals appeared, which were collected by filtration and dried at 60 °C under vacuum. Yield: 0.74 g (22.2%) when TM=Mn (**2a**); FT-IR (cm^{-1}): 912 (W=O_t), 842 (W-O_c-W), 688 (W-O_e-W)

0.81 g (23.5%) when TM=Co (**2b**); FT-IR (cm^{-1}): 915 (W=O_t), 854, 832 (W-O_c-W), 636 (W-O_e-W)

0.77 g (19.7%) when TM=Ni (**2c**); FT-IR (cm^{-1}): 910 (W=O_t), 845 (W-O_c-W), 679 (W-O_e-W)

0.74 g (17.1%) when TM=Cu (**2d**); FT-IR (cm^{-1}): 915 (W=O_t), 852 (W-O_c-W), 672 (W-O_e-W)

$Na_{14}[Ni_2Fe_2^{3+}(H_2O)_2(ZnMo_xW_{9-x}O_{34})_2].12H_2O$ (2c-M)

A mixture of $Na_2WO_4.2H_2O$ (2.67 g, 8.08 mmol) and $Na_2MoO_4.2H_2O$ (0.97 g, 4.04 mmol) was dissolved in 15 mL DI water. The pH of the solution was fixed at 6.5 using glacial acetic acid. The resultant solution was put in Teflon microwave vials and microwave irradiated under controlled pressure with a power ramp for 15 min and hold for 45 min at 85 °C under 400 W maximum power. $Zn(NO_3)_2.6H_2O$ (0.39 g, 1.34 mmol) was added to the vial with stirring followed by a mixture of $Fe(NO_3)_3.9H_2O$ (0.54 g, 1.34 mmol) and $NiCl_2.6H_2O$ (0.31 g, 1.34 mmol) was added to the above solution with vigorous stirring and irradiated again in the microwave for 1 h at 85 °C maintaining the previous parameter. The dark red solution thus obtained was filtered hot, and the filtrate was kept for crystallization. After one day, red colored block crystals appeared, which were collected by filtration and dried at 60 °C under vacuum. Yield: 0.74 g (19.3%). FT-IR (cm^{-1}): 920 (M=O_t), 836 (M-O_c-M), 680 (M-O_e-M) (M=Mo/W)

$Na_{14}[(TM_e)_2Fe_2^{3+}(H_2O)_2(CoW_9O_{34})_2].nH_2O$ (3a/3b/3c/3d for TM_e = Mn/Ni/Cu/Zn, n=21 for 3c)

The synthetic procedure of compound **(2a)** was followed with slight modification. In place of $Zn(NO_3)_2.6H_2O$, $Co(NO_3)_2.6H_2O$ (0.38 g, 1.34 mmol) was used. The solution thus obtained was filtered hot, and the filtrate was kept for crystallization. After one day, crystals appeared, which were collected by filtration and dried at 60 °C under vacuum. Yield: 0.84 g (25.0%) when TM=Mn (3a), FT-IR (cm^{-1}): 918 (W=O_t), 853, 838 (W-O_c-W), 676 (W-O_e-W)

0.82 g (24.5%) when TM=Ni (3b), FT-IR (cm^{-1}): 914 (W=O_t), 849 (W-O_c-W), 699, 644 (W-O_e-W)

0.87 g (23.7%) when TM=Cu (3c), FT-IR (cm^{-1}): 901 (W=O_t), 849, 828 (W-O_c-W), 638 (W-O_e-W)

0.74 g (22.0%) when TM=Zn (3d). FT-IR (cm^{-1}): 915 (W=O_t), 852, 832 (W-O_c-W), 663 (W-O_e-W)

$Na_{14}[Ni_2Fe_2^{3+}(H_2O)_2(CoMo_xW_{9-x}O_{34})_2].28H_2O$ (3b-M)

A mixture of $Na_2WO_4.2H_2O$ (2.67 g, 8.08 mmol) and $Na_2MoO_4.2H_2O$ (0.97 g, 4.04 mmol) was dissolved in 15 mL DI water. The pH of the solution was fixed at 6.5 using nitric acid. The resultant solution was put in Teflon microwave vials and microwave irradiated under controlled pressure with a power ramp for 15 min and hold for 45 min at 85 °C under 400 W maximum power. $Co(NO_3)_2.6H_2O$ (0.39 g, 1.34 mmol) was added to the vial with stirring followed by a mixture of $Fe(NO_3)_3.9H_2O$ (0.54 g, 1.34 mmol) and $NiCl_2.6H_2O$ (0.31g, 1.34 mmol) was added to the above solution with vigorous stirring and irradiated again in the microwave for 1 h at 85 °C maintaining the previous parameter. The dark colored solution thus obtained was filtered hot, and the filtrate was kept for crystallization. After one day, light green colored block crystals appeared which were collected by filtration and dried at 60 °C under vacuum. Yield: 0.48 g (13.7%). FT-IR (cm^{-1}): 910 ($M=O_t$), 842 ($M-O_c-M$), 682 ($M-O_e-M$) (M=Mo/W).

$Na_{14}[Fe_2Mn_2^{3+}(H_2O)_2(ZnW_9O_{34})_2].25H_2O$ (4a)

A mixture of $Na_2WO_4.2H_2O$ (4.00 g, 12.12 mmol) was dissolved in 15 mL DI water. The pH of the solution was fixed at 6.5 using glacial acetic acid. The resultant solution was put in Teflon microwave vials and microwave irradiated under controlled pressure with a power ramp for 15 min and hold for 45 min at 85 °C under 400 W maximum power. $Zn(NO_3)_2.6H_2O$ (0.39 g, 1.34 mmol) was added to the vial with stirring followed by a mixture of $Mn(OAc)_3.2H_2O$ (0.35 g, 1.34 mmol) and $FeCl_2.4H_2O$ (0.26 g, 1.34 mmol) was added to the above solution with vigorous stirring and irradiated again in the microwave for 1 h at 85 °C maintaining the previous parameter. The dark red solution thus obtained was filtered hot, and the filtrate was kept for crystallization. After one day, red colored block crystals appeared which were collected by filtration and dried at 60 °C under vacuum. Yield: 0.48 g (12.9%). FT-IR (cm^{-1}): 921 ($W=O_t$), 842 ($W-O_c-W$), 681 ($W-O_e-W$).

$Na_{14}[Fe_2Mn_2^{3+}(H_2O)_2(ZnMo_xW_{9-x}O_{34})_2]$ (4a-M)

A mixture of $Na_2WO_4.2H_2O$ (2.67 g, 8.08 mmol) and $Na_2MoO_4.2H_2O$ (0.97 g, 4.04 mmol) was dissolved in 15 mL DI water. The pH of the solution was fixed at 6.5 using glacial acetic acid. The resultant solution was put in Teflon microwave vials and microwave irradiated under controlled pressure with a power ramp for 15 min and hold for 45 min at 85 °C under 400 W maximum power. $Zn(NO_3)_2.6H_2O$ (0.39 g, 1.34 mmol) was added to the vial with stirring followed by a mixture of $Mn(OAc)_3.2H_2O$ (0.35 g, 1.34 mmol) and $FeCl_2.4H_2O$ (0.26 g, 1.34 mmol) was added to the above solution with vigorous stirring and irradiated again in the microwave for 1 h at 85 °C maintaining the previous parameter. The dark red solution thus obtained was filtered hot and the filtrate was kept for crystallization. After one day, red colored block crystals appeared, which were collected by filtration and dried at 60 °C under vacuum. Yield: 0.44 g (14.3%). FT-IR (cm^{-1}): 920 ($M=O_t$), 834 ($M-O_c-M$), 681 ($M-O_e-M$) (M=Mo/W).

Molecular oxygen binding experiment and preparation of Cs-salt of POMs

A Schlenk tube was charged with 10 μmol of POM and 1 mL of toluene and heated at 110 °C for 12 h under 1 atm. O_2 pressure**.** After cooling to room temperature, the mixture was filtered and dried at 80 °C under a vacuum to obtain dioxygen-activated POM characterized via FT-IR and Raman.

A thick-wall glass tube was charged with POM **2** (0.05 g, 0.01 mmol) and dissolved in 1 mL water. To the clear yellowish solution, cesium chloride (0.13 mmol) was added, and the solution became coagulated. After 2 h stirring at room temperature, the solution was filtered. The solid residue was washed with water and dried at 70 °C under high vacuum to get Cs salt of **2** designated Cs[**2**]. Similarly, Cs salts of **2-M**, **3,** and **3-M** were prepared designated as Cs[**2-M**], Cs[**3**] and Cs[**3-M**], respectively.

2. Materials and Methods

Bond Valence Sum (BVS) Calculations: BVS values of selected atoms were calculated using the expression[1]

$$V_i = \sum_j \exp\left(\frac{R_o - R_{ij}}{B}\right)$$

Where V_i is bond valence parameter of atom i, B is a constant equal to 0.37 Å. R_{ij} is variation in bond length between two atoms i and j, R_o is the bond valence parameter of the given pair of atoms. BVS was calculated from the obtained crystal structure of all the synthesized POMs to calculate oxidation state of transition metals and further correlated with oxidation states calculated from the XPS analysis.

Ultraviolet-Visible spectroscopy (**UV-Vis**). UV-visible spectra were recorded in Shimadzu (UV-2600) spectrophotometer. Diffuse reflectance spectra were recorded in Shimadzu UV-2600 using integrating sphere units (ISR-2600). The optical band gap of these crystalline samples was calculated from diffuse reflectance spectroscopy (DRS) using the Kubelka-Munk equation. A graph was plotted between the energy axis and the Kubelka-Munk function as the intersection point between the energy axis and the line obtained by extrapolating the linear portion of the absorption edge in the plot of the Kubelka-Munk function versus energy. The Kubelka-Munk function, $(1 - R)2/2R$, was calculated from the recorded reflectance data, where R is the reflectance of the layer of TMSP. Absorbance was also calculated from the reflectance spectra using the Kubelka-Munk function.

Fourier Transform Infrared spectroscopy (**FT-IR**). FT-IR spectra were recorded in the range of 400−4000 cm^{-1} using Shimadzu spectrometer with a spectral resolution of 4 cm^{-1} and 100 scan.

Thermal gravimetric analysis (**TGA**). Measurements were performed using a Mettler Toledo TGA/DSC 3, STARe System apparatus under nitrogen flow at a heating rate of 10 °C.min^{-1} up to 600 °C. The water of crystallization was determined from the weight loss based on the first derivative plot below 220 °C.

Electrospray ionization mass spectrometry (ESI-MS). The ESI-MS spectra of all the polyoxometalates were recorded on Waters XEVO G2-XS QTOF mass spectrometer. Sample was prepared by adding 2.5 mL of milli-Q water to the sample vial (5-10 mg), sonicated for 10 minutes to obtain a clear solution, and filtered using a syringe filter (organic solvents like acetonitrile should be avoided, which may precipitate POM). The sample was run in the HRMS using **negative ionization** mode in the range of m/z 100-3000 with different z values (single peak/envelope of peaks).

Raman spectra were recorded on a LabRAM HR Evolution Raman spectrometer (Horiba Scientific) in the range of 200-4000 cm^{-1} by using a 532 nm laser as the excitation source.

Energy dispersive X-ray analysis (EDAX) spectra analysis was conducted using a JEOL 7610FPLUS (Jeol, Japan) with detector Oxford Inca X-act. Integrated JEOL Analysis Station software was used for data collection and analysis.

Powder X-ray diffraction (**PXRD**) studies were performed to affirm the phase purity of the compounds over PANalytical's X'Pert Pro MPD with Cu Kα radiation.

X-ray photoelectron spectra (**XPS**) were recorded using a Thermo Scientific NEXSA surface analysis system with a microfocused (400 μm, 72 W, 12000 V) monochromatic Al Kα (1486.6 eV) hemispherical analyzer and 128 channel plate detectors under an ultrahigh vacuum (UHV 8-10 mbar). The XPS was taken using a powder sample on carbon tape. The XPS spectra were calibrated with respect to C (1s) peak at 284.5 eV with a precision of ±2 eV at a pass energy of 20 eV.

Mössbauer spectra were recorded by using a Wissel 1200 spectrometer and a proportional counter. ^{57}Co(Rh) in constant-acceleration mode was used as the radioactive source. Isomer shifts (δ) are given relative to α-iron foil at RT.

Electrochemical studies. Cyclic voltammograms were recorded on a Metrohm Autolab M204 and Nova 2.1.5 software using a standard three-electrode set-up equipped with a 3 mm diameter glassy carbon working electrode (WE), Pt wire counter electrode (CE) and Ag/AgCl/3 M KCl as reference electrode (RE) using 0.2 mM POM @50 mV/s scan rate.

Slurry preparation and catalytic activity- 7 mg of Cs salt of POMs were mixed with 3 mg of carbon black. 0.5 mL of a 3:1 (H_2O: isopropanol) solution was added, and 5 µL of Nafion binder was added to the mixture, which was sonicated for a minimum of 2 h before drop casting on a glassy carbon electrode. For a glassy carbon electrode with a diameter of 3 mm, 5 µL of slurry was used for drop cast and dried under vacuum oven at 50 °C. Linear sweep voltammetry (LSV) was performed using a three-electrode setup where Ag/AgCl/3M KCl (reference electrode), Pt wire (counter electrode), and glassy carbon (working electrode) in 25 mL phosphate buffer (50 mM) at pH 7.1 and a scan rate of 50 mV/s in 0.5 M Na_2SO_4.

Structural description

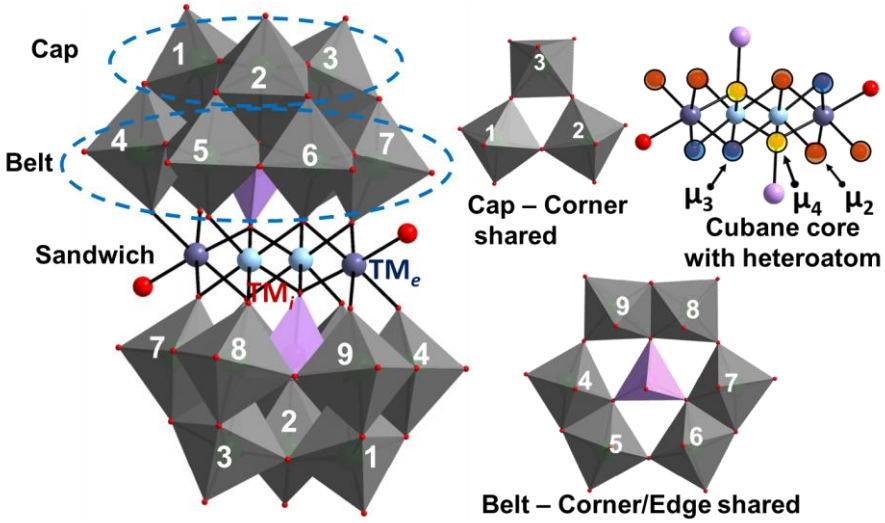

Figure S1. Combined polyhedral/ball and stick representation of tetrasubstituted sandwich POMs showing the position and type of oxygen present (corner/belt shared) as well as internal (TM_i) and external (TM_e) transition metals in sandwich position. μ_2, μ_3, and μ_4 indicate the denticity of the different kinds of oxygen atoms connected to the transition metals.

The 3D structure of these sandwich polyoxometalates can be broken into two parts: (I) tetranuclear cubane framework consisting of 3d transition metals at the sandwich position and (II) the trivacant Keggin framework. The trilacunary Keggin moiety contains a tetrahedrally bound transition metal or P-atom at the center as a templating agent to form triads of addenda W/Mo atoms. Four transition metals in the tetrasubstituted sandwich core are termed internal $\{TM_i\}$ and external atoms $\{TM_e\}$ (Figure S1). Two internal transition metal atoms are connected with the Keggin framework octahedrally via oxygen atoms, while the external transition metal atoms $\{TM_e\}$ are pentacoordinated with the trivacant framework through oxygens, while the sixth coordination is occupied by one water molecule, making it pseudo-octahedral. There are a total of 34 oxygen atoms in the asymmetric unit of these sandwich POMs, of which 6 oxygens are corner shared (O_c), 12 are edge shared (O_e), 9 are terminal oxygens (O_t), and 7 oxygen atoms are bridging transition metals at the sandwich position with the trivacant framework; heteroatoms are tetrahedrally bound through μ_4-oxygens. Both the internal transition metal atoms $\{TM_i\}$ are bound to both sides of the heteroatom through μ_4 oxygens and the framework through μ_2 and μ_3 oxygens, each type of oxygen lying on both sides of the transition metal. However, each external transition metal atom $\{TM_e\}$ is bound to only one side heteroatom through μ4 oxygen, while it is bound to the framework metals through two μ_2 oxygens on one side and two μ_3 oxygens on the opposite side with a water molecule as the sixth coordination site (Figure S1).

Characterizations of 1 and 1-M.

Table S1. Crystal data, data collection, and refinement parameters for 1 and 1-M		
	1	**1-M**
CCDC number	**2330248**	**2330238**
empirical formula	$Fe_6H_{12}Na_{13}O_{107}W_{18}$	$Fe_6K_4Mo_{3.4}Na_{10}O_{98}W_{14.6}$
formula weight	5667.37	5299.81
Temperature/K	273.15	273.15
crystal system	Monoclinic	Monoclinic
space group	$P2_1/n$	$P2_1/n$
unit cell dimension		
a (Å)	13.0961(2)	12.918(14)
b (Å)	17.8110(4)	16.357(18)
c (Å)	21.1982(5)	21.566(2)
α (deg)	90	90
β (deg)	93.5170(10)	104.675(3)
γ (deg)	90	90
V (Å^3)	4935.27(18)	4408.6(8)
Z	2	2
ρ (calculated) (g/cm^3)	3.814	3.992
μ/mm^{-1}	21.91	20.743
F (000)	4998.0	4698.0
crystal size (mm^3)	0.31 × 0.24 × 0.14	0.28 × 0.22 × 0.14
2Θ range for data collection/°	3.85 to 52.81	3.90 to 52.92
index ranges	-16 ≤ h ≤ 16, -22 ≤ k ≤ 22, -26 ≤ l ≤ 26	-16 ≤ h ≤ 16, -20 ≤ k ≤ 20, -26 ≤ l ≤ 27
no. of reflection collected /unique	64932/10134	112852/9084
R(int)	0.057	0.059
GOF on F^2	1.038	1.113
final *R* indices ($I > 2\sigma(I)$)	R1=0.025, wR2=0.060	R1=0.028, wR2=0.074
R indices (all data)	R1=0.031, wR2=0.063	R1=0.029, wR2=0.075
data/restraints/param	10134/1/677	9084/0/623
Largest diff. peak/hole / e Å^{-3}	1.87/-1.24	1.64/-1.71

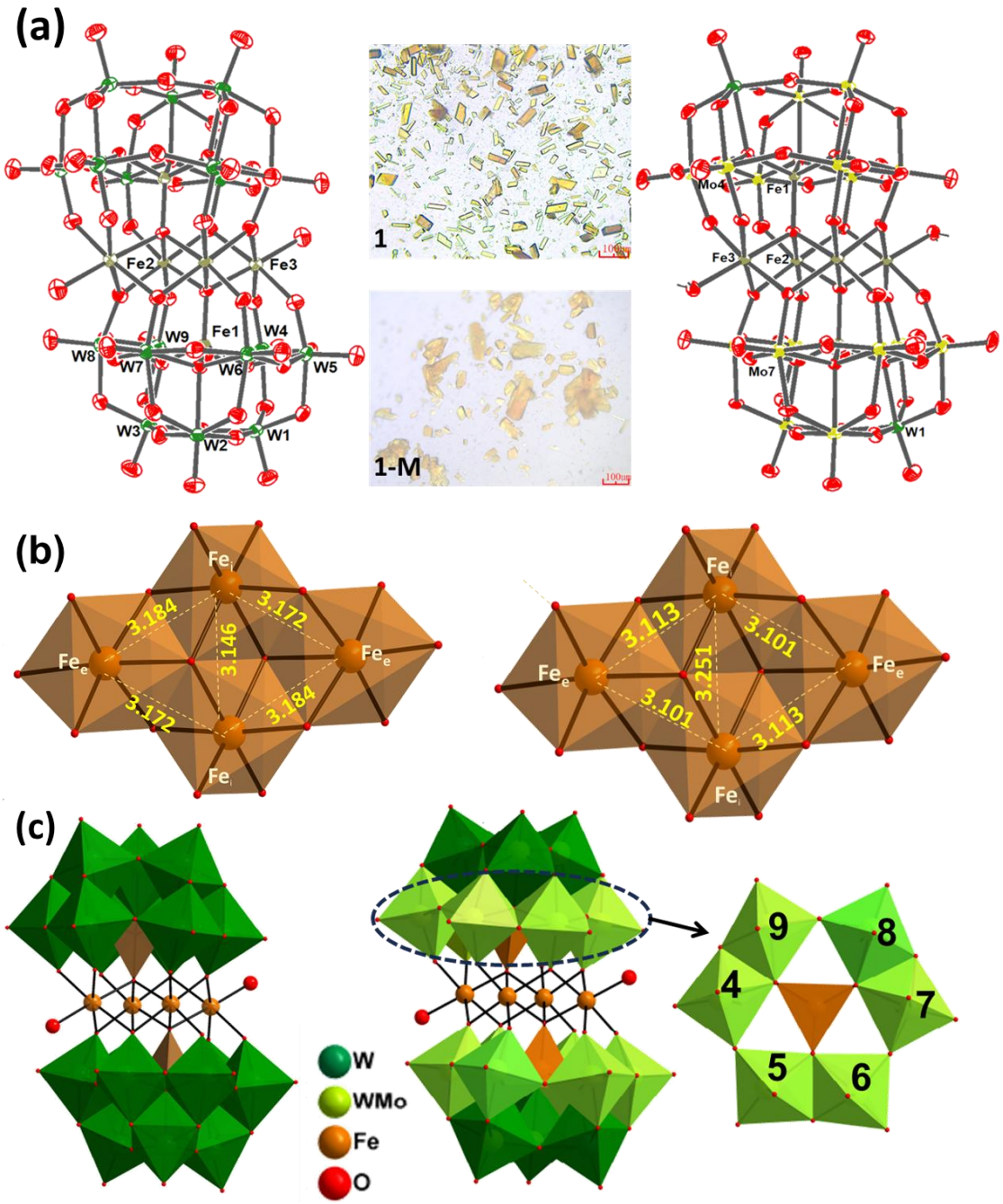

Figure S2. (a) ORTEP drawing (with 60% ellipsoid probability) and Optical images of sandwich POMs; **1** (left) and **1-M** (right); (b) Cubane core showing the interatomic distances between TMs in **1** (left) and **1-M** (right); (c) combined polyhedral/ball and stick representation **1** (left) and **1-M** (right), belt 2 depicting different Mo to W ratios in **1-M**; (Countercations and hydrogen atoms are omitted for clarity).

Table S2. Bond valence parameter (BVS) of selected atoms calculated from the SC-XRD structure **1** and **1-M**			
POMs	**Transition metal**	**Bond valence sum value**	**Oxidation state**
1	W	6.06	+6
	Fe1	3.11	+3
	Fe2	3.03	+3
	Fe3	2.00	+2
1-M	Mo	6.11	+6
	W	6.06	+6
	Fe1	3.02	+3
	Fe2	3.02	+3
	Fe3	3.14	+3

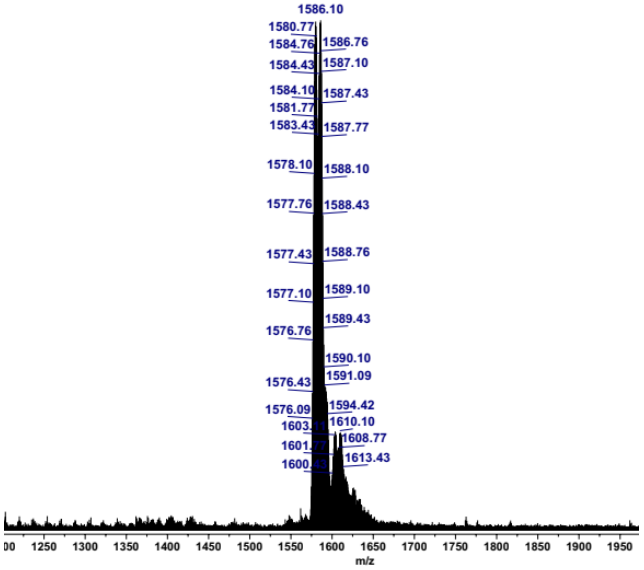

Figure S3. ESI-MS spectra of **1** in the range of m/z 1200-1950 (z=-3).

Table S3. Assignment of ESI-mass peaks of 1

Charge	m/z (obs.)	m/z (calc.)	Mol. Wt.	Assigned probable formula
-3	1580.77	1580.46	4741.40	**$H_9Fe_4(Fe_2W_{18}O_{68})$**
-3	1586.10	1586.47	4759.41	**$H_9Fe_4(Fe_2W_{18}O_{68})(H_2O)$**

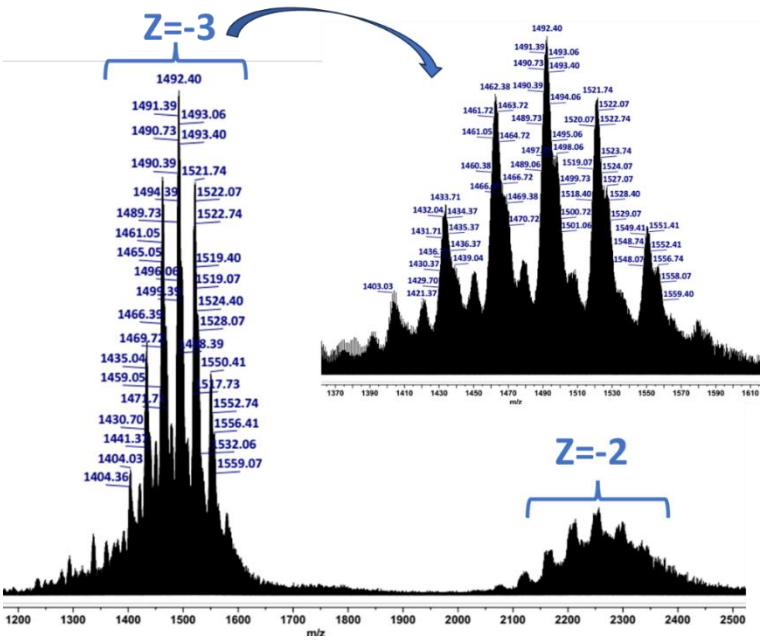

Figure S4. ESI-MS spectra of **1-M** in the range of m/z 1200-2500 for different z values.

Table S4. Assignment of ESI-mass peaks of 1-M

Charge	m/z (obs.)	m/z (calc.)	Mol. Wt.	Assigned probable formula
-3	1550.41	1550.44	4651.34	$H_7Fe_4(Fe_2MoW_{17}O_{68})$
-3	1521.74	1521.10	4563.30	$H_7Fe_4(Fe_2Mo_2W_{16}O_{68})$
-3	1492.40	1491.75	4475.26	$H_7Fe_4(Fe_2Mo_3W_{15}O_{68})$
-3	1462.38	1462.40	4387.22	$H_7Fe_4(Fe_2Mo_4W_{14}O_{68})$
-3	1433.71	1433.06	4299.18	$H_7Fe_4(Fe_2Mo_5W_{13}O_{68})$

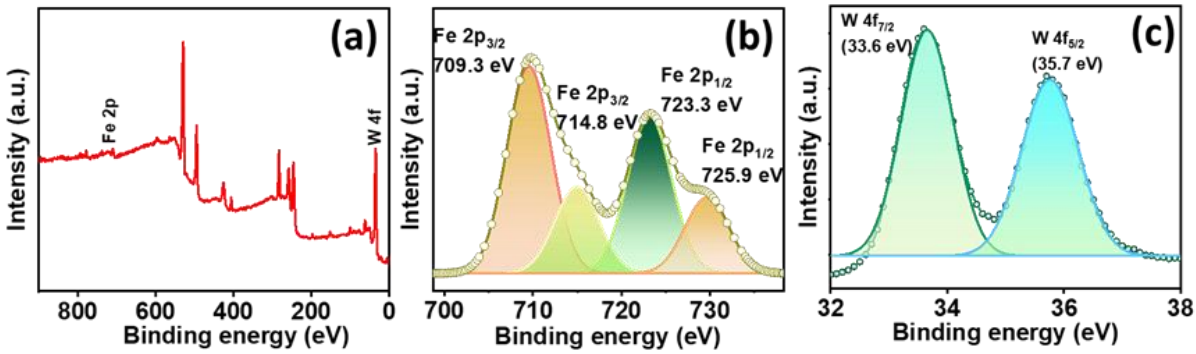

Figure S5. XP spectra of **1** showing (a) Survey spectra, (b) Fe $2p_{3/2}$ and $2p_{1/2}$, (c) W $4f_{7/2}$ and $4f_{5/2}$.

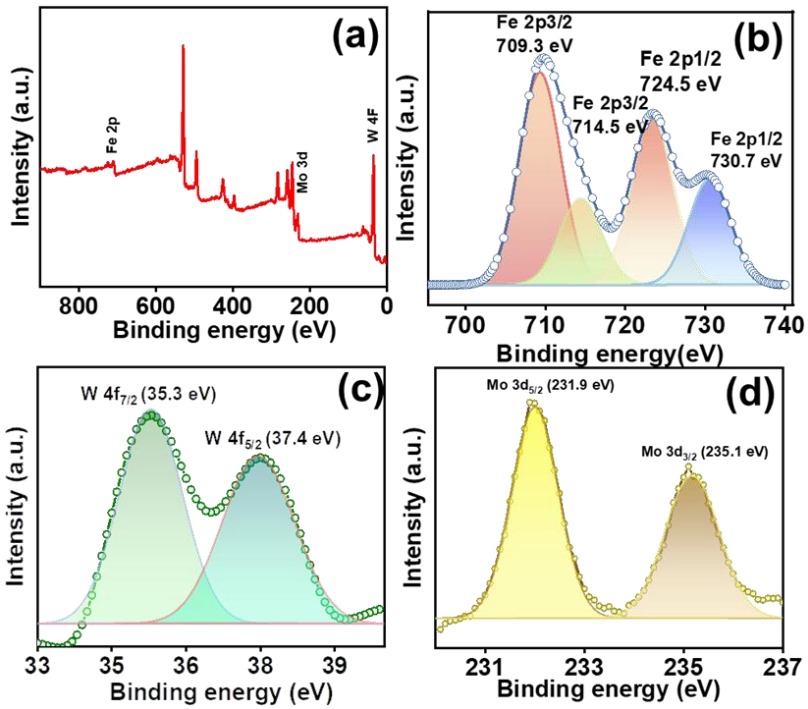

Figure S6. XP spectra of **1-M** showing (a) Survey spectra, (b) Fe $2p_{3/2}$ and $2p_{1/2}$, (c) W $4f_{7/2}$ and $4f_{5/2,}$ (d) Mo $3d_{5/2}$ and $3d_{3/2}$.

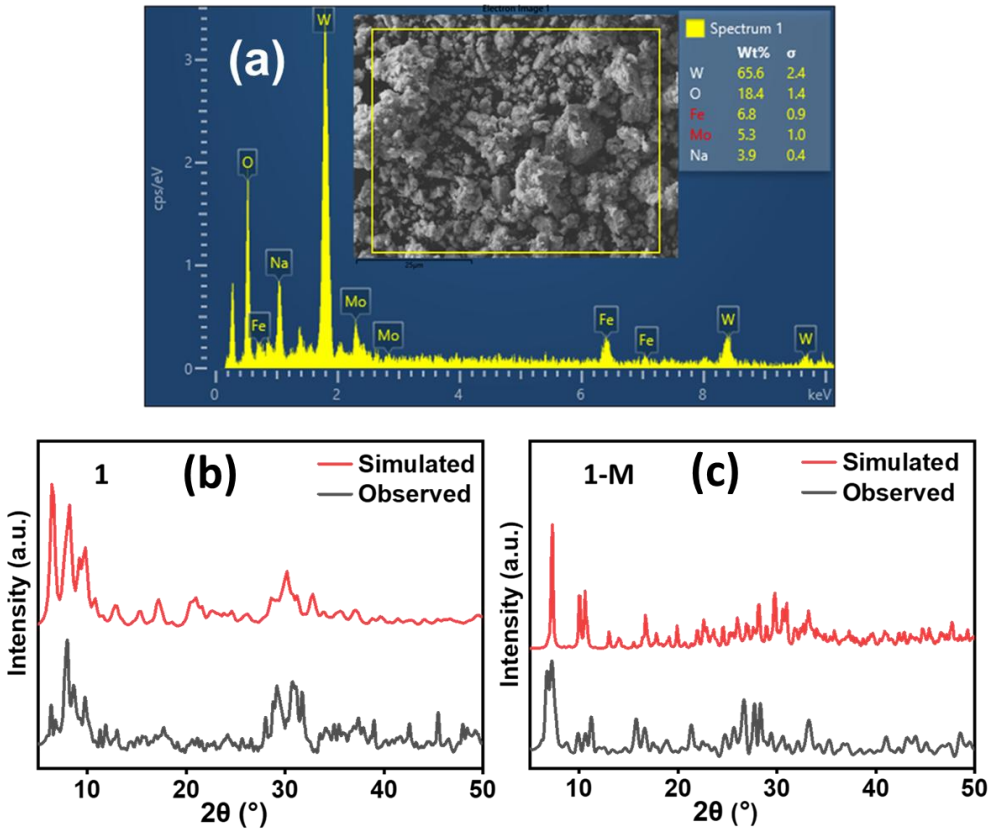

Figure S7. (a) EDX mapping for **1-M**; Observed PXRD pattern and comparison with the simulated data obtained from single crystal XRD (using Mercury software) for (b) **1** (c) **1-M**.

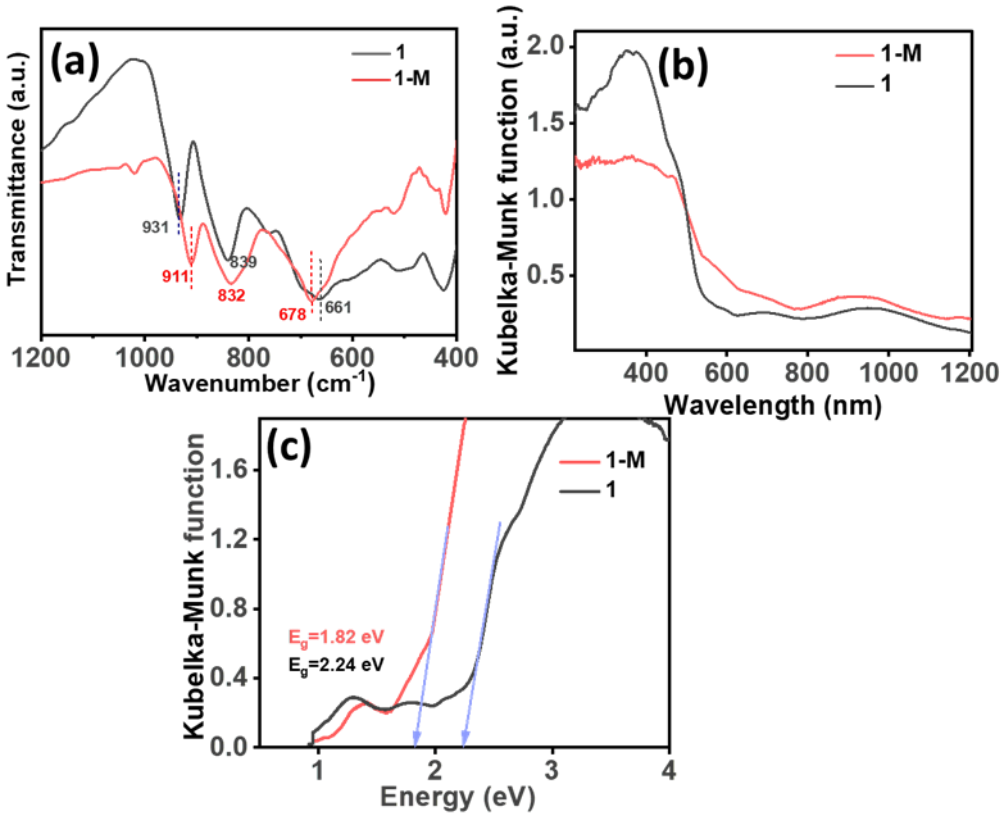

Figure S8. (a) FT-IR, and (b) solid-state UV-vis. spectra and (c) optical band-gap shifting derived from the Kubelka-Munk equation in **1** and **1-M**.

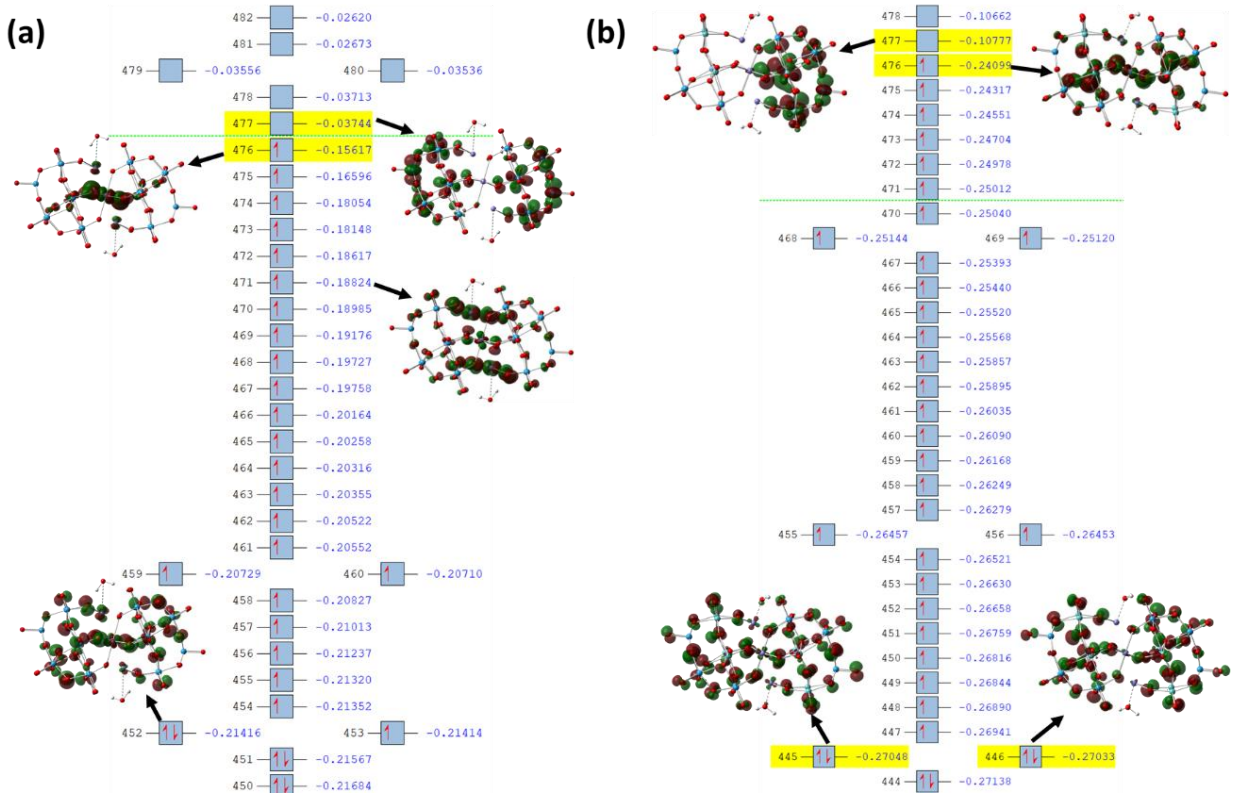

Figure S9. Frontier Molecular orbitals (FMOs) showing HOMOs, LUMOs, and some of the SOMOs of representative structures of (a) **1** and (b) **1-M.**

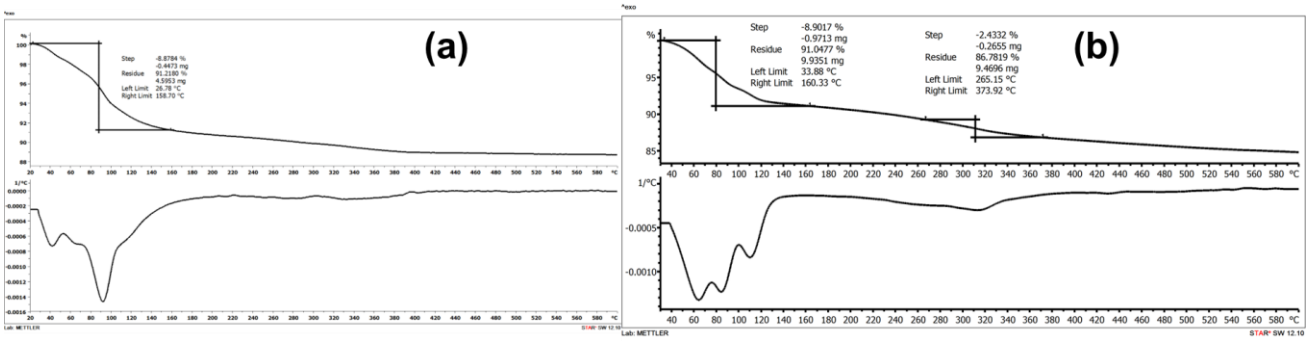

Figure S10. TGA curve along with their first derivative of (a) **1** and (b) **1-M.**

Characterization analysis of 1 and 1-M

Compounds **1** and **1-M** were characterized using TGA, SC-XRD, FT-IR, ESI-MS, XPS and UV-vis spectroscopy (Figure S2-S10). The structure was confirmed by SC-XRD (**CCDC 2330248, 2330238).** The light yellow colored crystals (Figure S2) of **1** and orange crystals of **1-M** crystallize in monoclinic with $P2_1/n$ space group (Table S1). BVS calculation indicates that all addenda atoms are in their +6 oxidation state and Fe in +3 oxidation states in **1-M** while BVS in the case of **1** indicates that Fe in +2 oxidation state at external sandwich position while Fe at internal sandwich position and heteroatom position in +3 oxidation states (Table S2) which was further confirmed from XPS analysis. The XP spectra of **1** revealed the presence of W, Fe, and oxygen (Figure S5), while **1-M** revealed the presence of W, Fe, Mo, and oxygen (Figure S6). Two peaks at 710.3 and 724.3 eV in **1-M** can be attributed to the presence of Fe in a +3 oxidation state, while **1** gives one additional peak at lower side apart from these two peaks, indicating the presence of Fe in +2 oxidation state. The W 4f doublet appears between 33-37 eV, corresponding to W $4f_{7/2}$ and $4f_{5/2}$ in both **1/1-M**. The shift to higher values in **1-M** compared to **1** can be attributed to strong anion-anion interaction in **1-M** due to the less overall negative charge and also due to the presence of Mo in the framework. EDAX demonstrates that all elements are uniformly distributed with bulk composition as $Na_{9.2}Fe_{6.6}Mo_{2.7}W_{19.3}O_{62.3}$ (Figure S7a). From the atom percentage, it is clear that all the elements are in accordance with the ratio of atomic composition of the crystal structure of **1-M**. This has been further confirmed using powder X-ray diffraction analysis (PXRD). The experimental PXRD patterns are consistent with their simulated pattern (Figure S7b, S7c), indicating the phase purity of **1** and **1-M**. From the comparison of $[\{Fe_4(H_2O)_2(FeMo_xW_{9-x})_2\}^{3-}]$, with the reference structure (Figure S1), it is clear that Mo incorporation is favorable at 4/5/9 positions of the belt, which are connected to transition metals in the sandwich position through μ_2 oxygens followed by positions 6 and 8. (Figure S2c). The other positions in the belt as well as in the cap, are comparatively less favorable for Mo incorporation. The distance between Fe atoms in the internal and external positions is 3.18 Å, while it is 3.14 Å between two internal Fe atoms in **1,** however, in **1-M,** the distance between Fe atoms in the internal and external positions is 3.10 Å, while it is 3.24 Å between two internal Fe atoms.

ESI-mass spectrum of **1** in (Figure S3-S4, Table S3-S4) shows the envelope of peaks at m/z 1580.33 (z= –3), while the analog mixed addenda POM shows the isotopic multiple envelopes of peaks attributed to varying ratios of Mo to W. The mixed addenda sandwich POM **1-M** shows the envelopes of peaks in the range of *m*/*z* 1390-1550 for $[\{Fe_4(H_2O)_2(FeMo_xW_{9-x})_2\}^{3-}]$, and *m*/*z* 2100-2400 for $[\{Fe_4(H_2O)_2(FeMo_xW_{9-x})_2\}^{2-}]$. The most

abundant anion in **1-M** has the composition of Mo/W (3:15) with the formula [$\{Fe_4(H_2O)_2(FeMo_{1.5}W_{7.5}O_{34})_2\}^{10-}$], while the Mo/W ratio varies from 1:17 to 5:13 with a constant charge of the cluster, i.e., -10. Comparing the stretching frequencies of tetrasubstituted mixed addenda sandwich POMs with corresponding W-only sandwich POMs, there is a subtle variation in the characteristic peaks (Figure S8a) depending upon the number of Mo atoms incorporated in the framework structure. The FT-IR spectra of **1** show the peaks in the region 650-950 cm^{-1} with characteristic peaks at 931 cm^{-1} (W=O_{term}), 839, 661 cm^{-1} (W-O-W) cm^{-1}. The FT-IR spectra of **1-M** show characteristic peaks similar to **1** in the region 650-950 cm^{-1} with slight shifting due to Mo incorporation in the framework. The M=O_{term} characteristics peaks shift to 911 cm^{-1} while the M-O-M (M=Mo/W) peak shifts to 832 and 678 cm^{-1}, respectively.

Both **1** and **1-M** exhibit broad absorption bands in the UV region due to LMCT (O2p → W5d), while in visible region due to d-d transitions. Moreover, a significant contribution of Mo is evident in **1-M** through a red shift in the UV-vis spectra compared to that of **1** (Figure S8b). This red shift can be explained by the changes in the band gap of these POMs, which were investigated using DRS. It was observed that the band gap reduced to 1.82 eV (**1-M**) from 2.24 eV (**1**). These results were further supported by the DFT study, where the electron density in LUMO shifts to Mo in **1-M** (representative **1-M** formula is taken as $Fe_4(H_2O)_2(FeMo_4W_5)_2\}^{10-}$), while in case of **1** (Figure S9) the electron density lies at W. It was observed that optimization was not feasible with an overall charge of -14/-16 in **1-M**, which also supports our experimental findings, where it was found that all Fe is in a +3 oxidation state, leading to an overall charge of -10. Further, charge -16 in **1** leads to elongation of Fe-O(H_2O) (discussed later). Thus, overall charge as well as the nature of addenda/substituted TM at the sandwich position play crucial roles in defining the redox characteristics of these POMs. Thermal stability was determined by TGA analysis from 30 to 600 °C (Figure S10). The TGA curve of **1** and **1-M** shows high thermal stability up to 600 °C. The first weight loss was observed in the range of 30-160 °C, which was attributed to the release of water of crystallization. Stepwise weight loss indicates lattice and hydrated water molecules in the range 30-160 °C.

Table S5. Some characteristics bond lengths in tetrasubstituted sandwich POMs[2]

Sandwich POMs TM_x-$(TM)_4W_{18}$	**TM_X-O_h**	**$O\mu_4$-TM_i**	**$O\mu_4$-TM_e**	**TM_e-O_c (μ_2 oxygen)**	**O_c-W/Mo**	**Sum of bond lengths X-O_h and $O\mu_4$-TM_i**
Fe-$Fe_2Co_2W_{18}$	1.880	2.024	2.015	2.095	1.774	3.904
Co-$Co_2Bi_2W_{18}$	1.955	2.112	2.016	2.153	1.856	4.067 (distorted)
Cu-Cu_4W_{18}	1.866	2.016	2.022	2.090	1.774	3.872
Fe-$Fe_2Dy_2W_{18}$	1.849	2.049	2.514	2.246	1.772	3.898
Fe-Fe_4W_{18}	1.852	2.048	2.047	1.990	1.803	3.900
Fe-$Fe_2Mn_2W_{18}$	1.848	2.041	2.076	2.033	1.807	3.889
Fe-$Fe_2Ni_2W_{18}$	1.832	2.039	2.034	1.997	1.824	3.871
Ni-Ni_4W_{18}	1.849	2.063	1.992	2.074	1.814	3.912

Zn-$Zn_2Bi_2W_{18}$	1.944	2.164	2.076	2.178	2.326	4.108 (distorted)
Zn-$Ru_2Zn_2W_{18}$	1.932	2.033	2.060	2.072	1.769	3.965
Zn-WZn_3W_{18}	1.930	2.039	2.043	2.070	1.768	3.969
Zn-$WZnMn_2W_{18}$	1.936	2.025	2.142	2.114	1.780	3.961
Co-WCo_3W_{18}	1.938	2.030	2.049	2.074	1.771	3.968
Zn-$WZnCo_2W_{18}$	1.927	2.048	2.051	2.062	1.782	3.975
Zn-$WZnNi_2W_{18}$	1.923	2.019	2.022	2.043	1.771	3.942
Zn-$WZnCu_2W_{18}$	1.936	2.063	2.069	2.079	1.757	3.999
TM_X = transition metal/P at heteroposition, TM_i = transition metal at internal sandwich position, $O\mu_4$ = tetradentate oxygen ligand between heteroatom and transition metal, TM_e = transition metal at external position, O_c = corner shared oxygen						

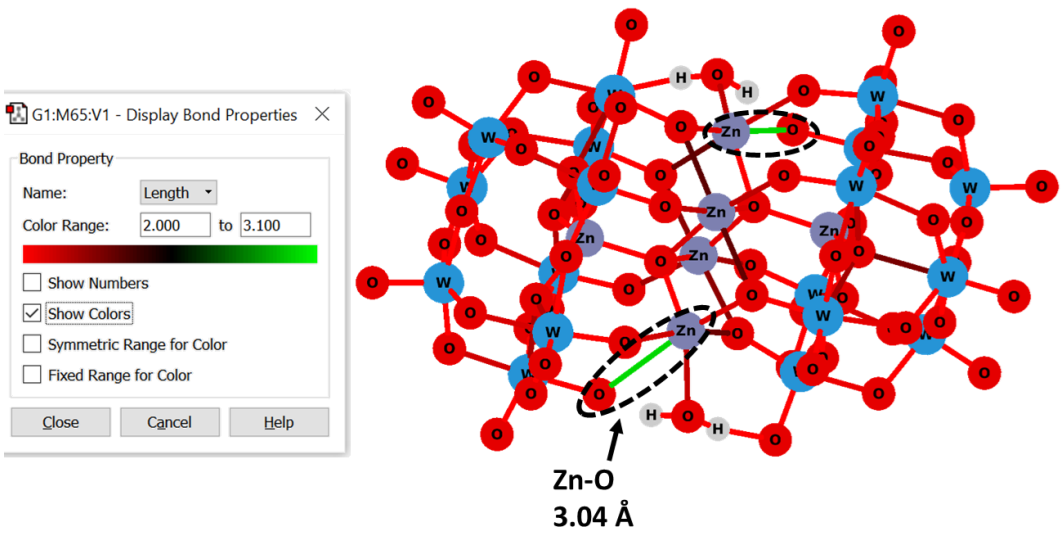

Figure S11. DFT optimized auxiliary structure of Zn-based POM [$\{Zn_4(H_2O)_2(ZnW_9O_{34})_2\}^{16-}$] (elongated bond length shown in green).

Characterizations of 2 and 2-M/2-M(a).

Table S6. Crystal data, data collection, and refinement parameters for **2** and **2-M/2-M(a)**

	2	**2-M**	**2-M(a)**
CCDC number	**2330240**	**2330247**	**2330252**
empirical formula	$Fe_2Na_{15}O_{104}W_{18}Zn_4$	$Fe_6H_{56}K_4Mo_{5.4}Na_{24}O_{196}W_{30.6}Zn_6$	$Fe_3Mo_{1.74}Na_{12}O_{107}W_{16.26}Zn_3$
formula weight	5691.33	10771.81	5507.88
temp (K)	273.15	273.15	273.15
crystal system	triclinic	monoclinic	monoclinic
space group	$P\bar{1}$	$P2_1/n$	$P2_1/n$
unit cell dimension			
a (Å)	12.387(3)	12.893(5)	13.139(14)
b (Å)	13.829(4)	16.492(6)	17.749(15)
c (Å)	14.867(4)	21.624(7)	21.146(2)
α (deg)	98.891(7)	90	90
β (deg)	104.161(6)	104.660(10)	93.601(4)
γ (deg)	102.461(7)	90	90
V (Å^3)	2352.7(10)	4448.4(3)	4921.6(8)
Z	1	1	2
ρ (calculated) (g/cm^3)	4.017	4.021	3.717
μ/mm^{-1}	23.392	21.600	20.448
F (000)	2501.0	4791.0	4865.0
crystal size (mm^3)	0.77 x 0.17 x 0.15	0.35 x 0.27 x 0.17	0.24 × 0.23 × 0.13
2Θ range data/°	4.75 to 52.88	4.09 to 52.85	3.86 to 52.85
index ranges	$-15 \le h \le 15$, $-17 \le k \le 17$, $-18 \le l \le 18$	$-16 \le h \le 16$, $-20 \le k \le 20$, $-26 \le l \le 25$	$-16 \le h \le 16$, $-22 \le k \le 22$, $-26 \le l \le 26$
no. of reflection collected /unique	60927/9610	47592/9082	72728/10109
GOF on F^2	1.085	1.094	1.054
R(int)	0.050	0.047	0.066
final *R* indices ($I > 2\sigma(I)$)	R1=0.0280, wR2=0.0742	Rl=0.0283, wR2=0.0677	R_1 = 0.0329, wR_2 = 0.0832
R indices (all data)	R1=0.0288, wR2=0.0748	R1=0.0319, wR2=0.0694	R_1 = 0.0400, wR_2 = 0.0877
data/restraints/param	9610/0/710	9082/0/641	10109/0/659
Largest diff. peak/hole / e Å^{-3}	2.01/-1.51	1.70/-1.27	2.84/-1.53

Table S7. BVS of selected atoms calculated from the SC-XRD structure of **2** and **2-M.**			
POMs	**Transition metal**	**Bond valence sum value**	**Oxidation state**
2	W	6.04	+6
	Fe1	3.08	+3
	Zn1	2.06	+2
	Zn2	2.23	+2
2-M	Mo	6.15	+6
	W	6.04	+6
	Zn1	2.50	+2
	Zn2	2.34	+2
	Fe1	3.10	+3
	Fe2	3.03	+3

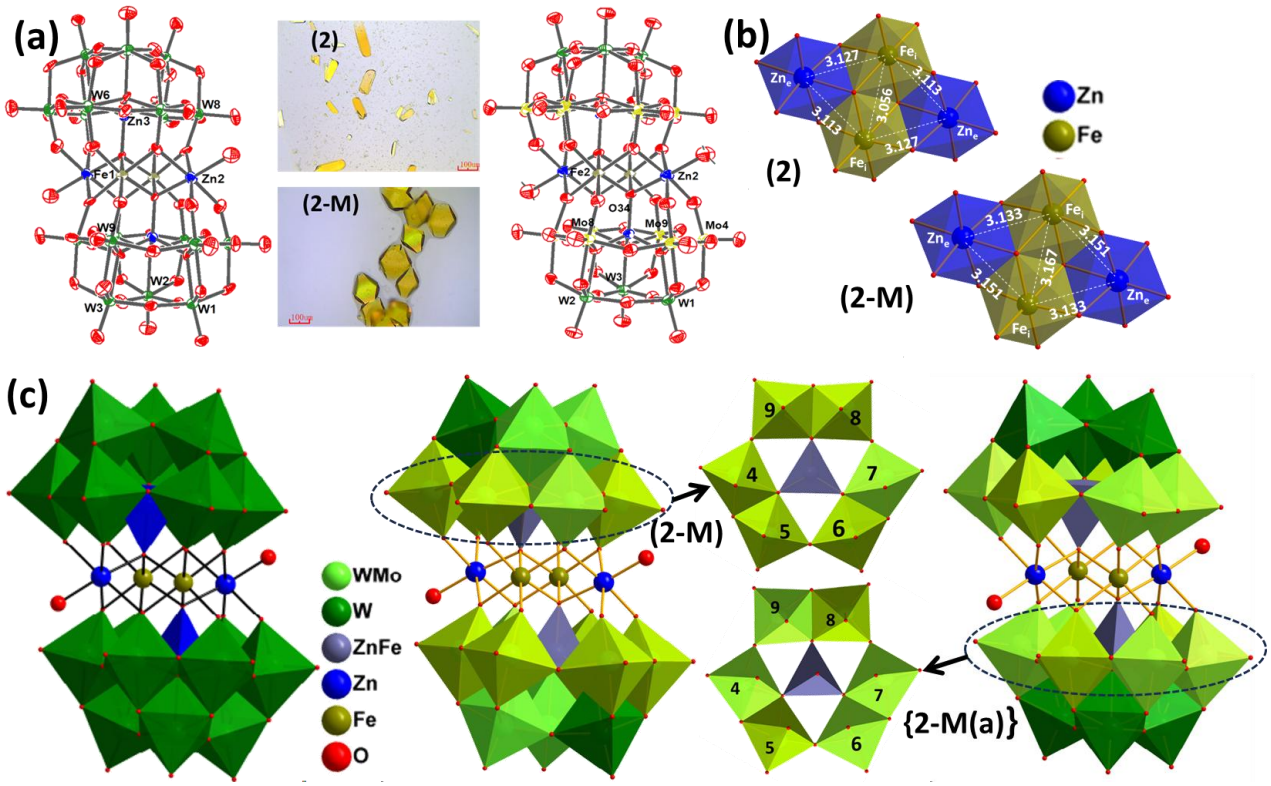

Figure S12. (a) ORTEP drawing (with 60% ellipsoid probability) and Optical images of sandwich POMs; **2** (left) and **2-M** (right); (b) Cubane core showing the interatomic distance between transition metals in **2** (left) and **2-M** (right); (c) combined polyhedral/ball and stick representation of the single-crystal X-ray structure of polyoxometalate **2**(left) and **2-M/2-M(a)** (right), belt 2 depicting different ratios of molybdenum to tungsten in **2-M/2-M(a)**; Countercations and hydrogen atoms are omitted for clarity.

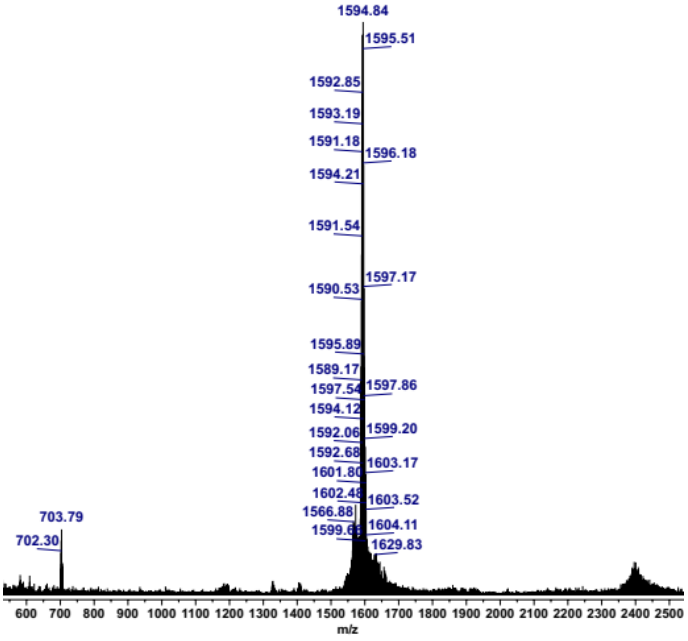

Figure S13. ESI-MS spectra of **2** in the range of m/z 1000-2500 for different z values.

Table S8. Assignment of ESI-mass peaks of 2

Charge	m/z (obs.)	m/z (calc.)	Mol. Wt.	Assigned probable formula
-3	1594.84	1593.79	4762.39	$H_{11}Zn_2Fe_2(Zn_2W_{18}O_{68})$
-2	2412.64	2413.17	4826.34	$H_{10}Na_2Zn_2Fe_2(Zn_2W_{18}O_{68})$

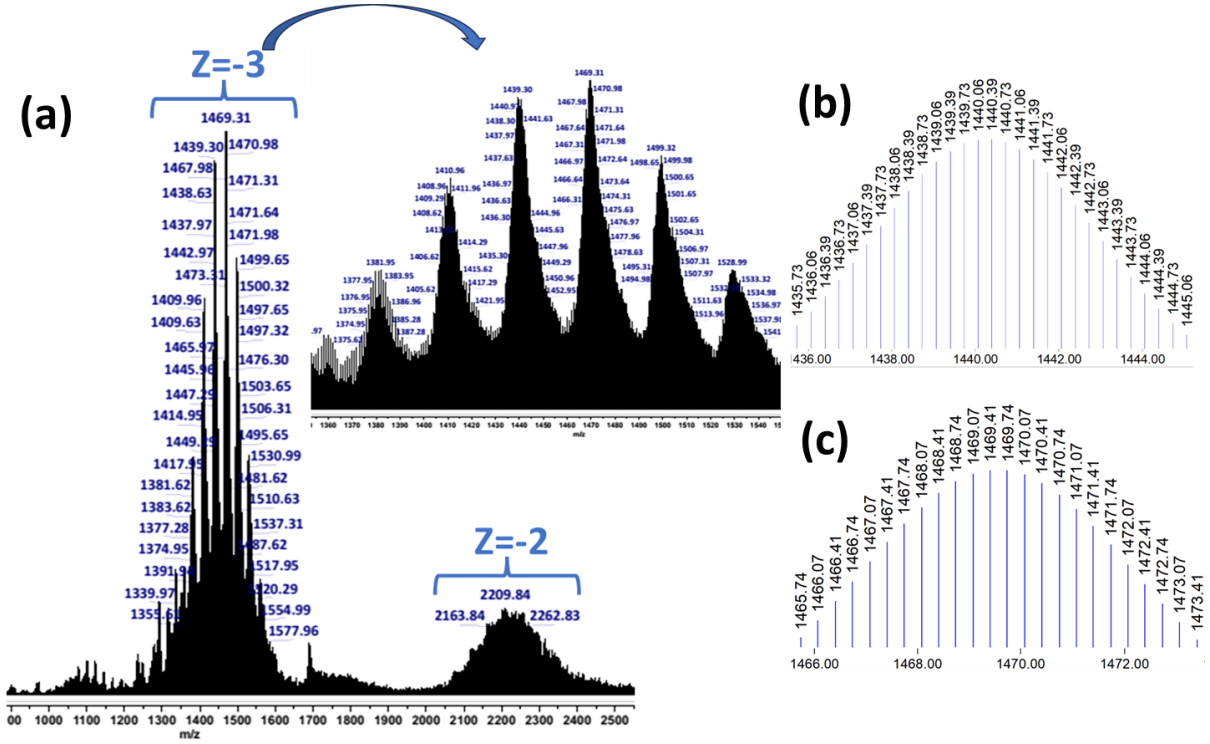

Figure S14. ESI-MS spectra of **2-M** in the range of m/z 1000-2500 for different z values; (b) and (c) corresponding simulated mass spectra of two envelopes of peaks.

Assignment of ESI-mass peaks of 2-M				
Charge	**m/z (obs.)**	**m/z (calc.)**	**Mol. Wt.**	**Assigned probable formula**
-3	1559.66	1560.77	4682.33	$H_{10}Zn_2Fe_2(ZnFeMoW_{17}O_{68})$
-3	1528.99	1528.10	4584.30	$H_9Zn_2Fe_2(Fe_2Mo_2W_{16}O_{68})$
-3	1499.32	1498.75	4496.26	$H_9Zn_2Fe_2(Fe_2Mo_3W_{15}O_{68})$
-3	1469.31	1469.40	4408.22	$H_9Zn_2Fe_2(Fe_2Mo_4W_{14}O_{68})$
-3	1439.30	1440.39	4321.18	$H_9Zn_2Fe_2(Fe_2Mo_5W_{13}O_{68})$
-3	1410.96	1411.04	4233.14	$H_9Zn_2Fe_2(Fe_2Mo_6W_{12}O_{68})$
-3	1381.95	1381.70	4145.10	$H_9Zn_2Fe_2(Fe_2Mo_7W_{11}O_{68})$

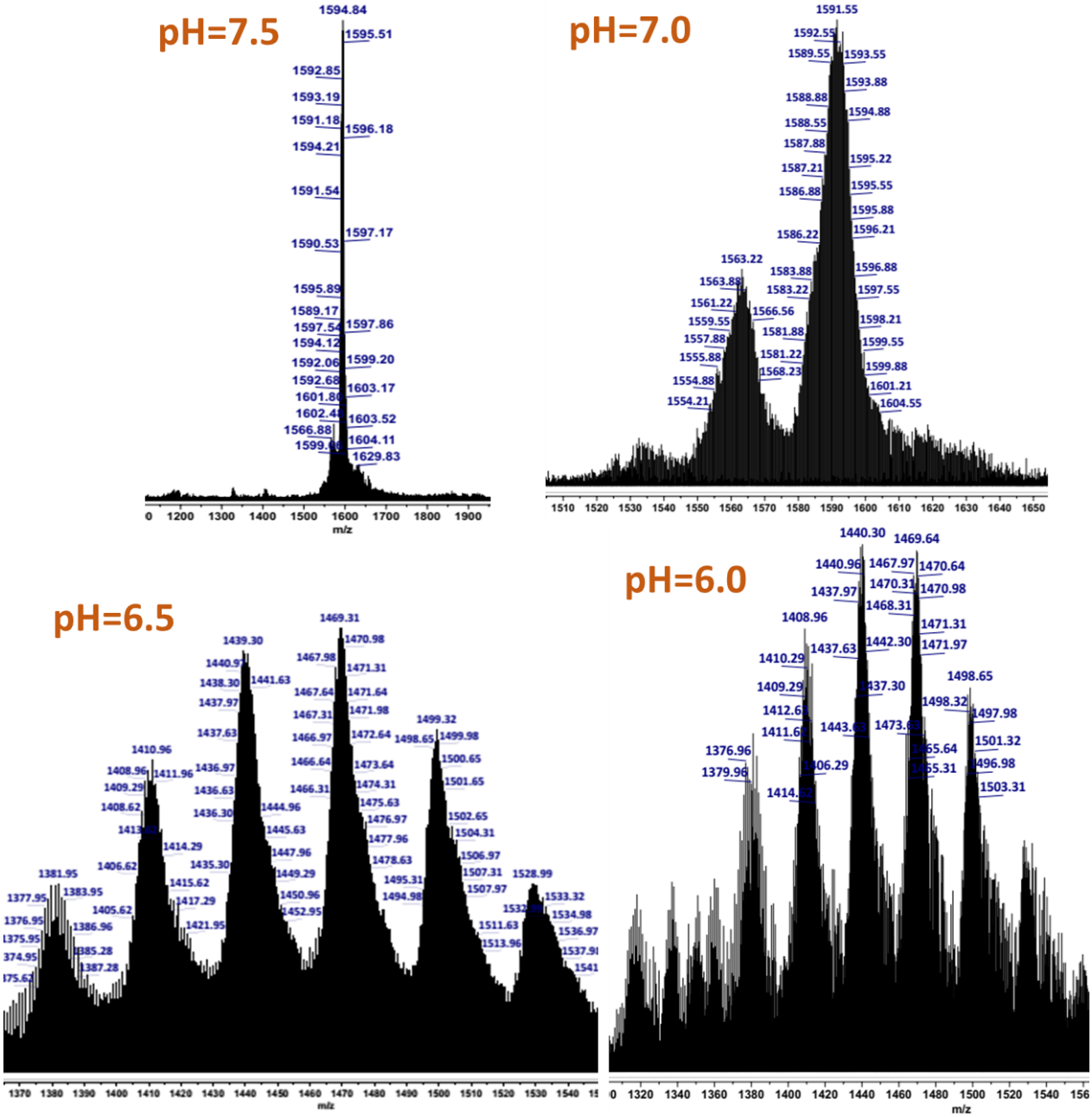

Figure S15. pH-dependent ESI-MS spectra of **2-M** with charge (z) = –3

Table S10. Assignment of ESI-mass peaks of **2-M** (pH-dependent study)

Charge	m/z (obs.)	m/z (calc.)	Mol. Wt.	Assigned probable formula
-3	1594.84	1593.79	4781.37	$H_{11}Zn_2Fe_2(Zn_2W_{18}O_{68})$
-3	1590.55	1590.12	4770.37	$H_{10}Zn_2Fe_2(Zn_2MoW_{17}O_{68})$
-3	1560.33	1560.77	4682.33	$H_{10}Zn_2Fe_2(ZnFeMoW_{17}O_{68})$
-3	1528.99	1528.10	4584.30	$H_{10}Zn_2Fe_2(Fe_2Mo_2W_{16}O_{68})$
-3	1498.32	1498.75	4496.26	$H_9Zn_2Fe_2(Fe_2Mo_3W_{15}O_{68})$
-3	1469.65	1469.40	4408.22	$H_9Zn_2Fe_2(Fe_2Mo_4W_{14}O_{68})$
-3	1440.30	1440.39	4321.18	$H_9Zn_2Fe_2(Fe_2Mo_5W_{13}O_{68})$
-3	1410.96	1411.04	4233.14	$H_9Zn_2Fe_2(Fe_2Mo_6W_{12}O_{68})$
-3	1380.96	1381.70	4145.10	$H_9Zn_2Fe_2(Fe_2Mo_7W_{11}O_{68})$

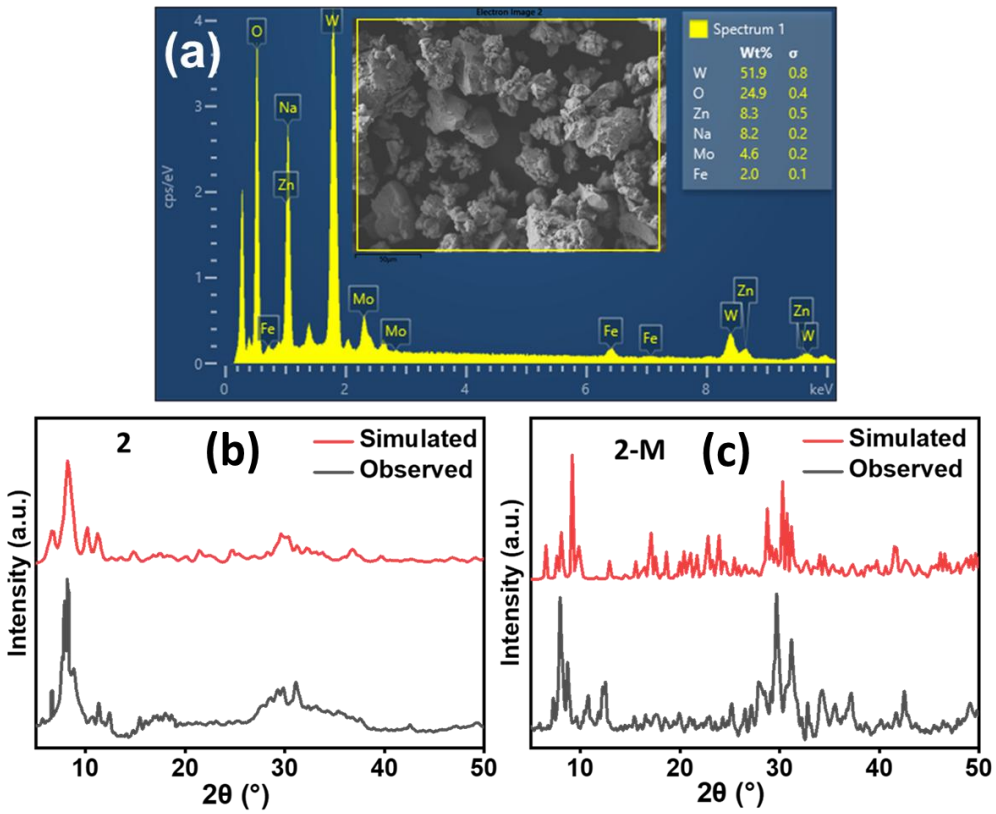

Figure S16. (a) EDX mapping for **2-M**; Observed PXRD pattern and comparison with the simulated data obtained from single crystal XRD for (b) **2** (c) **2-M**.

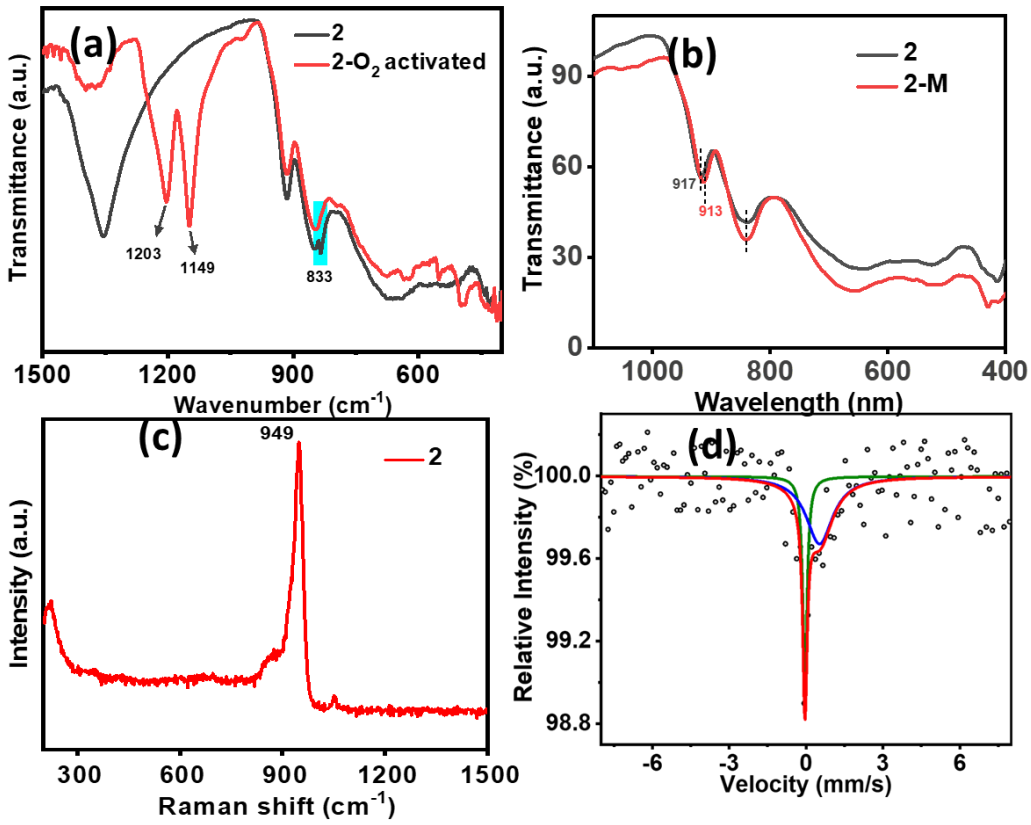

Figure S17. FT-IR spectra of (a) **2** before and after O_2 treatment in toluene**;** (b) FT-IR of **2** and **2-M**; (c) Raman spectra of **2**; (d) ^{57}Fe Mössbauer spectrum of **2-M**.

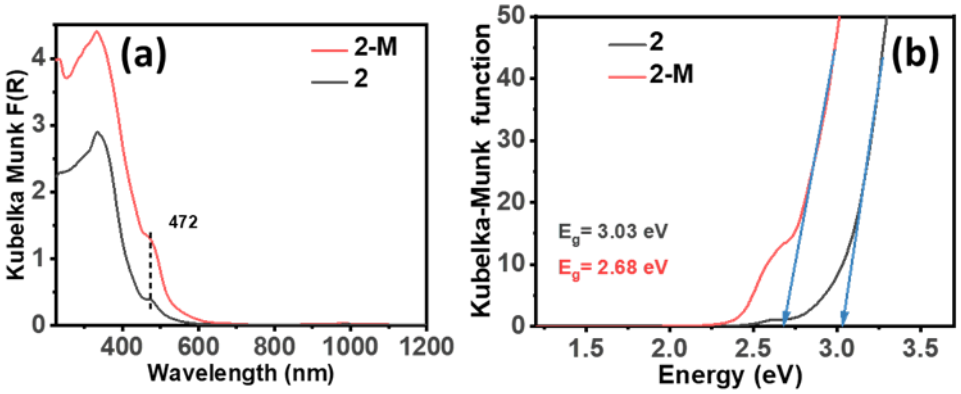

Figure S18. (a) solid-state UV-vis spectra and (b) optical band-gap shifting derived from the Kubelka-Munk equation in **2** and **2-M**.

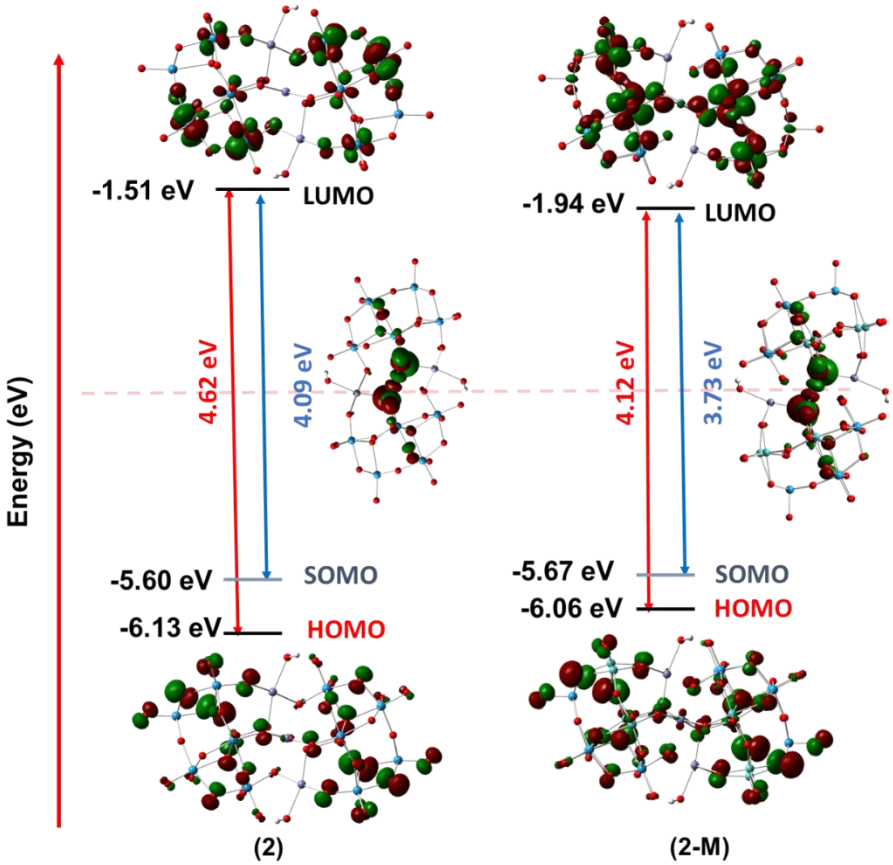

Figure S19. Frontier molecular orbitals of tetrasubstituted sandwich POMs showing the effect of Mo doping on band gaps and shifting of electron density on addenda atoms in **2** and **2-M**.

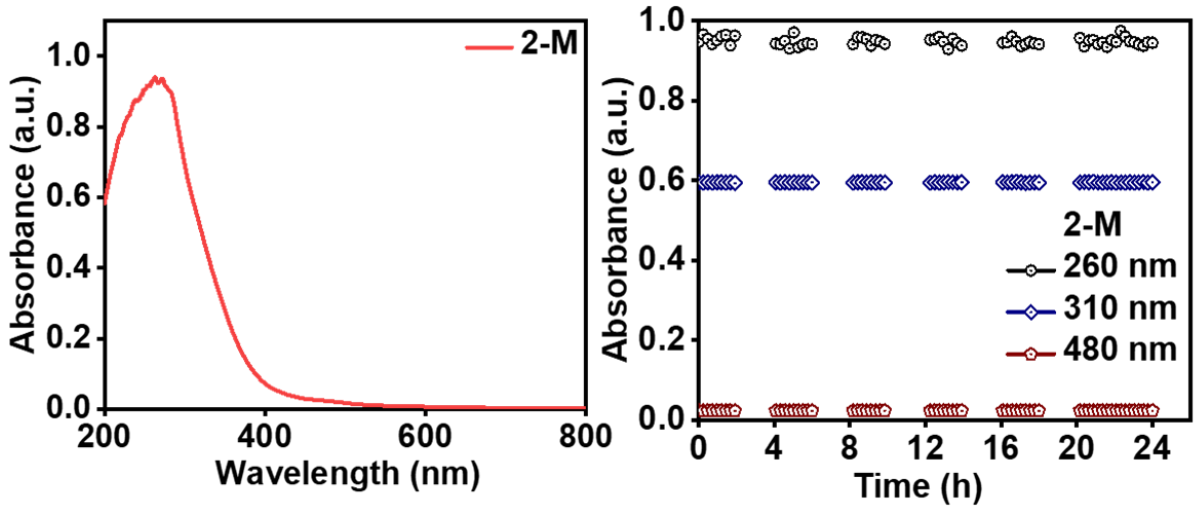

Figure S20. (left) UV-vis spectrum of 0.1 mM aqueous solution of **2-M**, and (right) changes in UV-vis spectra over a period of 24 hours at ambient atmosphere (no change was observed).

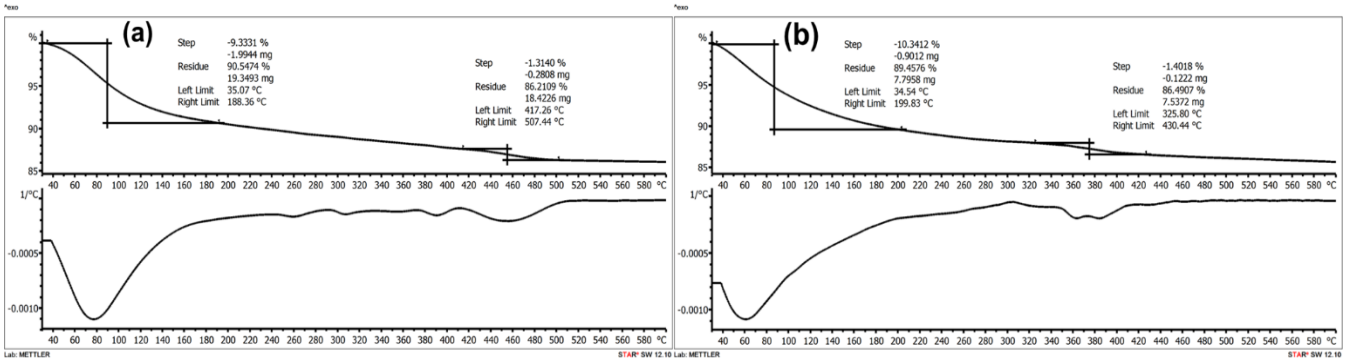

Figure S21. TGA curve along with the corresponding first derivative of (a) **2** and (b) **2-M**.

Characterization analysis of 2 and 2-M

Compounds **2** and **2-M** were characterized using SC-XRD, FT-IR, ESI-MS, and UV-visible spectroscopy (Figure S12-S21). The framework structure was confirmed by SC-XRD (**CCDC 2330240** and **2330247).** The light yellow-colored crystals (Figure S12) of **2** crystallize in triclinic with $P\bar{1}$ Space group and **2-M** crystallize in monoclinic with $P2_1/n$ space group (Table S6). BVS calculation indicates that all addenda atoms are in their highest oxidation state (+6) and Zn, Fe in +2 and +3 oxidation states, respectively (Table S7). The 3D SC-XRD structure of **2** and **2-M** shows that the tri-lacunary Keggin moiety contains a tetrahedrally bound zinc atom in the center as a templating agent to triads of addenda W/Mo atoms. The tetrasubstituted sandwich core consists of Fe at the internal $\{TM_i\}$ position and Zn as external atoms $\{TM_e\}$ (Figure S12b). From the comparison of $[\{Zn_2Fe_2(H_2O)_2(ZnFeMo_xW_{9-x})_2\}^{14-}]$, with the reference structure (Figure S1), it is clear that Mo incorporation is favorable at the entire belt position, most favorable at 4/5 which are connected to transition metals in the sandwich position through μ_2 oxygens (Figure S12c). The other positions in the cap are comparatively less favorable for Mo incorporation. The distance between Zn atoms at the external and Zn/Fe at the internal positions is 3.15 Å in **2/2-M**; however, the distance between Zn/Fe atoms in the internal positions is 3.08 Å in **2** and 3.16 Å in **2-M**. It was observed that at a particular pH, analyzing different crystals from the same mother liquor

indicates a different ratio of Mo to W (Figure S12c) as observed in **2-M(a)** (**CCDC 2330252)**, which was further confirmed from ESI-MS.

The ESI-mass spectrum of **2** in (Figure S13, Table S8) shows the envelope of peaks at m/z 1593 (z= –3), while the analog mixed addenda POMs (**2-M**) structure shows the isotopic multiple envelopes of peaks attributed to varying ratios of Mo to W. **2-M** show the envelopes of peaks (Figure S14, Table S9) in the range of *m*/*z* 1380-1560 for $[H\{Zn_2Fe_2(H_2O)_2(ZnFeMo_xW_{9-x})_2\}^{3-}]$, and *m*/*z* 2100-2400 for $[\{Zn_2Fe_2(H_2O)_2(ZnFeMo_xW_{9-x})_2\}^{2-}]$. The most abundant anion in **2-M** has the composition of Mo/W (2:7) with the formula $[\{Zn_2Fe_2(H_2O)_2(FeMo_2W_7O_{34})_2\}^{14-}]$, while the Mo/W ratio varies from 1:17 to 7:11 with a constant charge of the cluster, i.e., -14. Further, pH plays a crucial role in tuning the amount of Mo addenda incorporation. Hence, to understand the control of the Mo/W ratio in the sandwich framework of **2-M**, an ESI-MS-based systematic study was performed by varying pH. From ESI-MS, it was found that for the most abundant peak, the Mo/W ratio increases by decreasing the pH from 7.5 to 6.0; however, a further decrease in the pH results in the formation of the Keggin framework (Figure S15, Table S10). EDAX demonstrates that all elements are uniformly distributed with bulk composition as $Na_{14.9}Zn_{5.3}Fe_{1.5}Mo_{2.0}W_{11.8}O_{64.7}$ (Figure S16a). From the atom percentage, it is clear that all the elements are in accordance with the ratio of atomic composition of the crystal structure of **2-M**. This has been further confirmed using powder X-ray diffraction analysis (PXRD). The experimental PXRD patterns are consistent with their simulated pattern (Figure S16b, S16c), indicating the phase purity of **2** and **2-M**.

A subtle variation in the characteristic peaks was observed while comparing the stretching frequencies of tetrasubstituted mixed addenda sandwich POMs with corresponding tungstate-only sandwich POMs. The FT-IR/Raman spectra of **2** show the characteristic peaks in the region 650-920 cm^{-1} with characteristic peaks at 917 cm^{-1} ($W{=}O_{term}$), 835, 657 cm^{-1} (W-O-W) cm^{-1} (Figure S17b-S17c). The FT-IR spectra of **2-M** show characteristic peaks similar to **2** in the region 650-920 cm^{-1} with slight shifting due to Mo incorporation in the framework. The $M{=}O_{term}$ characteristic peak shifts to 913 cm^{-1}, while M-O-M (M=Mo/W) peak shifts are negligible (Figure S17b). From the FT-IR study of O_2-activated **2**, two peaks at 1149 and 1203 cm^{-1}, along with 833 cm^{-1} have been observed, indicating dioxygen activation using these POMs (Figure S17a). ^{57}Fe Mössbauer spectrum of **2-M** indicates two singlets with isomeric shift of -0.04 due to heteroatom position and +0.53 due to internal sandwich position, which confirms two types of Fe are present in the structure (Figure S17d). Both **2** and **2-M** exhibit broad absorption bands in the UV-vis region due to ligand to metal charge transfer (LMCT) ($O_{2p} \rightarrow W_{5d}$), and a feeble peak is observed for transition metal to POM charge transfer at 472 nm ($TM \rightarrow W_{5d}$), indicating Metal to metal charge transfer (MMCT). Moreover, a significant contribution of Mo is evident in mixed addenda sandwich POMs through a red shift in the UV-vis spectra compared to W-based sandwich POMs (Figure S18a). This red shift can be explained by the changes in the band gap of these POMs, which were investigated using DRS. These results were further supported by DFT studies, where the HOMO-LUMO band gap in **2-M** (representative structure of 2-M is taken with the formula $[Zn_2Fe_2(H_2O)_2(ZnMo_4W_5)_2\}^{14-}]$ falls lower than that of **2** (Figure S19). The LUMO energy, as well as the band gap energy (HOMO-LUMO) drops, going from **2** to **2-M**, which also correlates well with UV-visible spectroscopy. The band positions and overall charge on the POM play crucial roles in defining their redox characteristics, e.g., **2-M** is easy to reduce and a powerful

oxidizing agent compared to **2**. While the overall charge is constant in all these sandwich POMs, the relatively lower LUMO energy in mixed addenda POMs correlates well with the higher electron affinity compared to their corresponding W-analogues. To identify the most suitable position for Mo substitution, one Mo-substituted at each addenda position in the mixed addenda sandwich POM was investigated using DFT studies in our previous report,[3] where it was observed that the μ_2-oxygen dissipates the lowest energy in Mo incorporation in the framework of these POMs. The solution state UV-visible study of **2-M** for 24 hours shows no change in absorbance, thus reflecting its stability in aqueous solution (Figure S20). Thermal stability was determined by TGA analysis from 30 to 600 °C (Figure S21). The TGA curve of **2/2-M** shows negligible weight loss, thus indicating high thermal stability up to 600 °C. The first weight loss observed in the range of 30-190 °C can be attributed to the release of water of crystallization. The small weight loss in the 300-450 °C range can be the release of water molecules coordinated to the counter cations outside the POM framework.[4, 5]

Characterizations of 3 and 3-M.

Table S11. Crystal data, data collection, and refinement parameters for 3 and 3-M		
	3	**3-M**
CCDC number	**2330239**	**2330253**
empirical formula	$Co_4Fe_2H_{12}Na_{17}O_{105}W_{18}$	$Co_4Fe_2Mo_{2.84}Na_{13}O_{109}W_{15.16}$
formula weight	5739.19	5450.25
temp (K)	273.15	273.15
crystal system	Monoclinic	Monoclinic
space group	$P2_1/n$	$P2_1/n$
unit cell dimension		
a (Å)	13.064(3)	13.0895(6)
b (Å)	17.740(4)	17.7586(8)
c (Å)	21.015(6)	21.1435(11)
α (deg)	90	90
β (deg)	93.599(9)	93.488(2)
γ (deg)	90	90
V (Å^3)	4861(2)	4905.7(4)
Z	2	2
ρ (calculated) (g/cm^3)	3.921	3.690
μ/mm^{-1}	22.351	19.168
F (000)	5062.0	4833.0
crystal size (mm^3)	0.41 × 0.41 × 0.23	0.34 × 0.32 × 0.32
2Θ range data /°	4.25 to 53.12	4.41 to 52.84
index ranges	$-16 \le h \le 15$, $-19 \le k \le 21$, $-26 \le l \le 18$	$-15 \le h \le 16$, $-22 \le k \le 22$, $-23 \le l \le 26$
no. of reflection collected /unique	24711/9975	41028/10022
GOF on F^2	1.026	1.079
R(int)	0.051	0.042
final *R* indices ($I > 2\sigma(I)$)	$R_1 = 0.0386$, $wR_2 = 0.0917$	$R_1 = 0.0270$, $wR_2 = 0.0648$
R indices (all data)	$R_1 = 0.0495$, $wR_2 = 0.0977$	$R_1 = 0.0297$, $wR_2 = 0.0660$
data/restraints/param	9975/0/680	10022/0/704
Largest diff. peak/hole / e Å^{-3}	2.14/-1.47	2.27/-1.41

Table S12. Bond valence parameter of selected atoms calculated from the SC-XRD structure of **3** and **3-M**			
POMs	**Transition metal**	**Bond valence sum value**	**Oxidation state**
3	W	6.13	+6
	Fe	3.07	+3
	Co1	2.36	+2
	Co2	2.06	+2
3-M	Mo	6.11	+6
	W	6.06	+6
	Fe	3.21	+3
	Co1	2.54	+2
	Co2	2.01	+2

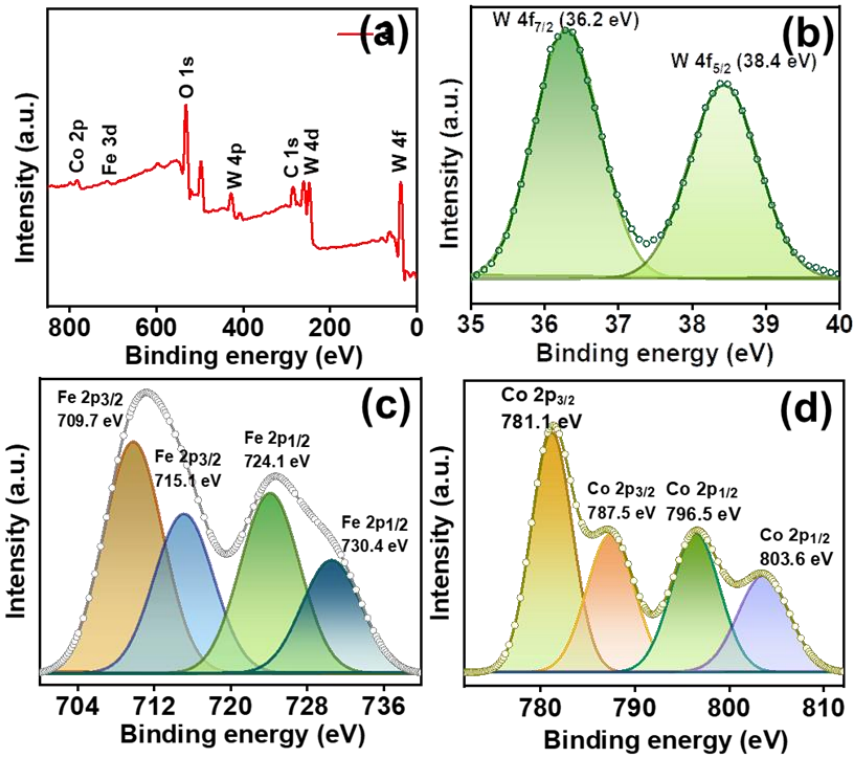

Figure S22. XP spectra of **3** showing (a) Survey spectra, (b) W $4f_{7/2}$ and $4f_{5/2}$ (b) W $4f_{7/2}$ and $4f_{5/2}$ (c) Fe $2p_{3/2}$ and $2p_{1/2}$, and (d) Co $2p_{3/2}$ and $2p_{1/2}$.

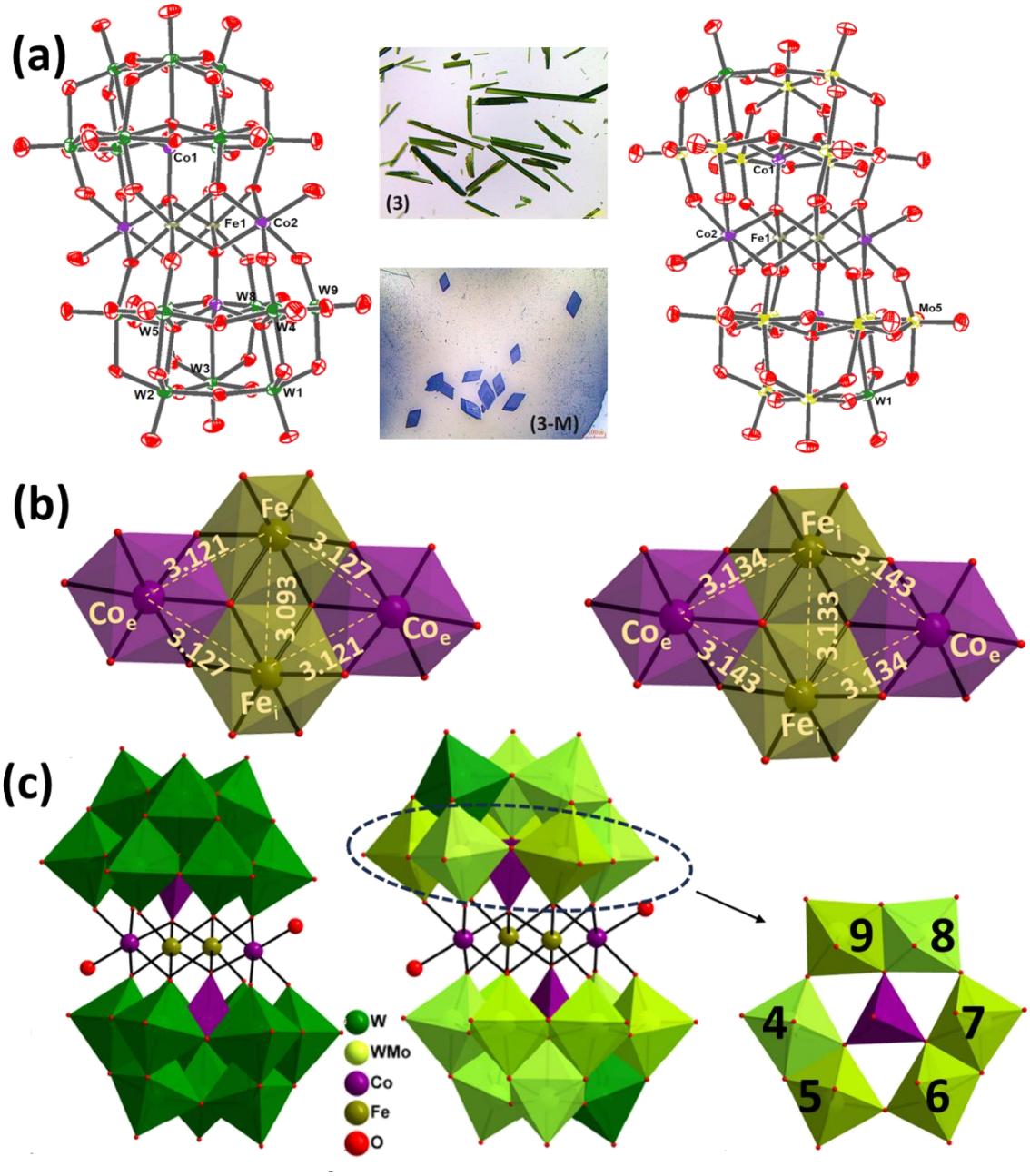

Figure S23. (a) ORTEP drawing (with 60% ellipsoid probability) and Optical images of sandwich POMs **3** (left) and **3-M** (right); (b) Cubane core showing the interatomic distance between TMs in **3** (left) and **3-M** (right); (c) combined polyhedral/ball and stick representation of **3** (left) and **3-M** (right), belt 2 depicting different ratios of molybdenum to tungsten in **3-M**; (Countercations and hydrogen atoms are omitted for clarity).

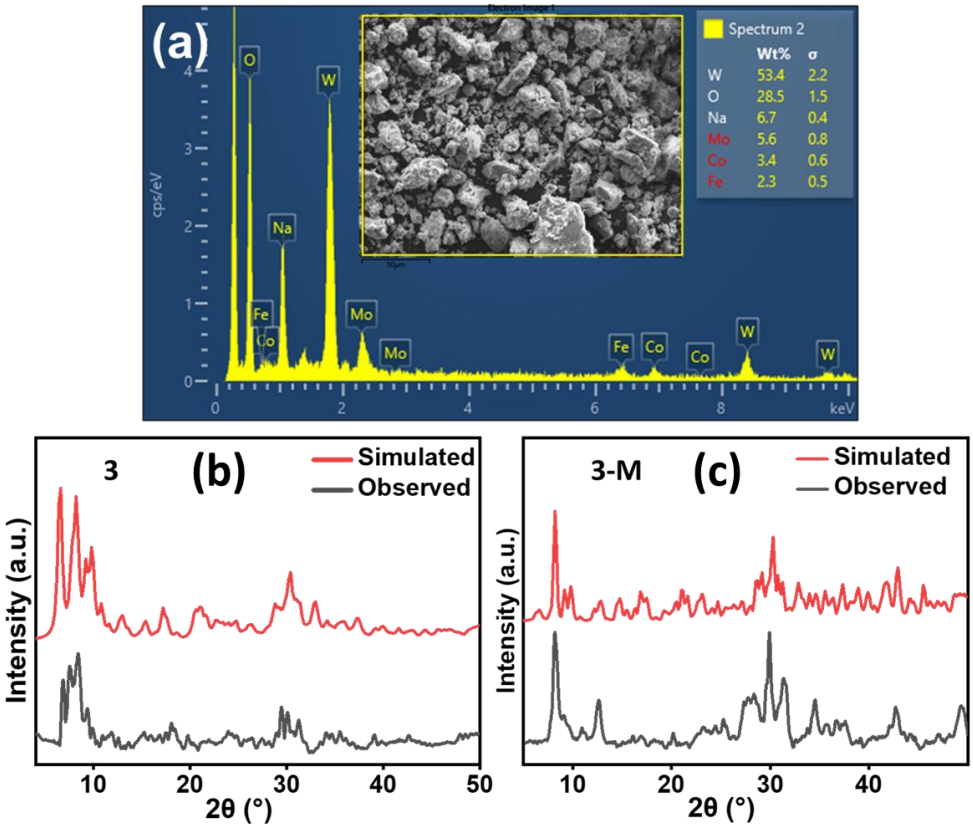

Figure S24. (a) EDX mapping for **3-M**; Observed PXRD pattern and comparison with the simulated data obtained from single crystal XRD for (b) **3** (c) **3-M.**

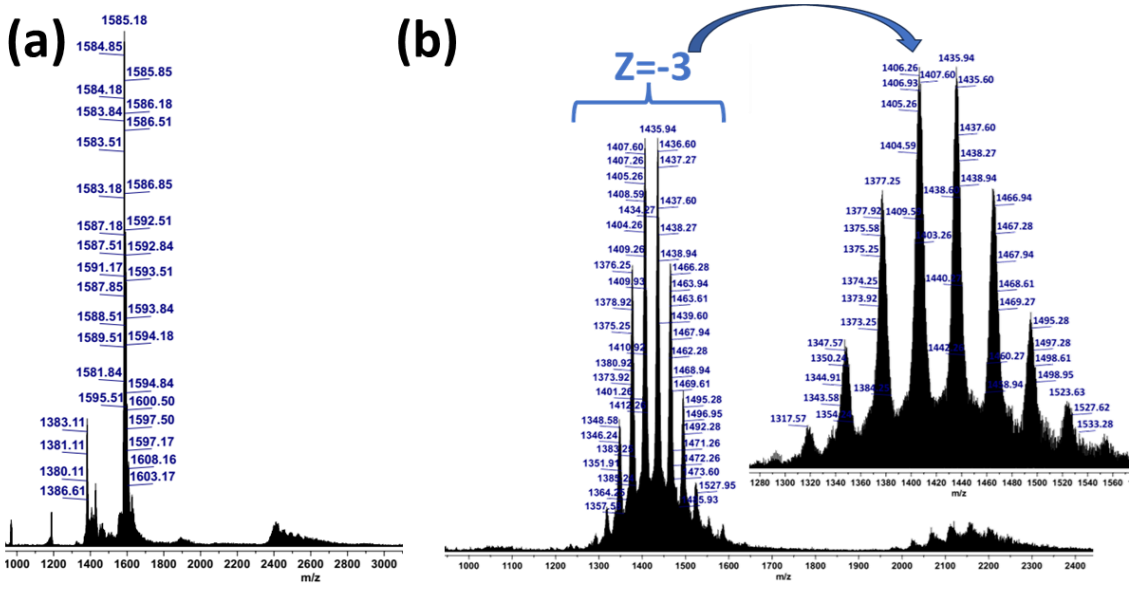

Figure S25. ESI-MS spectra of (a) **3** and (b) **3-M** in the range of m/z 1000-2500 for different z values.

Table S13. Assignment of ESI-mass peaks of **3/3-M**				
Charge	**m/z (obs.)**	**m/z (calc.)**	**Mol. Wt.**	**Assigned probable formula**
-3	1585.18	1585.13	4755.39	$H_{11}Co_2Fe_2(Co_2W_{18}O_{68})$
-3	1495.28	1495.75	4487.27	$H_{10}Co_2Fe_2(FeCoMo_3W_{15}O_{68})$
-3	1466.94	1466.74	4400.23	$H_{10}Co_2Fe_2(FeCoMo_4W_{14}O_{68})$
-3	1435.94	1436.06	4308.19	$H_9Co_2Fe_2(Fe_2Mo_5W_{13}O_{68})$
-3	1406.26	1406.71	4220.15	$H_9Co_2Fe_2(Fe_2Mo_6W_{12}O_{68})$
-3	1377.25	1377.37	4132.11	$H_9Co_2Fe_2(Fe_2Mo_7W_{11}O_{68})$
-3	1347.57	1347.68	4043.06	$H_9Co_2Fe_2(Fe_2Mo_7W_{11}O_{68})$

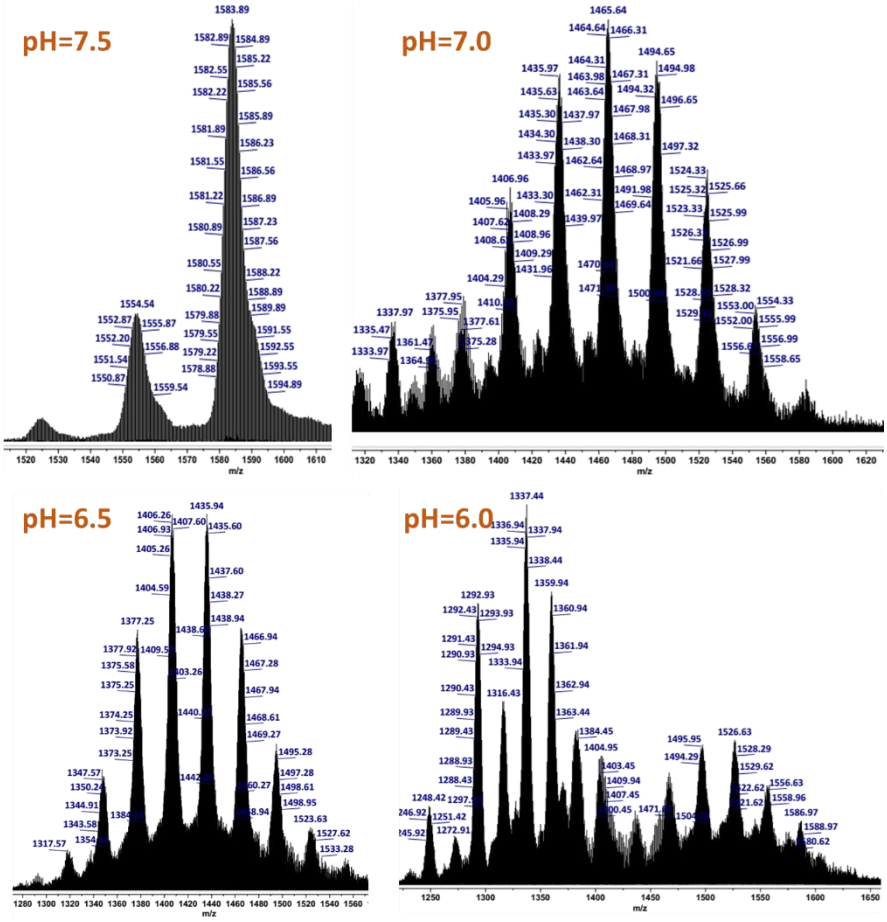

Figure S26. pH-dependent ESI-MS spectra of **3-M** with charge (z) = –3

Table S14. Assignment of ESI-mass peaks of 3-M (pH dependent study)				
Charge	**m/z (obs.)**	**m/z (calc.)**	**Mol. Wt.**	**Assigned probable formula**
-3	1583.89	1583.79	4751.39	$H_{10}Co_2Fe_2(FeCoW_{18}O_{68})$
-3	1554.54	1554.45	4663.35	$H_{10}Co_2Fe_2(FeCoMoW_{17}O_{68})$
-3	1524.33	1525.10	4575.31	$H_{10}Co_2Fe_2(FeCoMo_2W_{16}O_{68})$
-3	1494.98	1495.75	4487.27	$H_{10}Co_2Fe_2(FeCoMo_3W_{15}O_{68})$
-3	1465.64	1466.74	4400.23	$H_{10}Co_2Fe_2(FeCoMo_4W_{14}O_{68})$

-3	1435.97	1436.06	4308.19	$H_9Co_2Fe_2(Fe_2Mo_5W_{13}O_{68})$
-3	1406.96	1406.71	4220.15	$H_9Co_2Fe_2(Fe_2Mo_6W_{12}O_{68})$
-3	1377.25	1377.37	4132.11	$H_9Co_2Fe_2(Fe_2Mo_7W_{11}O_{68})$
-3	1347.57	1348.02	4044.07	$H_9Co_2Fe_2(Fe_2Mo_8W_{10}O_{68})$
-3	1317.57	1318.67	3956.03	$H_9Co_2Fe_2(Fe_2Mo_9W_9O_{68})$

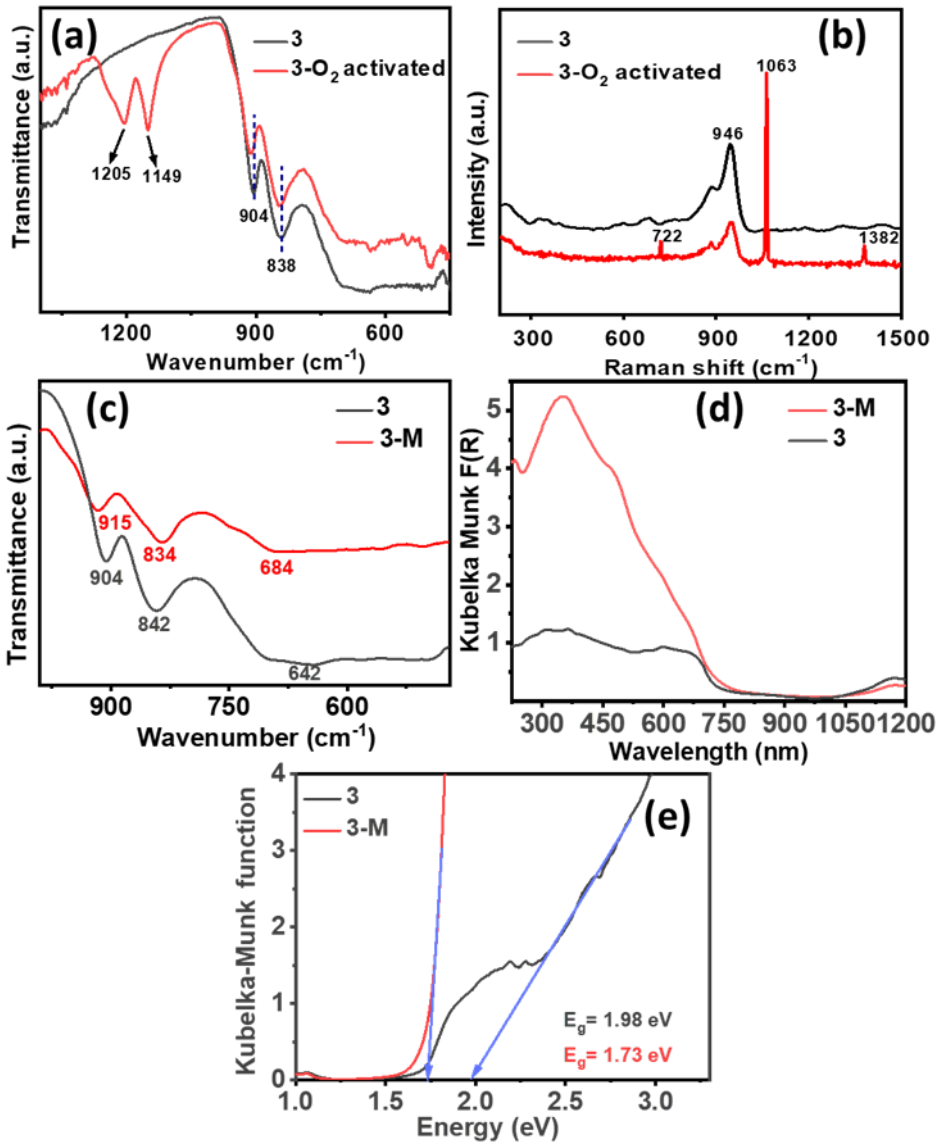

Figure S27. (a) FT-IR and (b) Raman spectra of **3** before and after O_2 treatment; (c) FT-IR and (d) solid-state UV-vis spectra of **3** and **3-M** (e) corresponding optical band-gap derived from the Kubelka-Munk equation in **3** and **3-M**.

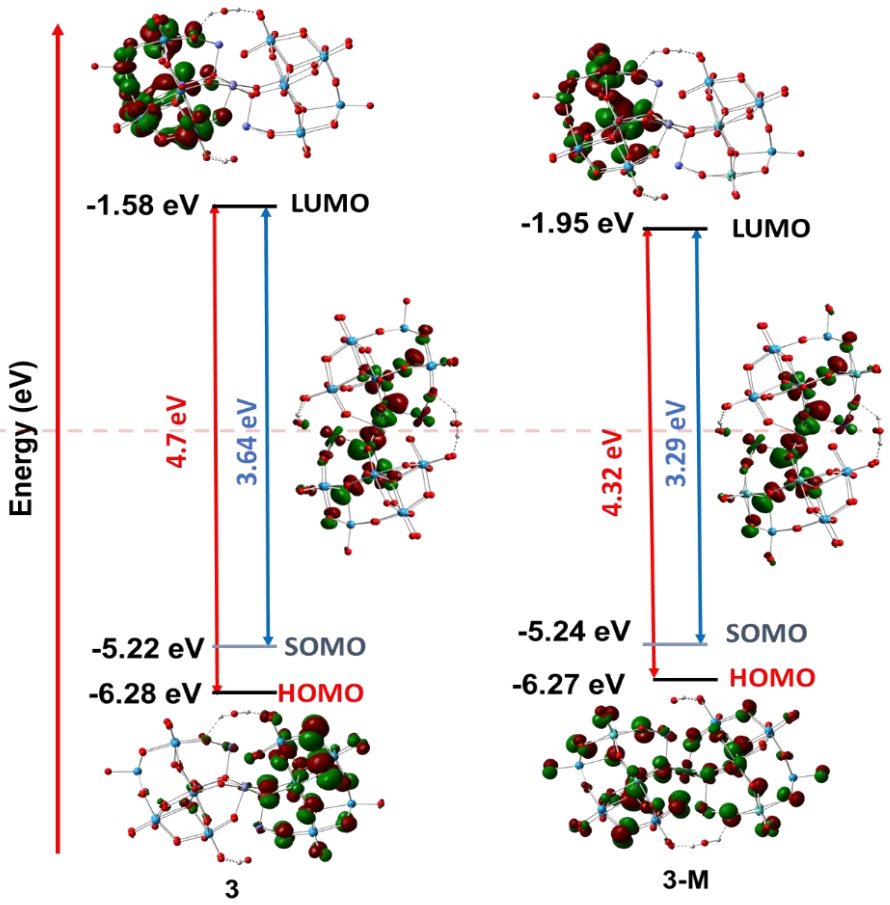

Figure S28. Frontier molecular orbitals of tetrasubstituted sandwich POMs showing the effect of Mo doping on band gaps as well as shifting of electron density on addenda atoms in **3** and **3-M**.

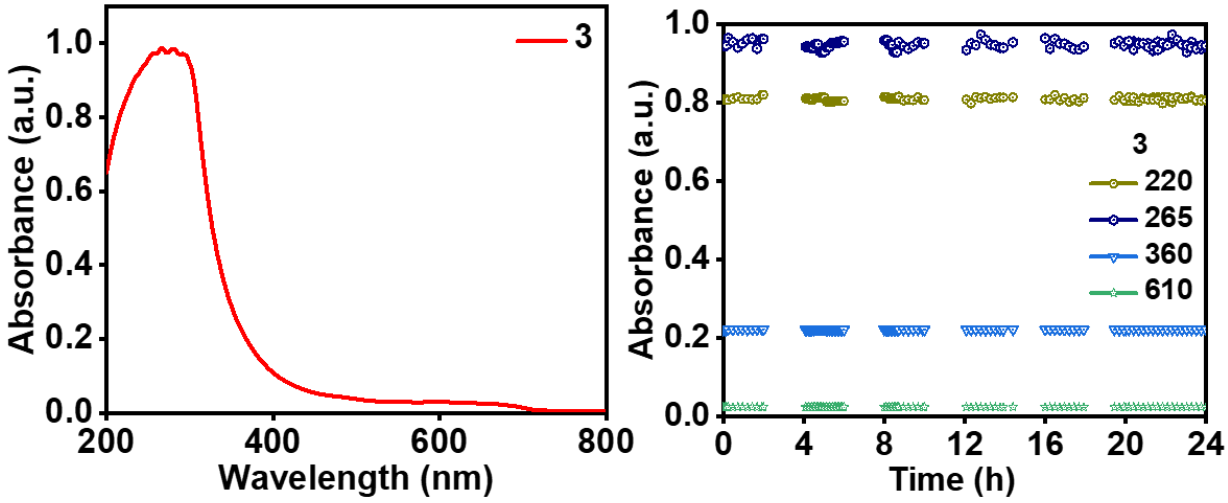

Figure S29. UV-visible spectra of **3** in aqueous solution (left) and changes in UV-visible spectra of 0.1 mM **3** over 24 hours (right, no change was observed).

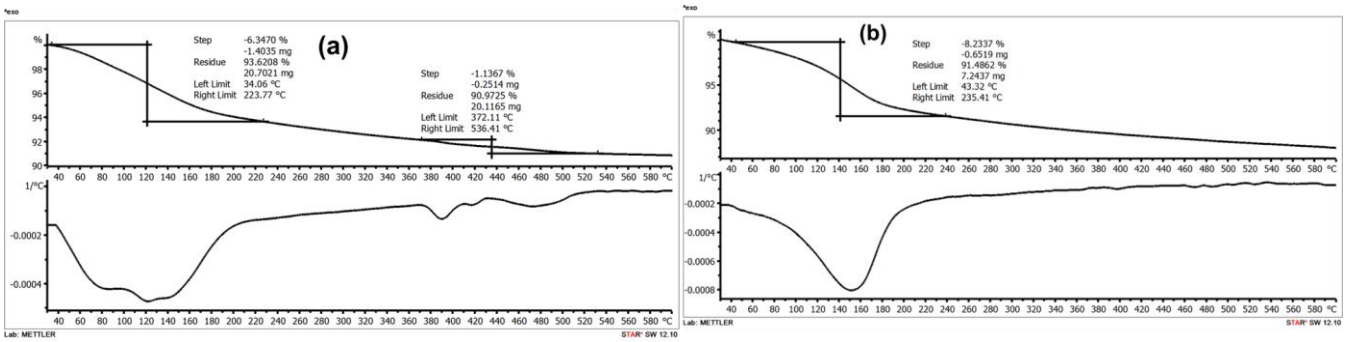

Figure S30. TGA curve along with corresponding first derivative of (a) **3** (b) **3-M.**

Characterization analysis of 3 and 3-M

Compounds **3** and **3-M** were characterized using SC-XRD, FT-IR, ESI-MS, XPS, and UV-visible spectroscopy (Figure S22-S30). The framework structure was confirmed by SC-XRD (**CCDC 2330239, 2330253)** (Table S11). The needle-shaped green-coloured crystals (Figure S23a) of **3** and dark purple-colored crystals of **3-M** crystallize in monoclinic with $P2_1/n$ space group. The 3D SC-XRD structure of **3** and **3-M** shows that the trilacunary Keggin moiety contains a tetrahedrally bound cobalt/iron atom in the center as a templating agent to triads of addenda W/Mo atoms (Figure S23). The tetrasubstituted sandwich core consists of Fe at the internal $\{TM_i\}$ position and Co as external atoms $\{TM_e\}$. From the comparison of **3-M** with the reference structure (Figure S23b), it is clear that Mo incorporation is favorable at all the belt positions. Except for position 1, other positions in the cap are comparatively more favorable for Mo incorporation than **2-M** (Figure S23c). The distance between Co atoms at the external and Fe at the internal positions is 3.12-3.15 Å in **3/3-M**. However, the distance between Zn/Fe atoms in the internal positions is 3.09 Å in **3** and 3.13 Å in **3-M** (Figure S23b). BVS calculation indicates that all addenda atoms are in their highest oxidation state (+6) and Co, Fe in +2 and +3 oxidation states, respectively (Table S12). Apart from the BVS, the oxidation states of all of the atoms in **3** were determined from XPS analysis. The XP spectra of **3** revealed the presence of tungsten (W), iron (Fe), cobalt (Co), and oxygen. The two peaks at 713.2 and 723.5 eV in **3** can be attributed to the presence of Fe in a +3 oxidation state. The W 4f doublet appears between 36.2 and 38.4 eV, corresponding to W $4f_{7/2}$ and $4f_{5/2}$ in **3-M**, respectively (Figure S22). EDAX demonstrates that all elements are uniformly distributed with bulk composition as $Na_{11.6}Co_{2.3}Fe_{1.6}W_{11.5}Mo_{2.3}O_{70.7}$ (Figure S24a). From the atom percentage, it is clear that all the elements are in accordance with the ratio of atomic composition of the crystal structure of **3-M**. This has been further confirmed using powder X-ray diffraction analysis (PXRD). The experimental PXRD patterns are consistent with their simulated pattern (Figure S24b, S24c), indicating the phase purity of **3** and **3-M**.

ESI-mass spectrum of **3** in (Figure S25a, Table S13) shows the envelope of peaks at m/z 1585 (z=-3) while the analog mixed addenda POMs structure shows the isotopic multiple envelopes of peaks attributed to varying ratios of Mo to W. The mixed addenda sandwich POMs **3-M** show the envelopes of peaks (Figure S25b, Table S13) in the range of *m/z* 1300-1530 for $[\{Co_2Fe_2(H_2O)_2(CoMo_xW_{9-x})_2\}^{3-}]$, and *m/z* 2050-2300 for $[\{Co_2Fe_2(H_2O)_2(CoMo_xW_{9-x})_2\}^{2-}]$. The most abundant anion in **3-M** has the composition of Mo/W (5:13) with the formula $[\{Co_2Fe_2(H_2O)_2(CoMo_{2.5}W_{6.5}O_{34})_2\}^{14-}]$, while the Mo/W ratio varies from 1:5 to 7:11 with a constant charge of the cluster, i.e., -14. Further, pH plays a crucial role in tuning the amount of Mo addenda incorporation.

Hence, to understand the controlling of the Mo/W ratio in the sandwich framework of **3-M**, an ESI-MS-based systematic study was performed by varying pH (Figure S26, Table S14). From ESI-MS, it was found that for the most abundant peak, the Mo/W ratio increases by decreasing the pH from 7.5 to 6.5; however, a further decrease in the pH results in the formation of the Keggin framework along with the sandwich POM.

From the FT-IR study of O_2-activated **3**, two peaks at 1149 and 1205 cm^{-1} have been observed, indicating the formation of O_2 activation using these POMs (Figure S27a). This was further supported in Raman spectra where peaks at 722, 1063 cm^{-1} have been observed in the O_2 activated **3** (Figure S27b). A subtle variation in the characteristic peaks was observed while comparing the stretching frequencies of **3-M** with **3**. The FT-IR spectra of **3** show the characteristics peaks in the region 650-920 cm^{-1} with characteristics peaks at 904 cm^{-1} ($W{=}O_{term}$), 842, 642 cm^{-1} (W-O-W) cm^{-1} (Figure S27c). The FT-IR spectra of **3-M** show characteristic peaks similar to **3** in the region 650-920 cm^{-1} with slight shifting due to Mo incorporation in the framework. The $M{=}O_{term}$ characteristics peaks shift to 915 cm^{-1} while M-O-M (M=Mo/W) peak shifts to 834, 684 in **3-M** (Figure S27c) after Mo incorporation in the framework structure.

Both **3** and **3-M** exhibit broad absorption bands in the UV-vis region due to ligand-to-metal charge transfer (LMCT) ($O_{2p} \rightarrow W_{5d}$), as well as d-d transitions, and a feeble peak is observed for transition metal to POM charge transfer (MMCT) at 478 nm ($TM \rightarrow W_{5d}$). Moreover, a significant contribution of Mo is evident in mixed addenda sandwich POMs through a red shift in the UV-vis spectra compared to that W-based sandwich POMs (Figure S27d). This red shift can be explained by the changes in the band gap of these POMs, which were investigated using DRS. These results were further supported by DFT studies where the HOMO-LUMO band gap in **3-M** (representative structure of **3-M** is taken with formula $\{Co_2Fe_2(H_2O)_2(CoMo_4W_5)_2\}^{10-}$) falls lower than that of **3** (Figure S28). The LUMO energy, as well as the band gap energy (HOMO-LUMO) drops going from **3** to **3-M** (Figure S27e), which also correlates well with UV-visible spectroscopy. The band positions and overall charge on the POM play crucial roles in defining their redox characteristics. While the overall charge is constant in all these sandwich POMs, the relatively lower LUMO energy in mixed addenda POMs correlates well with the higher electron affinity compared to their corresponding W-analogues. The solution state UV-visible study of **3** for 24 hours shows no change in absorbance, thus reflecting its stability in aqueous solution for longer periods (Figure S29). Thermal stability of **3**/**3-M** was determined by TGA analysis from 30 to 600 °C (Figure S30). The TGA curve of **3/3-M** shows high thermal stability even up to 600 °C. The first weight loss observed in the range of 30-220 °C can be attributed to the release of water of crystallization. In **3**, small weight loss in the 350-420 °C range can be attributed to the release of water molecules coordinated to the counter cations outside the POM framework.

Characterizations of 4 and 4-M.

Table S15. Crystal data, data collection, and refinement parameters for 4 and 4-M		
	4	**4-M**
CCDC number	**2330243**	**2330242**
empirical formula	$Mn_4Na_{24}O_{216}W_{36.6}Zn_{7.4}$	$Mn_2Mo_{0.24}Na_{15}O_{104}W_{18.16}Zn_{3.6}$
formula weight	11440.17	5715.80
temp (K)	273.15	273.15
crystal system	monoclinic	Monoclinic
space group	$P2_1/n$	$P2_1/n$
unit cell dimension		
a (Å)	13.094(5)	13.152(2)
b (Å)	17.717(7)	17.774(3)
c (Å)	21.014(8)	21.019(3)
α (deg)	90	90
β (deg)	93.582(12)	93.447(6)
γ (deg)	90	90
V (Å^3)	4865(3)	4904.4(14)
Z	1	2
ρ (calculated) (g/cm^3)	3.905	3.871
μ/mm^{-1}	22.856	22.525
F (000)	5022.0	5018.0
crystal size (mm^3)	0.34 × 0.27 × 0.22	0.32 × 0.31 × 0.25
2Θ range for data collection/°	3.872 to 53.02	4.234 to 52.904
index ranges	-16 ≤ h ≤ 14, -22 ≤ k ≤ 22, -26 ≤ l ≤ 26	-16 ≤ h ≤ 16, -22 ≤ k ≤ 22, -26 ≤ l ≤ 26
no. of reflection collected /unique	39686/ 10042	34878/ 10078
GOF on F^2	1.038	1.062
R(int)	0.056	0.049
final R indices ($I > 2\sigma(I)$)	R_1 = 0.0365, wR_2 = 0.0782	R_1 = 0.0332, wR_2 = 0.0829
R indices (all data)	R_1 = 0.0524, wR_2 = 0.0863	R_1 = 0.0390, wR_2 = 0.0862
data/restraints/param	10042/0/658	10078/0/659
Largest diff. peak/hole / e Å^{-3}	2.37/-1.88	2.16/-1.55

Table S16. BVS parameter of selected atoms calculated from the SC-XRD structure of **4** and **4-M**.			
POMs	Transition metal	Bond valence sum value	Oxidation state
4	W	6.13	+6
	Mn	3.07	+3
	Zn1	2.25	+2
	Zn2	2.11	+2
4-M	W	6.08	+6
	Mo	6.04	+6
	Zn1	2.31	+2
	Zn2	2.26	+2
	Mn	3.10	+3

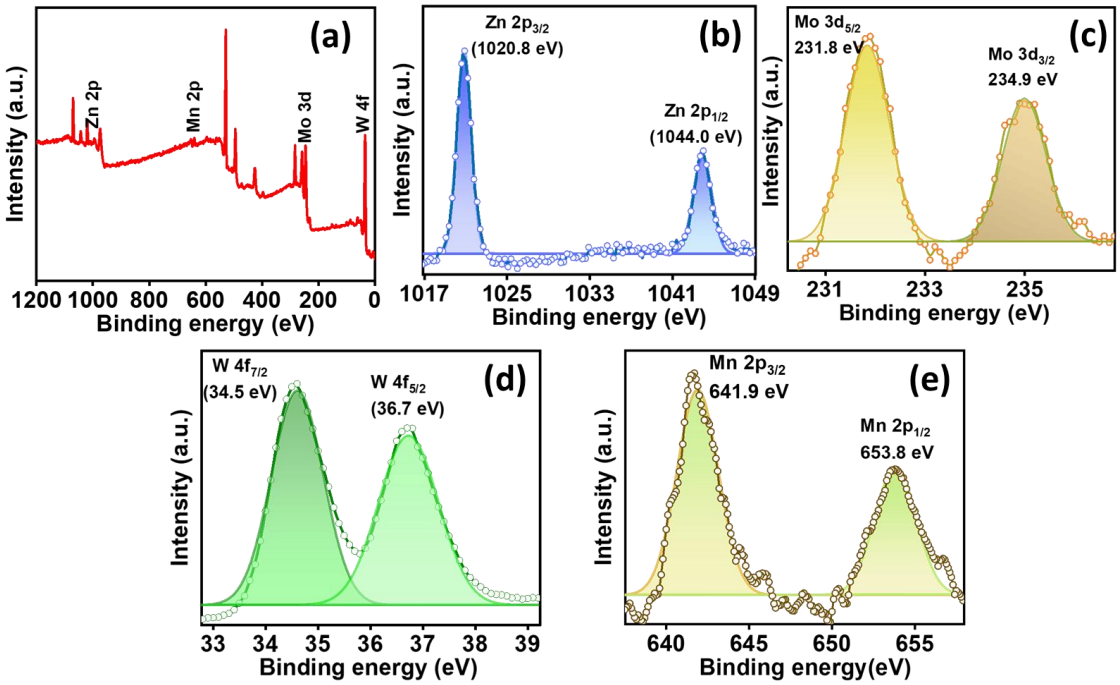

Figure S31. XP spectra of **4-M** (a) Survey spectra, (b) Zn $2p_{3/2}$ and $2p_{1/2}$, (c) Mo $3d_{5/2}$ and $3d_{3/2}$, and (d) W $4f_{7/2}$ and $4f_{5/2}$, (e) Mn $2p_{3/2}$ and $2p_{1/2}$.

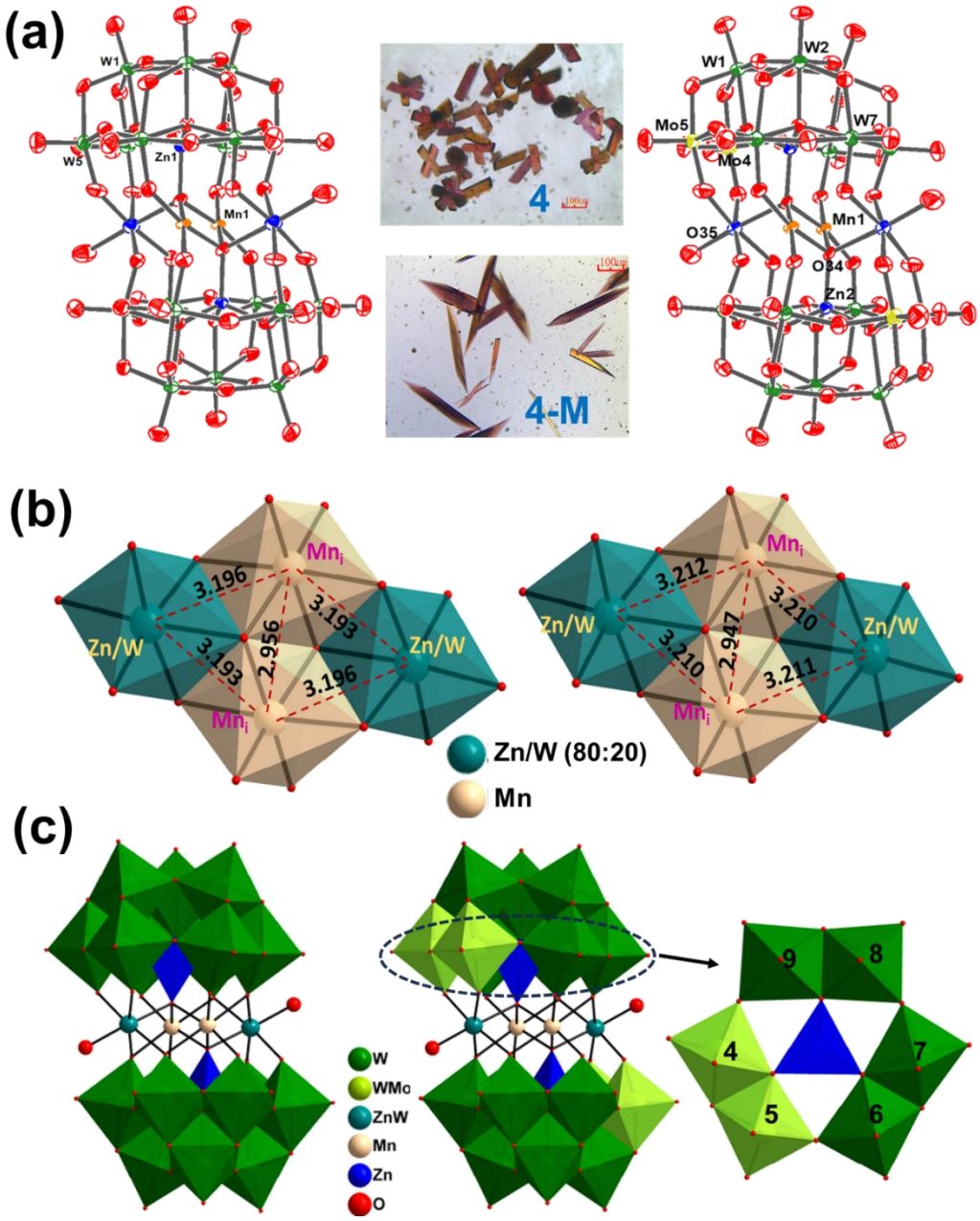

Figure S32. (a) ORTEP drawing (with 60% ellipsoid probability) and Optical images of sandwich POMs; **4** (left) and **4-M** (right); (b) Cubane core showing the interatomic distance between transition metals in **4** (left) and **4-M** (right); (c) combined polyhedral/ball and stick representation of the single-crystal X-ray structure of polyoxometalate **4** (left) and **4-M** (right), belt 2 depicting different ratios of molybdenum to tungsten in **4-M**; Countercations and hydrogen atoms are omitted for clarity.

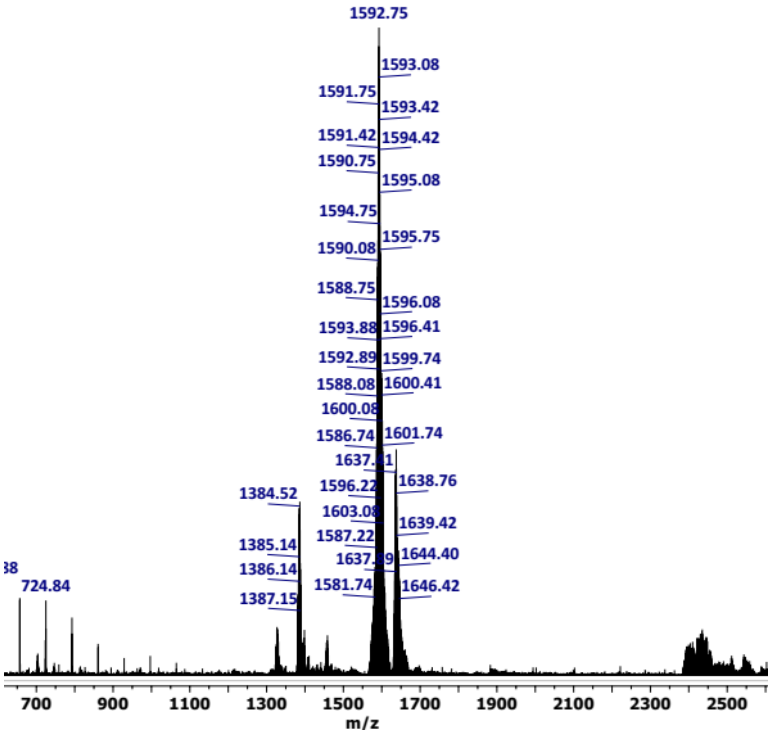

Figure S33. ESI-MS spectra of **4** in the range of m/z 700-2500 (z = –3).

Table S17. Assignment of ESI-mass peaks of **4**

Charge	m/z (obs.)	m/z (calc.)	Mol. Wt.	Assigned probable formula
-3	1592.75	1593.12	4779.37	$H_{11}Zn_2Mn_2(Zn_2W_{18}O_{68})$
-3	1637.07	1636.79	4910.39	$H_{11}Zn_2MnW(Zn_2W_{18}O_{68})$

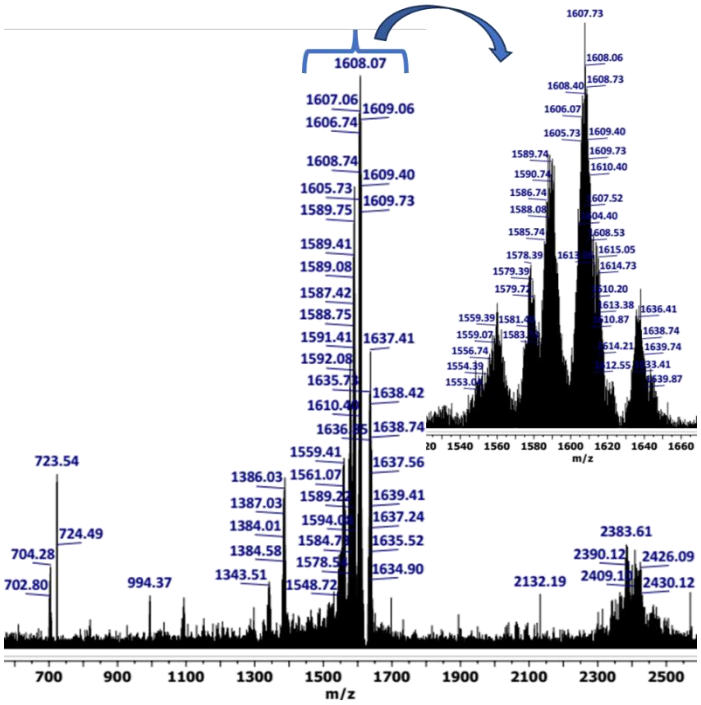

Figure S34. ESI-MS spectra of **4-M** in the range of m/z 870-2500 for different z values.

Table S18. Assignment of ESI-mass peaks of 4-M				
Charge	**m/z (obs.)**	**m/z (calc.)**	**Mol. Wt.**	**Assigned probable formula**
-3	1635.73	1635.45	4906.36	$H_{11}MnWZn_2(Zn_2W_{18}O_{68})$
-3	1607.73	1607.77	4823.33	$Na_2H_9Zn_2Mn_2(Zn_2W_{18}O_{68})$
-3	1589.74	1589.46	4768.38	$H_{11}ZnMn_3(Zn_2W_{18}O_{68})$
-3	1578.39	1578.43	4735.29	$Na_2H_9Zn_2Mn_2(Zn_2MoW_{17}O_{68})$

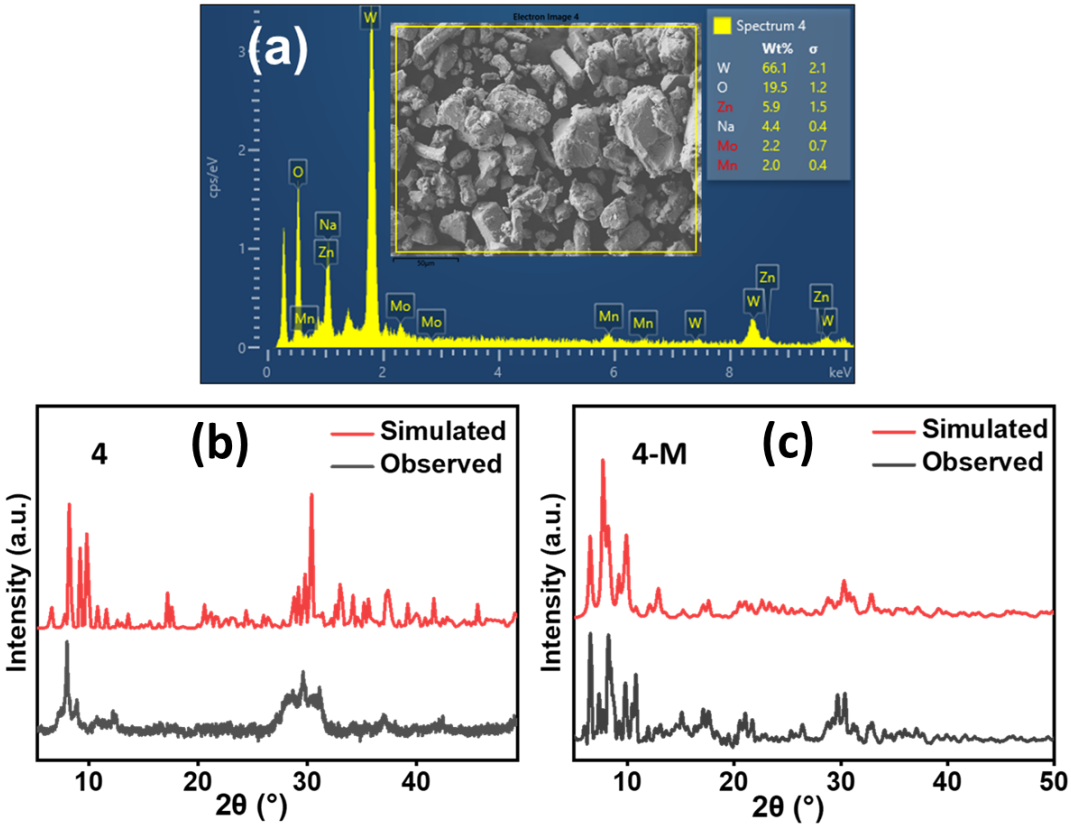

Figure S35. (a) EDX mapping for **4-M**; Observed PXRD pattern and comparison with the simulated data obtained from single crystal XRD for (b) **4** (c) **4-M.**

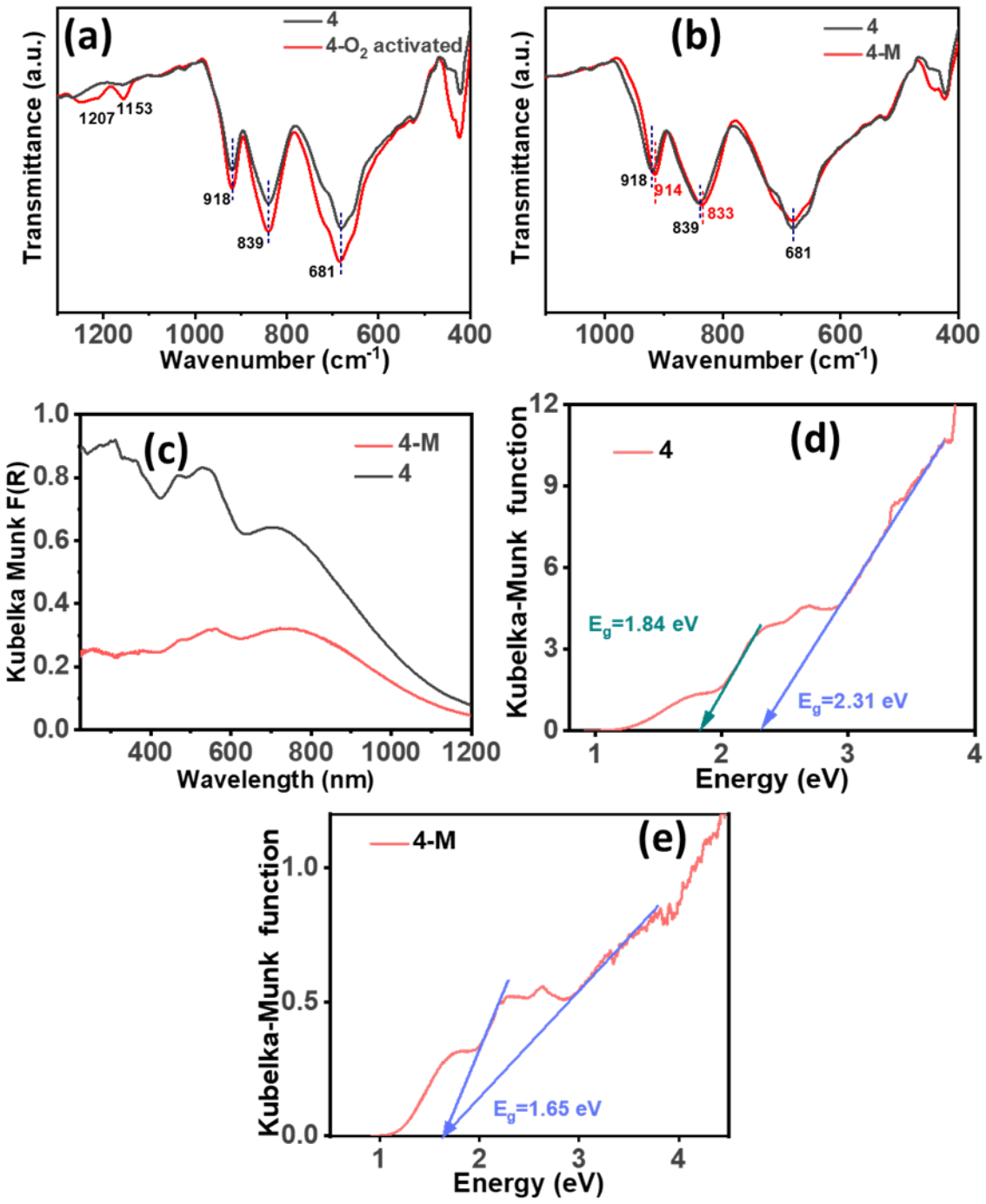

Figure S36. (a) FT-IR spectra of **4** before and after O_2 treatment; (b) FT-IR and (c) solid-state UV-vis spectra of **4** and **4-M** and corresponding optical band-gap derived from the Kubelka-Munk equation in (d) **4** and (e) **4-M**.

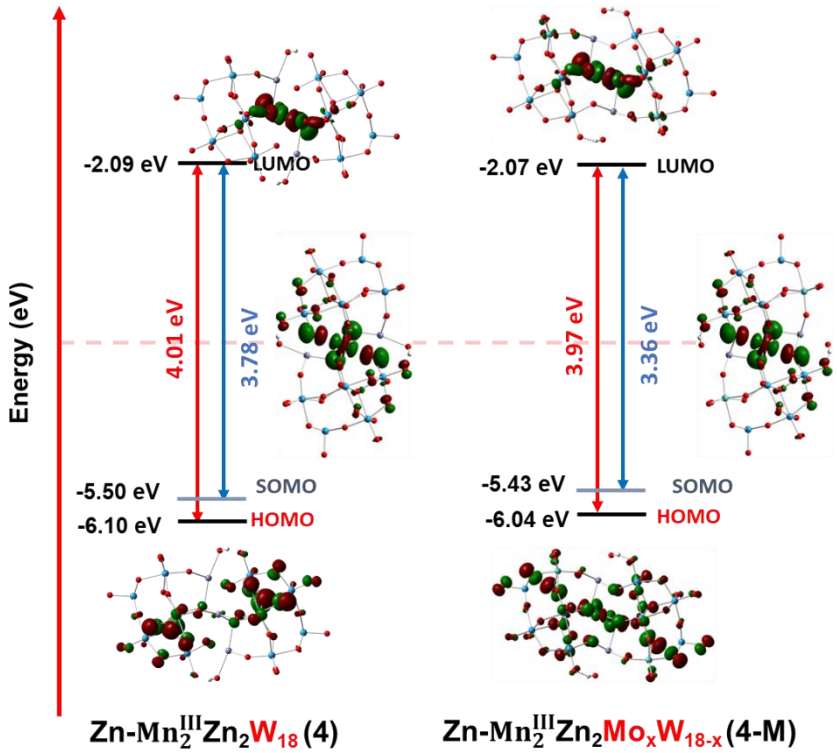

Figure S37. Frontier molecular orbitals of tetrasubstituted sandwich POMs showing the effect of Mo doping on band gaps as well as shifting of electron density on addenda atoms **4** and **4-M**.

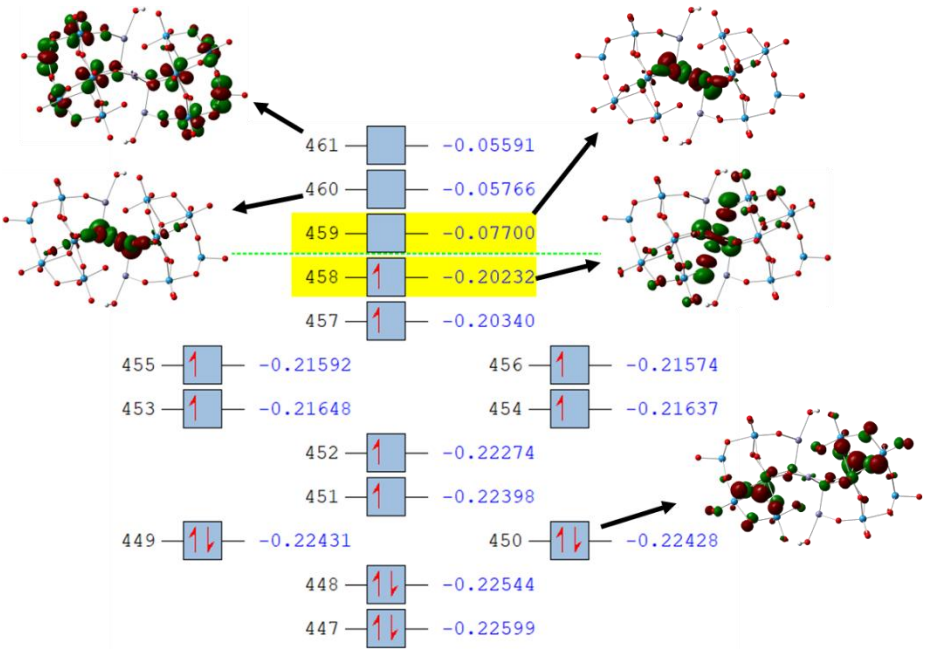

Figure S38. Frontier molecular orbitals of in **4** with characteristics molecular orbitals (highest SOMO, LUMO highlighted as yellow).

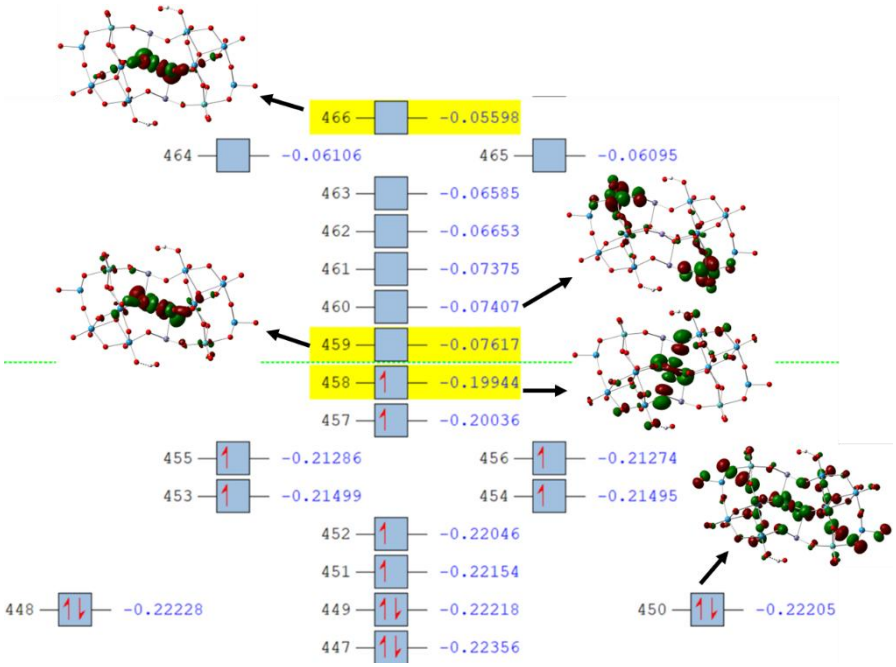

Figure S39. Frontier molecular orbitals of **4-M** with characteristics molecular orbitals (highest SOMO, LUMO highlighted as yellow).

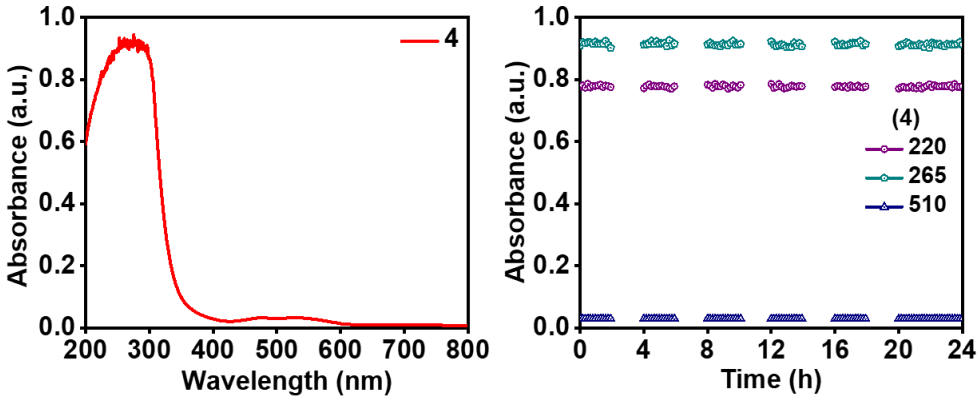

Figure S40. UV-visible spectra of **4** in aqueous solution (left) and changes in UV-visible spectra of 0.1 mM **4** over a period of 24 hour (right, no change was observed).

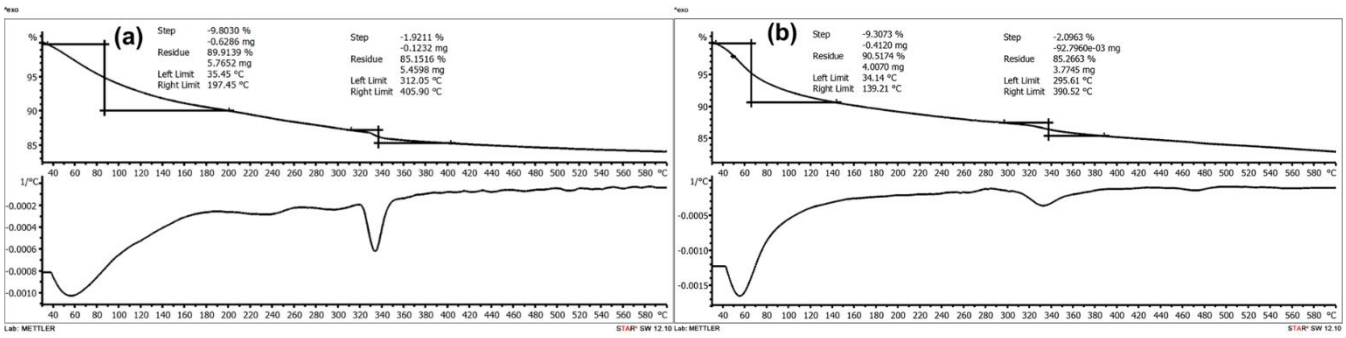

Figure S41. TGA curve along with corresponding first derivative of (a) **4** (b) **4-M**.

Characterization analysis of **4** and **4-M**

Compounds **4** and **4-M** were characterized using SC-XRD, FT-IR, ESI-MS, XPS, and UV-visible spectroscopy (Figure S31-S41). The framework structure was confirmed by SC-XRD (**CCDC 2330242, 2330243).** The dark pink-colored crystals (Figure S32a) of **4** and **4-M** crystallize in monoclinic with $P2_1/n$ space group (Table S15). The 3D SC-XRD structure of **4** and **4-M** shows that the trilacunary Keggin moiety contains a tetrahedrally bound zinc atom in the center as a templating agent to triads of addenda W/Mo atoms (Figure S32a). The tetrasubstituted sandwich core consists of Mn at the internal $\{TM_i\}$ position and Zn/W (80:20) as external atoms $\{TM_e\}$. From the comparison of **4-M** with the reference structure (Figure S1), it is clear that Mo incorporation is favorable at only 4/5 positions of the belt, which are connected to transition metals in the sandwich position through μ_2 oxygens. (Figure S32c). The other positions in the belt, as well as the cap, are not favorable for Mo incorporation. The distance between Zn atoms at the external and Mn at the internal positions is 3.19-3.21 Å in **4**/**4-M**, however, the distance between Zn/Fe atoms in the internal positions is 2.95 Å in **4**/**4-M** (Figure S32b). BVS calculation indicates that all addenda atoms are in their highest oxidation state (+6) and Zn and Mn in +2 and +3 oxidation states, respectively (Table S16). Apart from the BVS, the oxidation states of all of the atoms in **4** and **4-M** were determined from XPS analysis. The XP spectra of **4-M** revealed the presence of W, Mo, Mn, and oxygen (Figure S31). The two peaks at 641.5 and 653.2 eV in **4-M** can be attributed to the presence of Mn in a +3 oxidation state. The W 4f doublet appears at 34.5 and 36.7 eV, corresponding to W $4f_{7/2}$ and $4f_{5/2}$, and Mo 3d doublet appears at 231.8 and 234.9 eV, corresponding to Mo $3d_{5/2}$ and $3d_{3/2}$, respectively in **4-M**.

The ESI-mass spectrum of **4** in (Figure S33, Table S17) shows the envelope of peaks at m/z 1592.75 (z= –3) due to the presence of fragment $\{Zn_2Mn_2(H_2O)_2(ZnW_9O_{34})_2\}^{3-}$ while a relatively small peak at 1607.07 (z=-3) indicates the presence of analogous structure with W-substituted at the external position. These results have been supported by complementary results in SC-XRD. The analogous mixed addenda POMs structure **4-M** shows the isotopic multiple envelopes of peaks attributed to varying ratios of Mo to W. The mixed addenda sandwich POMs **4-M** show the envelopes of peaks (Figure S34, Table S18) at *m/z* 1576.71 for $[\{Zn_2Mn_2(H_2O)_2(Zn_2MoW_{17})\}^{3-}]$, and *m/z* 1607.73 for $[\{WMn_3(H_2O)_2(Zn_2MoW_{17}O_{68})\}^{3-}]$. EDAX demonstrates that all elements are uniformly distributed with bulk composition as $Na_{10.0}Zn_{4.7}Mn_{1.9}W_{18.7}Mo_{1.2}O_{63.1}$ (Figure S35a). From the atom percentage, it is clear that all the elements are in accordance with the ratio of atomic composition of the crystal structure of **4-M**. This has been further confirmed using powder X-ray diffraction analysis (PXRD). The experimental PXRD patterns are consistent with their simulated pattern (Figure S35b-c), indicating the phase purity of **4** and **4-M**.

From the FT-IR study of O_2-activated **4**, two feeble peaks in the range at 1153, 1207 cm^{-1} have been observed, indicating the formation of O_2 activation using these POMs (Figure S36a). Comparing the stretching frequencies of **4-M** with **4**, there is a subtle variation in the characteristic's peaks at 918 cm^{-1} (**4**, W=O_{term}) to 914 (**4-M**, M=O_{term}, M=Mo/W), 839 cm^{-1} (**4**, W-O-W) to 833 cm^{-1} (**4-M**, M-O-M, M=Mo/W) (Figure S36b). Both **4** and **4-M** exhibit broad absorption bands in the UV-vis region due to LMCT ($O_{2p} \rightarrow W_{5d}$), as well as d-d transitions and sharp peak, is observed for transition MPCT at 470 nm and 527/563 nm (TM → LUMO (W_{5d}/Mn_{3d}) (Figure S36c). Also, a broad peak at 700/733 can be assigned to d-d transition in **4**/**4-M**, respectively. Moreover, the contribution of Mo is evident in mixed addenda sandwich POMs can be explained by the changes

in the band gap (2.31 eV in **4** decreases to 1.65 eV in **4-M**) of these POMs, which were investigated using DRS (Figure 36d-36e).

These results were further supported by DFT studies, where the HOMO-LUMO band gap in **4-M** (representative structure of **4-M** is taken with formula $\{Zn_2Mn_2(H_2O)_2(ZnMo_2W_7O_{34})_2\}^{14-}$ falls lower than that of **4** (Figure S37). Interestingly, LUMO/LUMO+1 of **4** lies at Mn(3+) while LUMO+2 lies at W(6+) centre, which also supports UV-visible spectroscopy, e.g., MPCT at 470 nm can be assigned to TM → W and peak at 527 nm stands for TM → Mn^{3+} in **4** (Figure S38). In **4-M**, LUMO lies at Mn while LUMO+1 lies at Mo(6+) (Figure S39). Thus, in **4-M**, MPCT at 470 nm can be assigned to TM → Mo, and the peak at 527 nm stands for TM → Mn^{3+} in **4-M.** Thus, the incorporation of Mn at the internal sandwich position is responsible for the MPCT in these POMs, while mixed addenda change the electron density in LUMO, which lies at Mo rather than W, thus decreasing the overall band gap. The solution state UV-visible study of **4** for 24 hours shows no change in absorbance, thus reflecting its stability in aqueous solution for longer periods (Figure S40). Thermal stability was determined by TGA analysis from 30 to 600 °C (Figure S41). The TGA curve of **4/4-M** shows high thermal stability up to 600 °C. The first weight loss was observed below 200 °C, attributed to the release of water of crystallization. The small weight loss in 320-350 °C range can be attributed to release of water molecules coordinated to the counter cations outside the framework.

Characterizations of 5 and 5-M.

Table S19. Crystal data, data collection, and refinement parameters for **5** and **5-M**

	5	**5-M**
CCDC number	**2330255**	**2330245**
empirical formula	$Co_8Mn_4Na_{24}O_{216}W_{36}$	$Co_{3.8}Mn_2Mo_{0.4}Na_{13}O_{108}W_{17.8}$
formula weight	11317.56	5671.59
temp (K)	273.15	273.15
crystal system	monoclinic	monoclinic
space group	$P2_1/n$	$P2_1/n$
unit cell dimension		
a (Å)	13.090(4)	13.1630(17)
b (Å)	17.795(6)	17.768(3)
c (Å)	21.125(8)	21.106(3)
α (deg)	90	90
β (deg)	93.497(11)	93.538(5)
γ (deg)	90	90
V (Å^3)	4912(3)	4926.7(12)
Z	1	2
ρ (calcd.) (g/cm^3)	3.826	3.823
μ/mm^{-1}	22.061	21.782
F (000)	4972.0	4987.0
crystal size (mm^3)	0.27 × 0.22 × 0.21	0.23 × 0.21 × 0.14
2Θ range for data collection/°	3.86 to 54.98	3.87 to 55.07
index ranges	-16 ≤ h ≤ 14, -23 ≤ k ≤ 22, -27 ≤ l ≤ 27	-16 ≤ h ≤ 17, -23 ≤ k ≤ 23, -27 ≤ l ≤ 27
no. of reflection collected /unique	44097/11194	50057/11315
GOF on F^2	1.060	1.046
R(int)	0.058	0.057
final *R* indices ($I > 2\sigma(I)$)	R_1 = 0.0338, wR_2 = 0.0873	R_1 = 0.0382, wR_2 = 0.0870
R indices (all data)	R_1 = 0.0417, wR_2 = 0.0923	R_1 = 0.0541, wR_2 = 0.0961
data/restraints/param	11194/0/658	11315/0/665
Largest diff. peak/hole / e Å^{-3}	2.56/-1.57	1.86/-1.96

Table S20. BVS of selected atoms calculated from the SC-XRD structure of **5** and **5-M**			
POMs	Transition metal	Bond valence sum value	Oxidation state
5	W	6.05	+6
	Co1	2.11	+2
	Co2	2.01	+2
	Mn1	3.00	+3
5-M	W	6.05	+6
	Mo	6.11	+6
	Co1	2.12	+2
	Co2	2.32	+2
	Mn1	3.03	+3

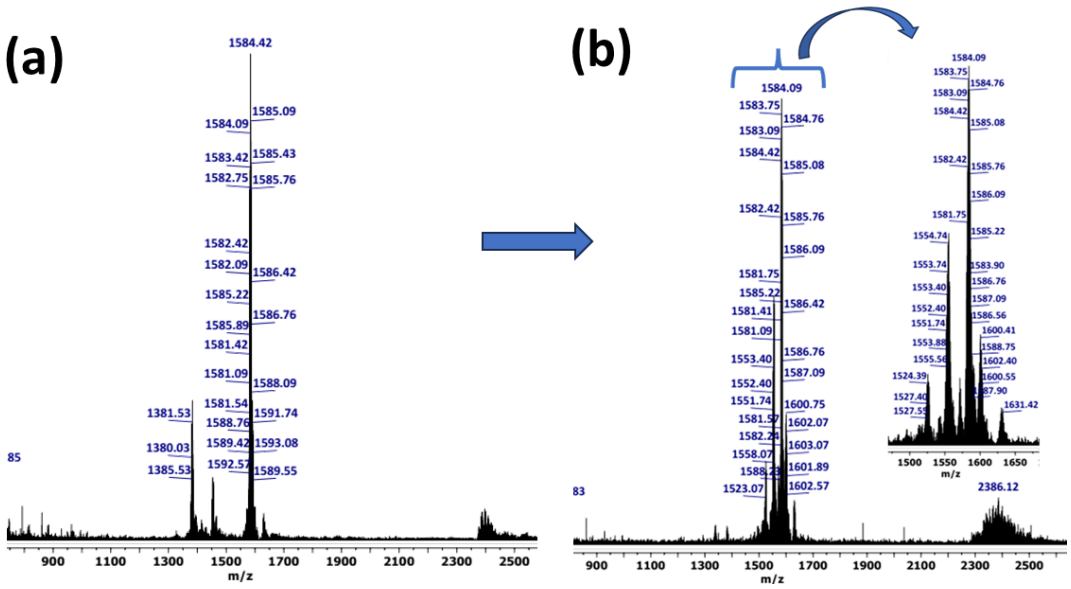

Figure S42. ESI-MS spectra of (a) **5** (b) **5-M** in the range of m/z 900-2500 (z = –3).

Table S21. Assignment of ESI-mass peaks of 5/5-M

Charge	m/z (obs.)	m/z (calc.)	Mol. Wt.	Assigned probable formula
-3	1584.09	1584.46	4753.38	$H_{11}Co_2Mn_2(Co_2W_{18}O_{68})$
-3	1554.74	1555.11	4665.34	$H_{11}Co_2Mn_2(Co_2MoW_{17}O_{68})$
-3	1524.39	1524.43	4573.31	$H_{11}CoMn_3(Co_2Mo_2W_{16}O_{68})$
-3	1600.41	1601.10	4803.31	$H_5NaMn_3W(Co_2MoW_{17}O_{68})$
-3	1631.42	1632.11	4896.35	$H_6NaCoWMn_2(Co_2W_{18}O_{68})$

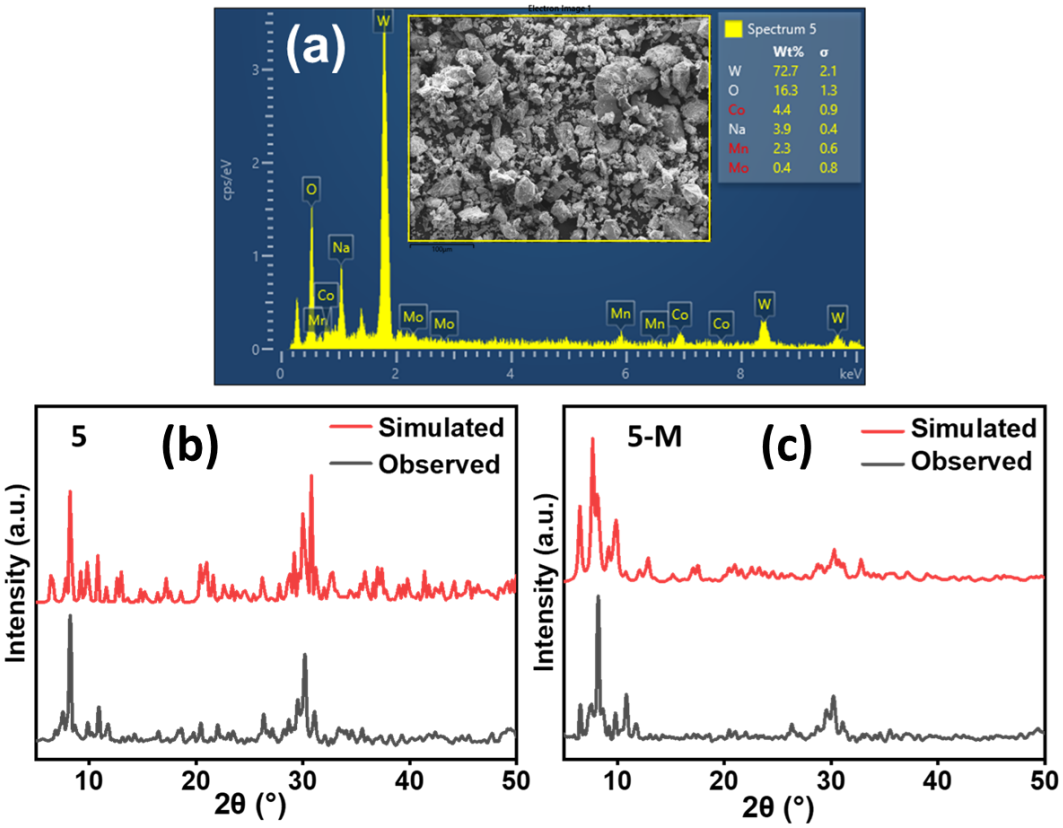

Figure S43. (a) EDX mapping for **5-M**; Observed PXRD pattern and comparison with the simulated data obtained from single crystal XRD for (b) **5** (c) **5-M.**

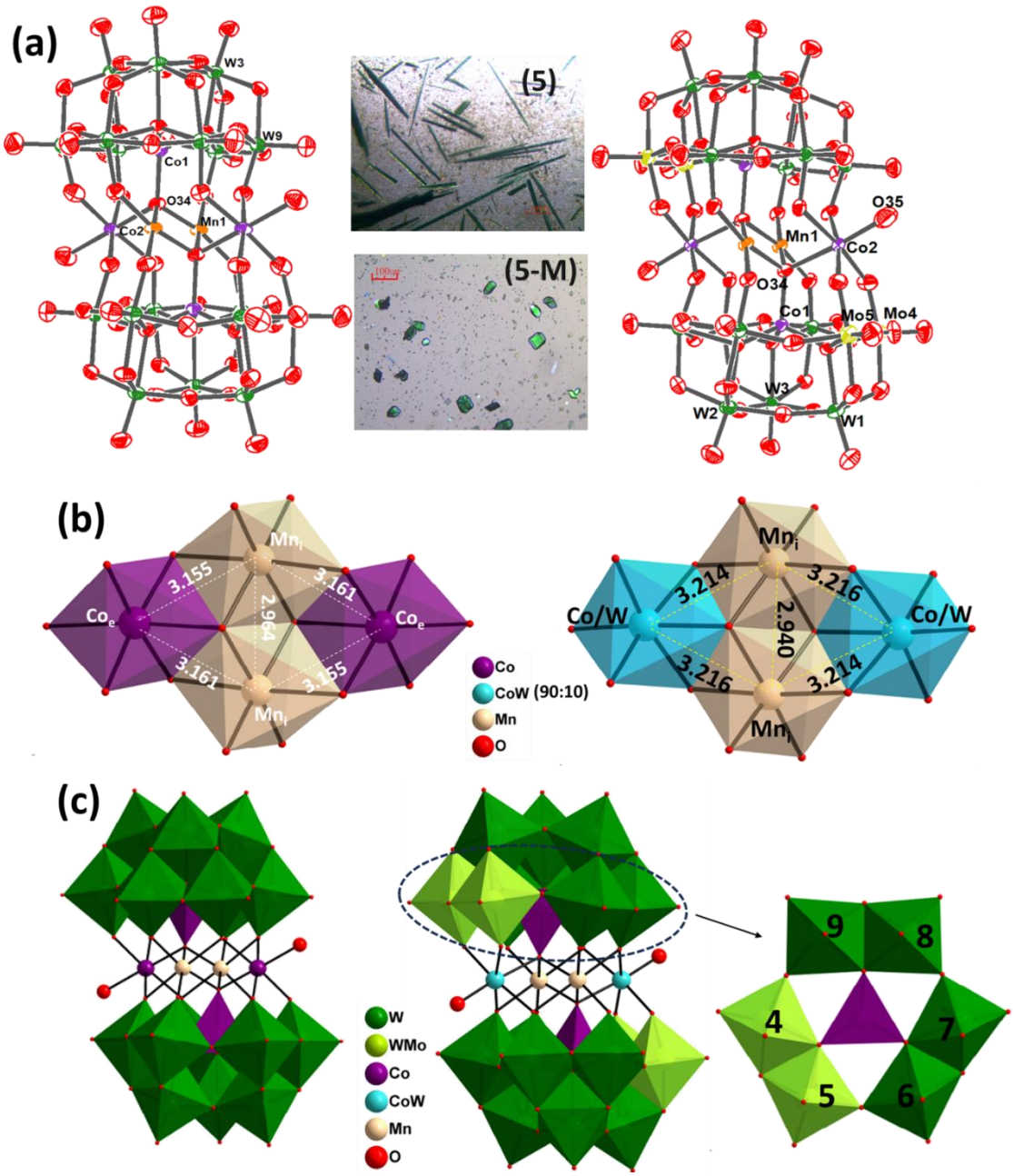

Figure S44. (a) ORTEP drawing (with 60% ellipsoid probability) and Optical images of sandwich POMs; **5** (left) and **5-M** (right); (b) Cubane core showing the interatomic distance between transition metals in **5** (left) and **5-M** (right); (c) combined polyhedral/ball and stick representation of the single-crystal X-ray structure of polyoxometalate **5** (left) and **5-M** (right), belt 2 depicting different ratios of molybdenum to tungsten in **5-M**; Countercations and hydrogen atoms are omitted for clarity.

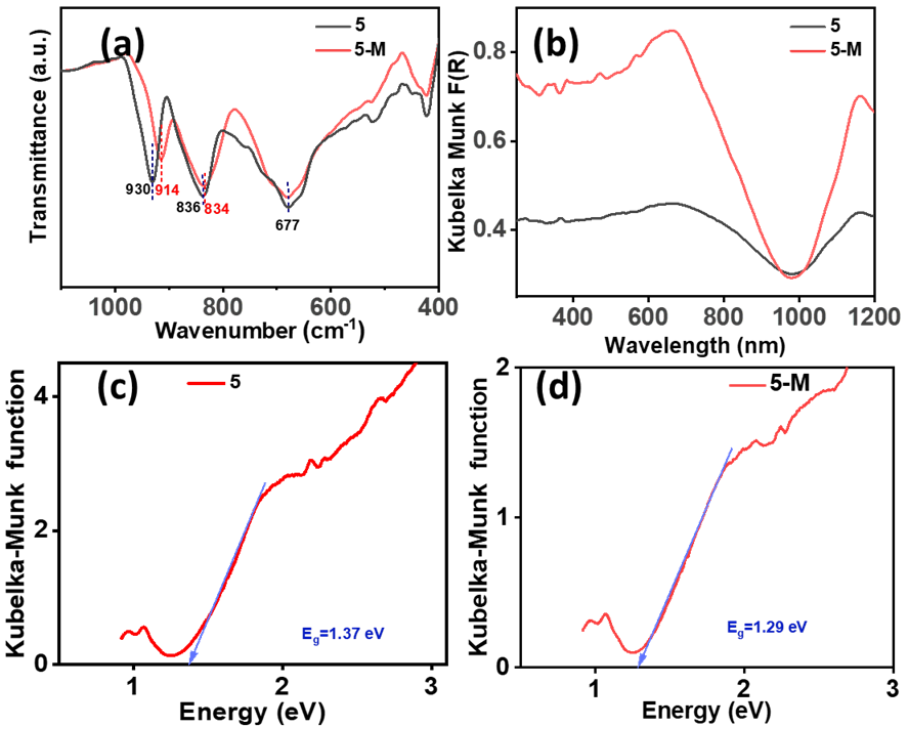

Figure S45. (a) FT-IR and (b) solid-state UV-vis spectra of **5** and **5-M** and corresponding optical band-gap derived from the Kubelka-Munk equation in (c) **5** and (d) **5-M**.

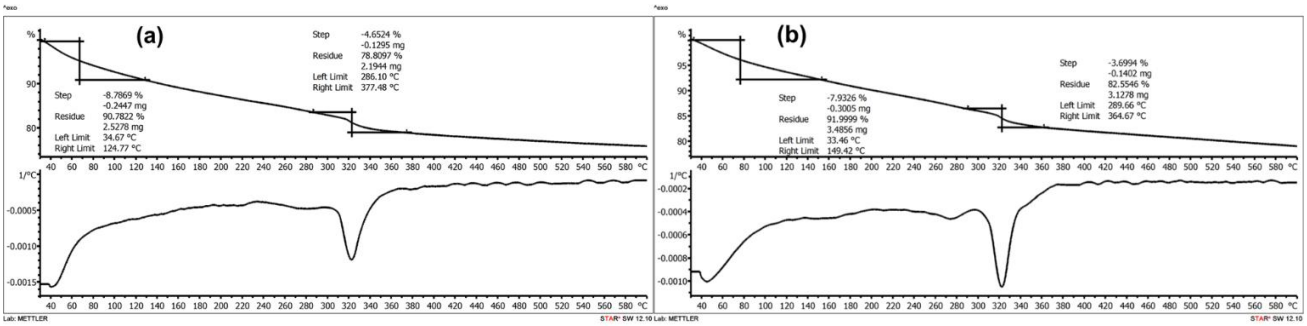

Figure S46. TGA curve along with corresponding first derivative of (a) **5** (b) **5-M**.

Characterization analysis **of 5 and 5-M**

Compounds **5** and **5-M** were characterized using SC-XRD, FT-IR, ESI-MS, and UV-visible spectroscopy (Figure S42-S46). The framework structure was confirmed by SC-XRD (**CCDC 2330255, 2330245).** The dark green colored crystals (Figure S44a) of **5** (needle-shaped) and **5-M** (cubic) crystallize in monoclinic with $P2_1/n$ space group (Table S19). The 3D SC-XRD structure of **5** and **5-M** shows that the trilacunary Keggin moiety contains a tetrahedrally bound cobalt atom in the center as a templating agent to triads of addenda W/Mo atoms. The tetrasubstituted sandwich core consists of Mn at the internal $\{TM_i\}$ position and Co/W (90:10) as external atoms $\{TM_e\}$ (Figure S44a). From the comparison of **5-M** with the reference structure (Figure S1), it is clear that Mo incorporation is favorable at only 4/5 positions of the belt similar to **4-M**, which are connected to transition metals in the sandwich position through μ_2 oxygens (Figure S44c). The other positions in the cap and belt are not favorable for Mo incorporation. The distance between Co atoms at the external and Mn at the internal positions is 3.15 Å in **5** while 3.21 Å in **5-M**, however, the distance between Mn atoms in the internal positions

is 2.9 Å in **5**/**5-M** (Figure S44b). BVS calculation indicates that all addenda atoms are in their highest oxidation state +6 and Co, and Mn in +2, +3 oxidation state respectively (Table S20).

ESI-mass spectrum of **5** in (Figure S42a) shows the envelope of peaks at m/z 1584 (z=–3) for the fragment [$\{Co_2Mn_2(H_2O)_2(CoW_9O_{34})_2\}^{3-}$], while the analog mixed addenda **5-M** structure shows the isotopic multiple envelopes of peaks attributed to varying ratios of Mo to W with maximum 2 Mo incorporated in the framework. **5-M** show the envelopes of peaks (Figure S42b, Table S21) at *m*/*z* 1554 for $[H_{11}\{Co_2Mn_2(CoMoW_{17}O_{68})\}]^{3-}$, and *m*/*z* 1524 for $[H_{11}\{Co_2Mn_2(CoMo_2W_{16}O_{68})\}]^{3-}$ while the incorporation of W at external sandwich position is indicated by the small peaks at 1631 due to fragments $[H_6Na\{CoWMn_2(Co_2W_{18}O_{68})\}]^{3-}$ with corresponding mixed addenda peaks at 1600 due to probable fragment $[H_7Na\{WMn_3(Co_2MoW_{17}O_{68})\}]^{3-}$. Comparing the stretching frequencies of **4-M** with **4**, there is a subtle variation in the characteristic's peaks at 930 cm^{-1} (**5**, $W{=}O_{term}$) to 914 (**5-M**, $M{=}O_{term,}$ M=Mo/W), 836 cm^{-1} (**5**, W-O-W) to 834 cm^{-1} (**5-M**, M-O-M, M=Mo/W) (Figure S45a). EDAX demonstrates that all elements are uniformly distributed with bulk composition as $Na_{10.0}Co_{4.4}Mn_{2.4}W_{23.1}Mo_{0.3}O_{59.8}$ (Figure S43a). From the atom percentage, it is clear that all the elements are in accordance with the ratio of atomic composition of the crystal structure of **5-M**. This has been further confirmed using powder X-ray diffraction analysis (PXRD). The experimental PXRD patterns are consistent with their simulated pattern (Figure S43b-c), indicating the phase purity of **5** and **5-M**.

Both **5** and **5-M** exhibit broad absorption bands in the UV-vis region due to (LMCT) (O2p → W5d), d-d transitions as well absorption in Near IR region (Figure S45b-d). The peak at 660/666 nm can be assigned to d-d transition in 5/5-M, respectively, while peaks at 1160 nm can be assigned to NIR absorption. Interestingly, Mo incorporation has very little effect on its absorption properties, which can be further confirmed from the band gap calculated from DRS (slight change in band gap; 1.37 eV in **5** to 1.29 eV in **5-M**). Thermal stability was determined by TGA analysis from 30 to 600 °C (Figure S46). The TGA curve of **9**/**10** shows thermal stability even up to 300 °C. The first weight loss was observed in the range of 30-150 °C attributed to the release of water of crystallization. The small weight loss in range of 300-340 °C is attributed to the release of water molecules coordinated to the counter cations outside the POM framework.

Characterizations of 6, 6-M, 7 and 8.

Table S22. Crystal data, data collection, and refinement parameters for **6-M, 7** and **8.**

	6-M	**7**	**8**
CCDC number	**2330256**	**2330257**	**2330261**
empirical formula	$Fe_4Mo_{2.7}Na_{19}O_{116}W_{17.3}Zn_3$	$Co_4Fe_{5.7}H_4Na_{13}O_{108}W_{18.3}$	$Mn_5Na_{11.5}O_{108}W_{18.9}Zn_{4.1}$
formula weight	6151.96	5945.39	6009.87
temp (K)	273.15	298.15	273.15
crystal system	Triclinic	Triclinic	Triclinic
space group	$P\bar{1}$	$P\bar{1}$	$P\bar{1}$
unit cell dimension			
a (Å)	12.8944(4)	12.4815(10)	12.6032(8)
b (Å)	13.6975(5)	13.6112(12)	13.7217(9)
c (Å)	16.9682(6)	16.6742(15)	16.8765(12)
α (deg)	113.3020(10)	82.635(3)	82.363(2)
β (deg)	96.6120(10)	73.593(3)	73.401(2)
γ (deg)	94.7230(10)	64.249(2)	64.088(3)
V (Å^3)	2707.18(16)	2447.5(4)	2515.7(3)
Z	1	1	1
ρ (calculated) (g/cm^3)	3.774	4.034	3.967
μ/mm^{-1}	19.961	23.058	23.235
F (000)	2725.0	2617.0	2637.0
crystal size (mm^3)	0.23 × 0.18 × 0.12	0.39 × 0.26 × 0.21	0.38 × 0.22 × 0.17
2Θ range for data collection/°	4.25 to 52.85	4.17 to 52.91	4.13 to 52.93
index ranges	-16 ≤ h ≤ 16, -17 ≤ k ≤ 17, -21 ≤ l ≤ 21	-15 ≤ h ≤ 15, -17 ≤ k ≤ 17, -20 ≤ l ≤ 20	-15 ≤ h ≤ 15, -17 ≤ k ≤ 17, -21 ≤ l ≤ 21
no. of reflection collected /unique	42479/ 11075	65901/10068	44095/10330
GOF on F^2	1.121	1.118	1.075
R(int)	0.044	0.054	0.042
final *R* indices ($I > 2\sigma(I)$)	R_1 = 0.0448, wR_2 = 0.0371	R_1 = 0.0365, wR_2 = 0.0871	R_1 = 0.0246, wR_2 = 0.0657
R indices (all data)	R_1 = 0.0334, wR_2 = 0.0811	R_1 = 0.0395, wR_2 = 0.0888	R_1 = 0.0262, wR_2 = 0.0668
data/restraints/param	11075/1/764	10068/1/682	10330/1/686
Largest diff. peak/hole / e Å^{-3}	2.66/-1.53	2.13/-1.61	1.25/-1.58

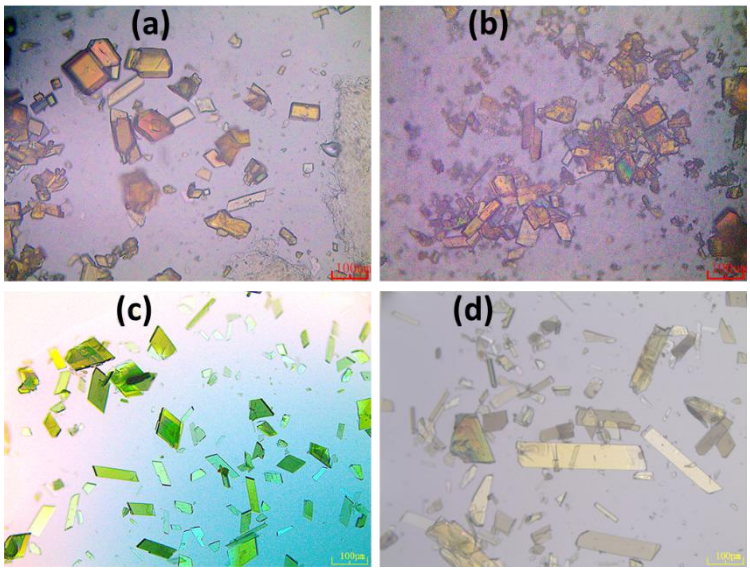

Figure S47. Optical images of sandwich POMs; (a) **6** (b) **6-M** (c) **7** and (d) **8.**

Table S23. Bond valence parameter of selected atoms calculated from the SC-XRD structure of framework structures **6-M, 7** and **8**

POMs	Transition metal	Bond valence sum value	Oxidation state
6-M	W	6.03	+6
	Mo	6.16	+6
	Zn1	2.34	+2
	Zn3	2.31	+2
	Fe1	3.03	+3
	Fe2	3.01	+3
7	W	6.06	+6
	Fe1	3.05	+3
	Fe2	2.23	+2
	Fe3	2.33	+2
	Co1	2.22	+2
	Co2	2.04	+2
8	W	6.04	+6
	Zn1	2.23	+2
	Zn2	2.54	+2
	Zn3	2.20	+2
	Mn3	2.46	+2
	Mn4	2.26	+2
	Mn1	2.23	+2

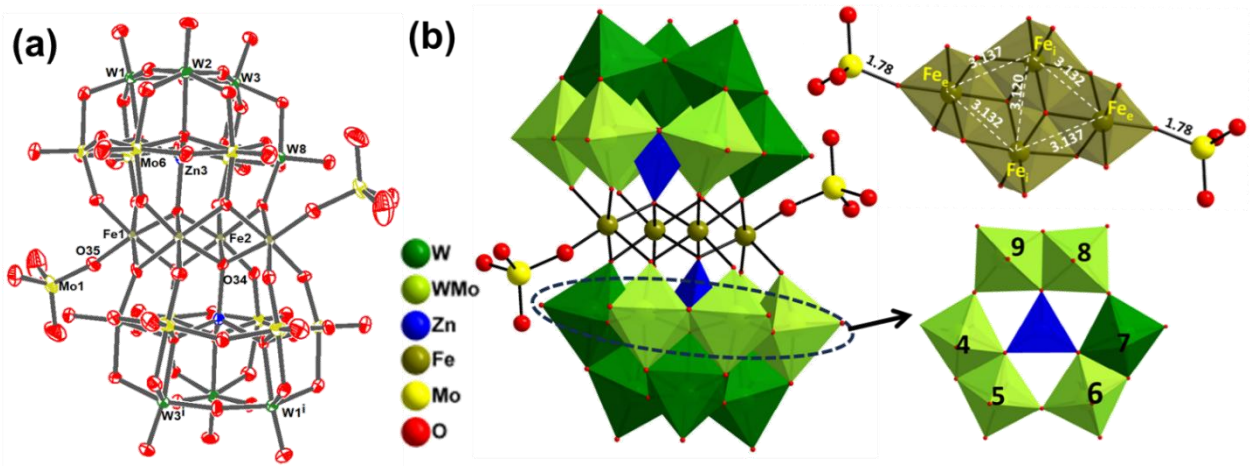

Figure S48. (a) ORTEP drawing (with 60% ellipsoid probability) (b) Cubane core showing the interatomic distance between transition metals in **6-M**; combined polyhedral/ball and stick representation of the single-crystal X-ray structure of polyoxometalate **6-M**; belt 2 depicting different ratios of molybdenum to tungsten in **6-M,** Countercations and hydrogen atoms are omitted for clarity.

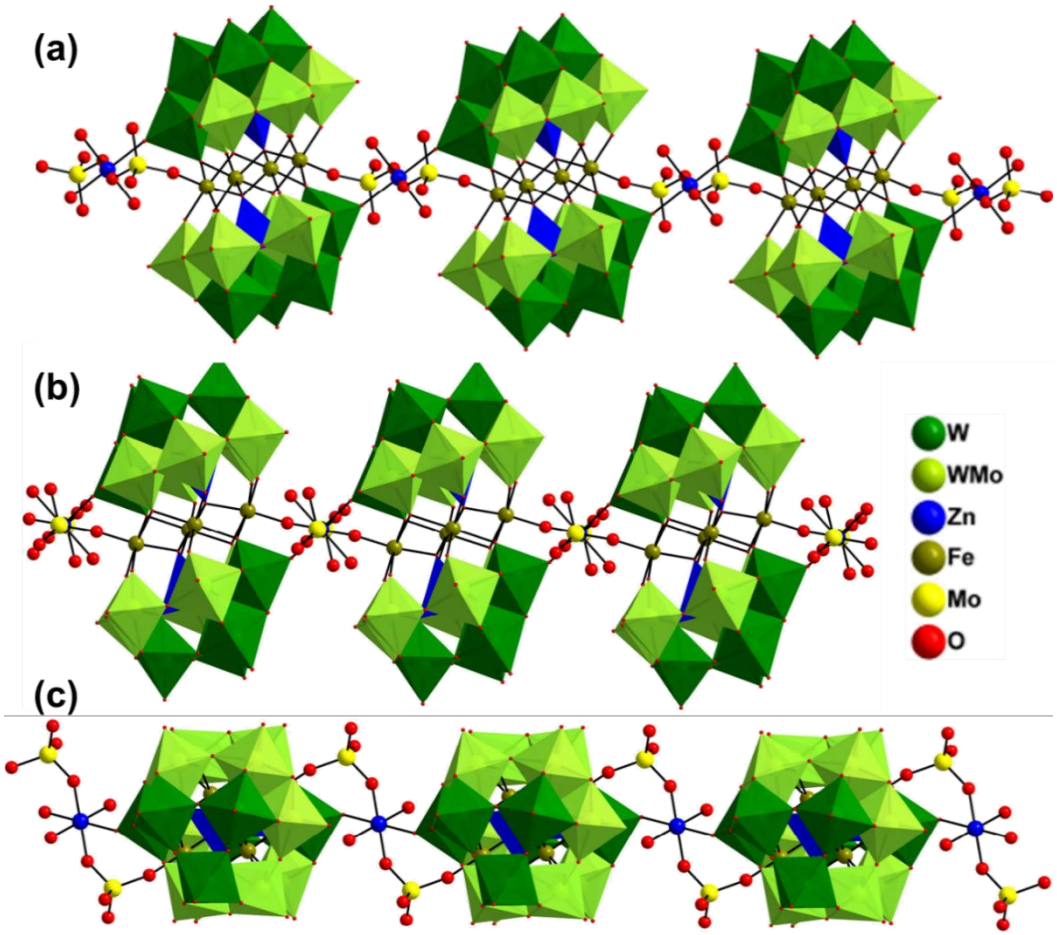

Figure S49. Combined polyhedral/ball-and-stick representation of **6-M** anion with different views. (b) different coordination environment of the **6-M** unit. (c) Perspective view of the three-dimensional chain connected by linker $ZnMo_2O_{10}$; sodium and hydrogen are omitted for clarity.

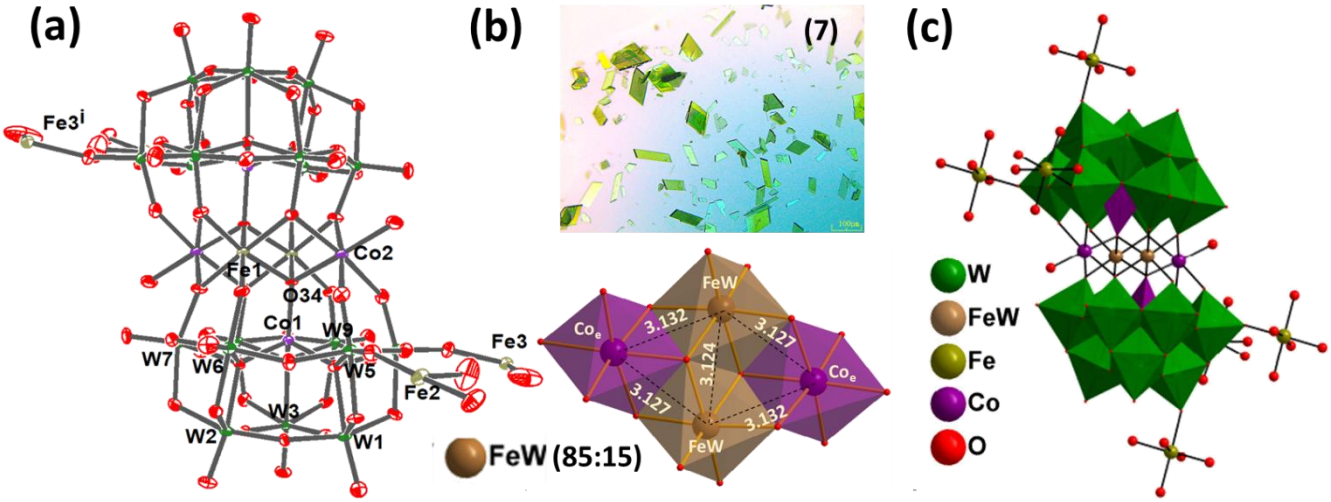

Figure S50. (a) ORTEP drawing (with 60% ellipsoid probability) (b) Optical images of sandwich POMs; **7** and Cubane core showing the interatomic distances between transition metals in **7**; (c) combined polyhedral/ball and stick representation of the single-crystal X-ray structure of **7** showing different coordination mode of POM framework; Countercations and hydrogen atoms are omitted for clarity.

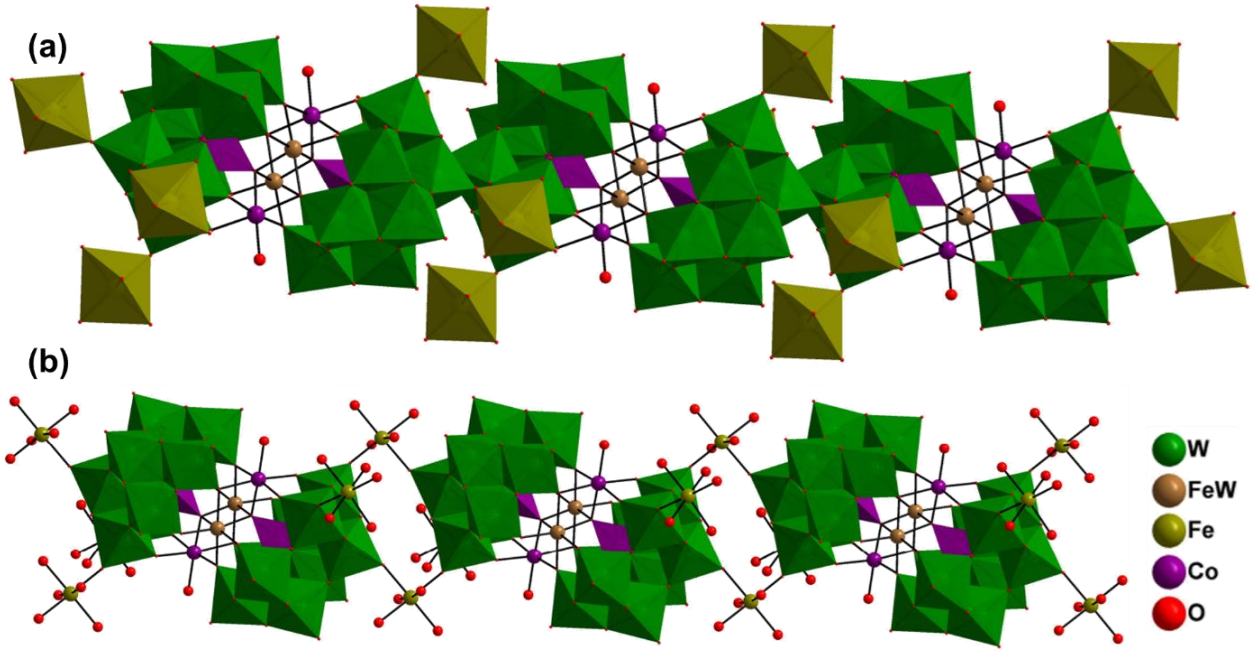

Figure S51. (a) Combined polyhedral/ball-and-stick representation of **7** anions, (b) Perspective view of the three-dimensional chain connected by Fe atoms; sodium and hydrogen are omitted for clarity.

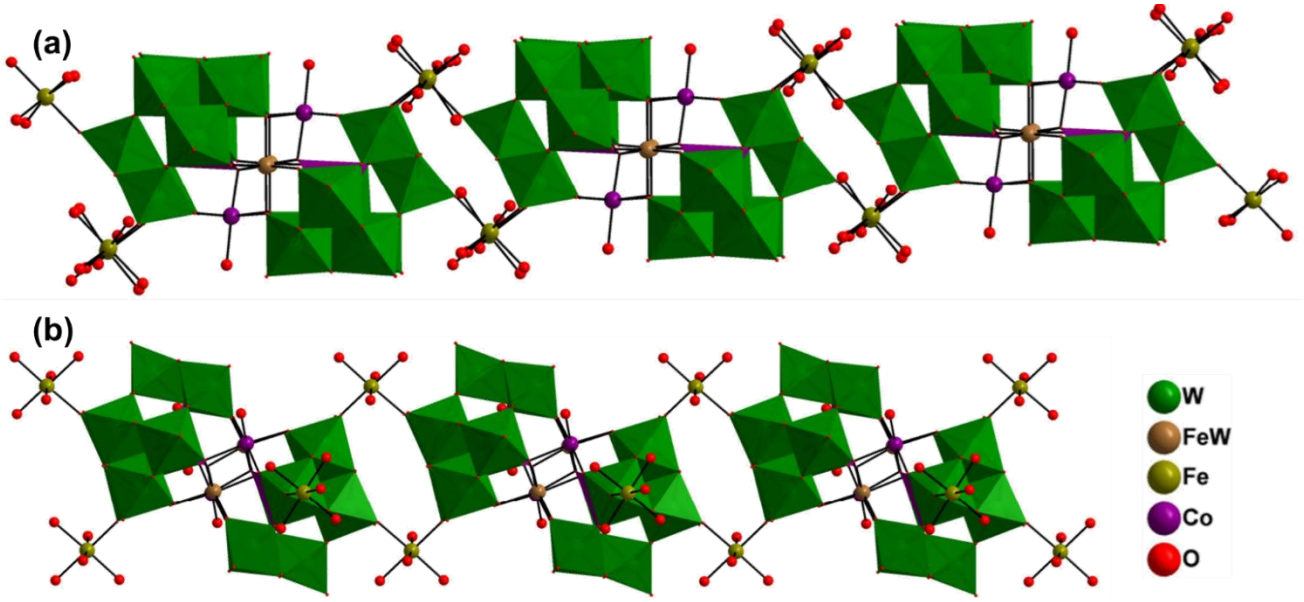

Figure S52. (a) Combined polyhedral/ball-and-stick representation of **7** with different views (c) Perspective view of the three-dimensional chain connected by linker Fe atoms; sodium and hydrogen are omitted for clarity.

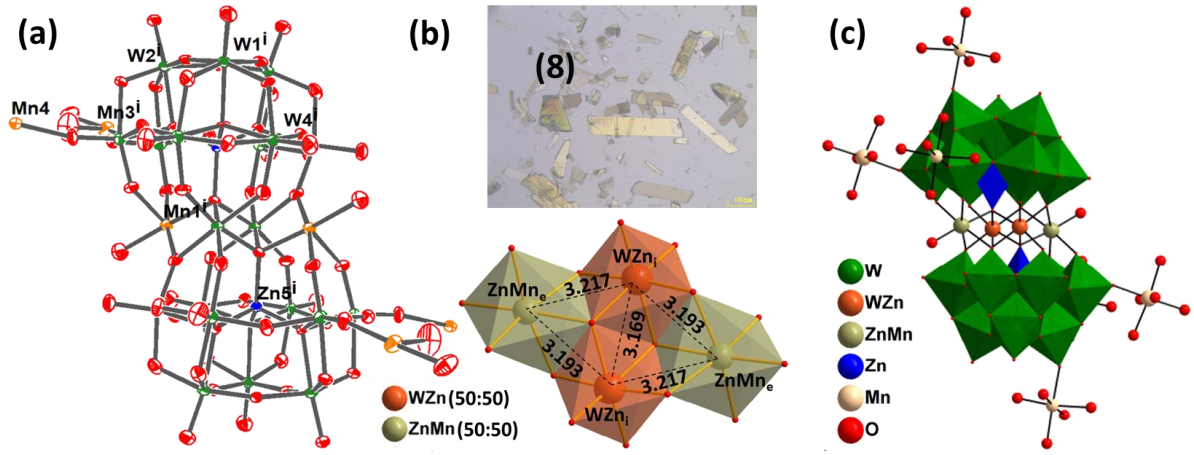

Figure S53. (a) ORTEP drawing (with 60% ellipsoid probability) (b) Optical images of sandwich POMs; **8** and Cubane core showing the interatomic distance between transition metals in **8**; (c) combined polyhedral/ball and stick representation of the single-crystal X-ray structure of polyoxometalate **8** showing different coordination mode of POM framework; Countercations and hydrogen atoms are omitted for clarity.

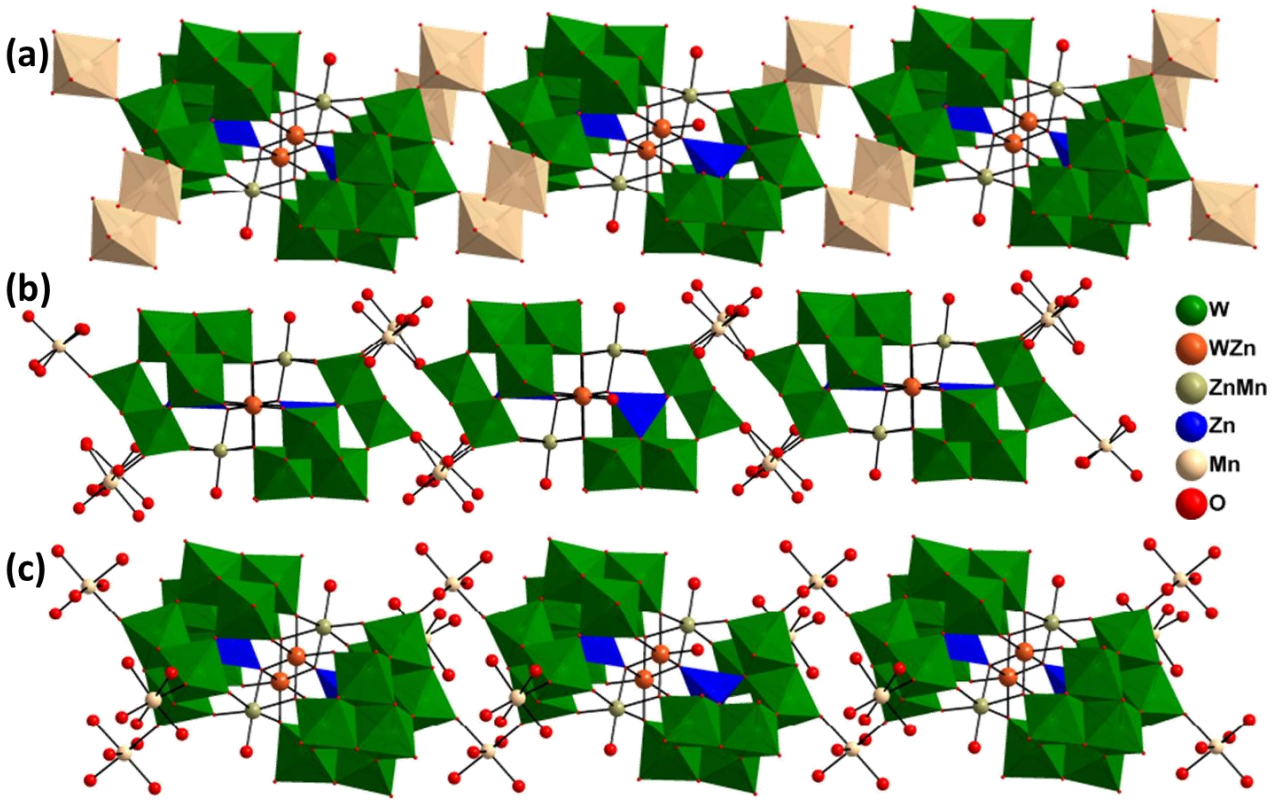

Figure S54. (a) Polyhedral and (b) Combined polyhedral/ball-and-stick representation of **8** with different views (c) Perspective view of the three-dimensional chain of **8** connected by linker Zn/Mn; sodium and hydrogen are omitted for clarity.

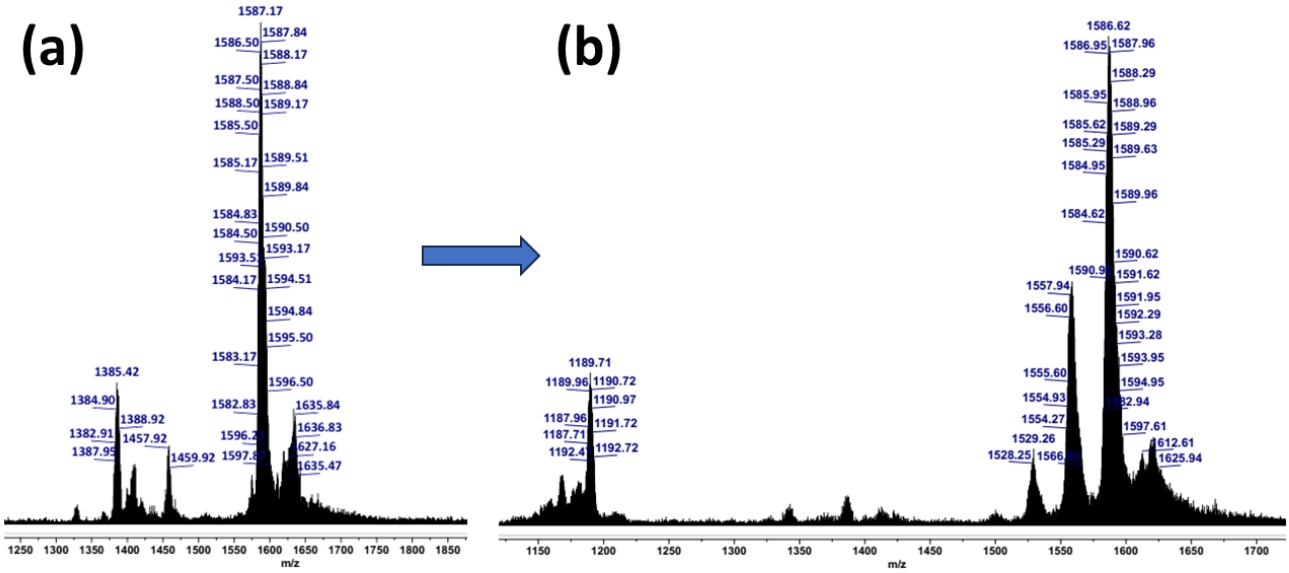

Figure S55. ESI-MS spectra of **6** (a) and **6-M** (b) in the range of m/z 1100-1850 (z = –3).

Table S24. Assignment of ESI-mass peaks of **6/6-M**

Charge	m/z (obs.)	m/z (calc.)	Mol. Wt.	Assigned probable formula
-3	1587.17/1586.62	1586.79	4760.38	$H_9Fe_4(Zn_2W_{18}O_{68})$
-3	1557.94	1557.44	4672.34	$H_{11}Fe_4(Zn_2MoW_{17}O_{68})$
-3	1528.25	1528.10	4584.30	$H_{11}Fe_4(Zn_2Mo_2W_{16}O_{68})$
-4	1189.71	1189.84	4759.37	$H_8Fe_4(Zn_2W_{18}O_{68})$

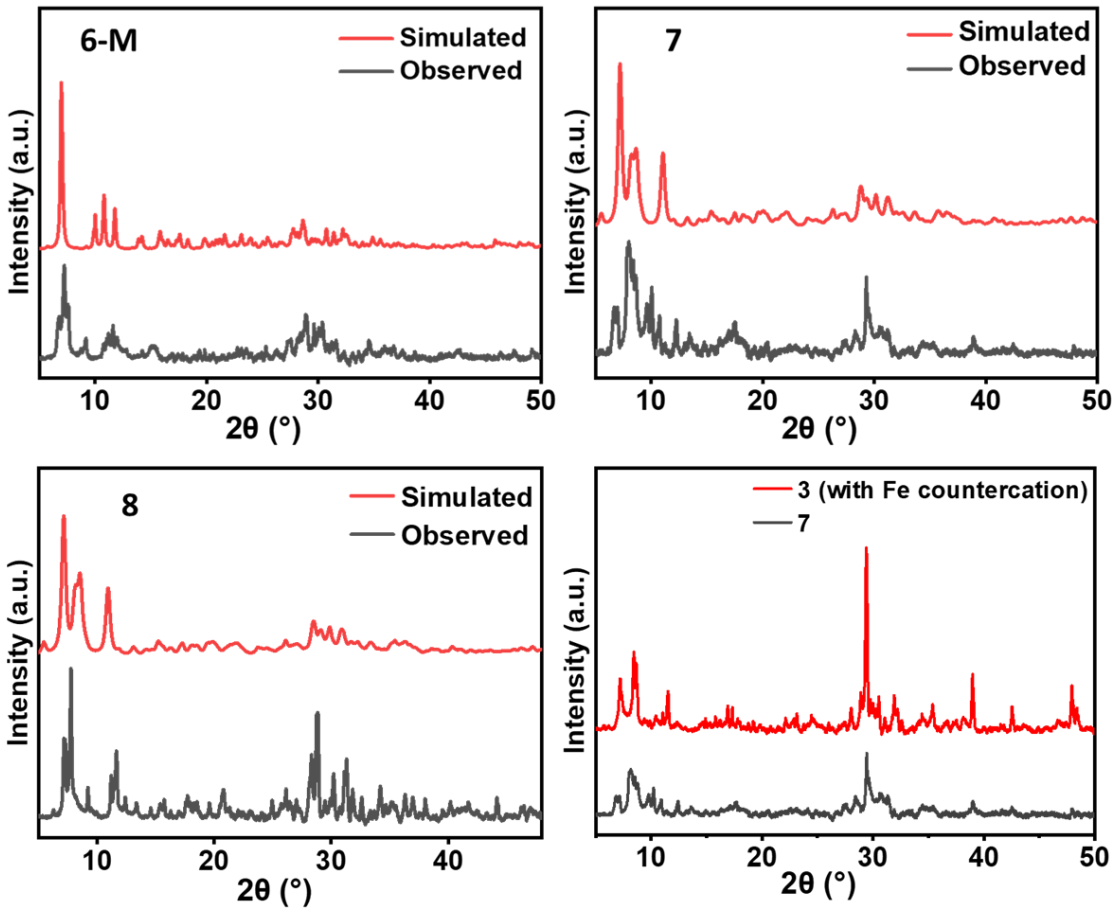

Figure S56. Simulated and experimental powder XRD of **6-M**, **7**, **8**, and comparison of PXRD of **7** and countercation exchange with Fe in **3**.

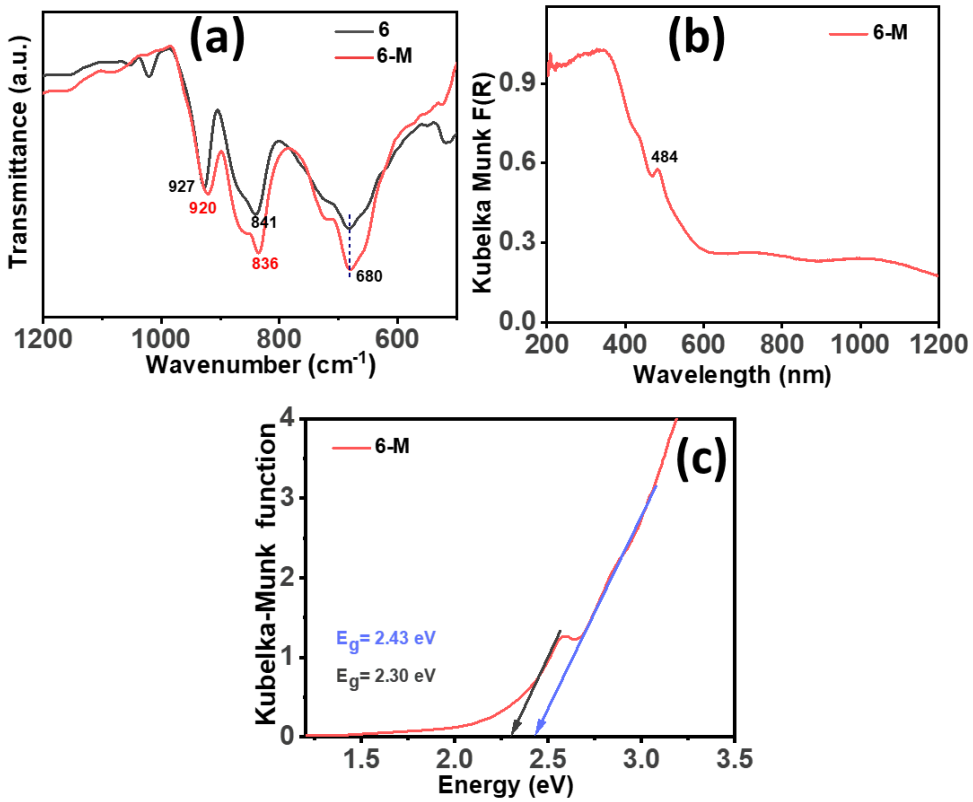

Figure S57. (a) Effect of Mo incorporation in the framework of tetrasubstituted sandwich POMs in terms of shifting of characteristics peaks in FT-IR of **6-M** (b); solid-state UV-vis spectra and (b) optical band-gap derived from the Kubelka-Munk equation in **6-M**.

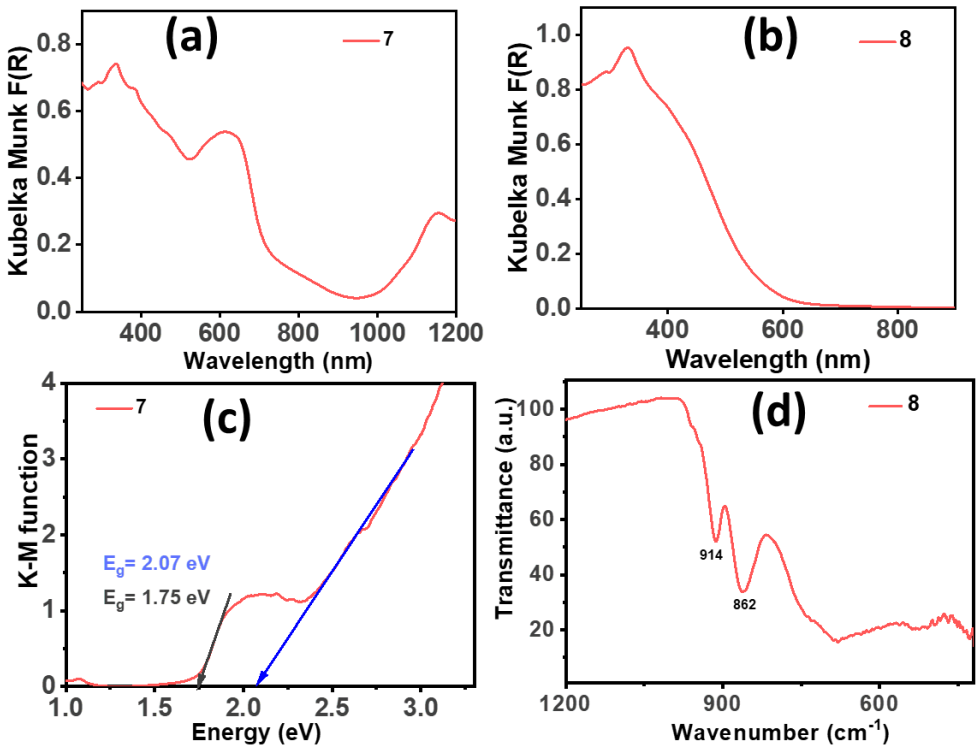

Figure S58. solid-state UV-vis spectra of (a) **7** (b) **8**; (c) optical band-gap derived from the Kubelka-Munk equation in **7** and (d) FT-IR spectra of **8**.

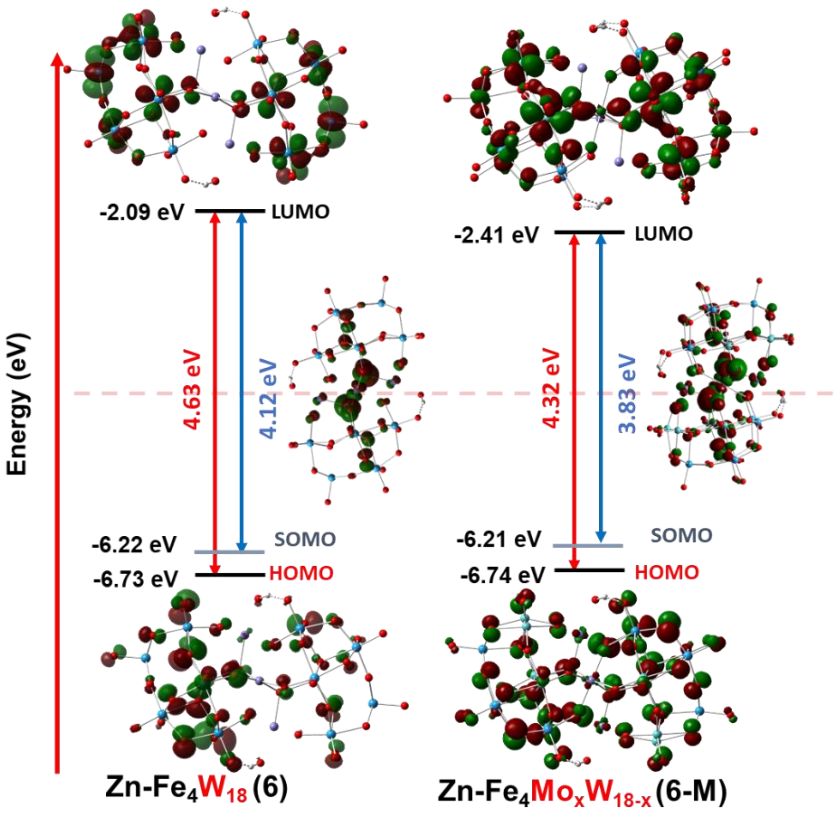

Figure S59. Frontier molecular orbitals of tetrasubstituted sandwich POMs showing the effect of Mo doping on band gaps as well as shifting of electron density on addenda atoms in **6** and **6-M**.

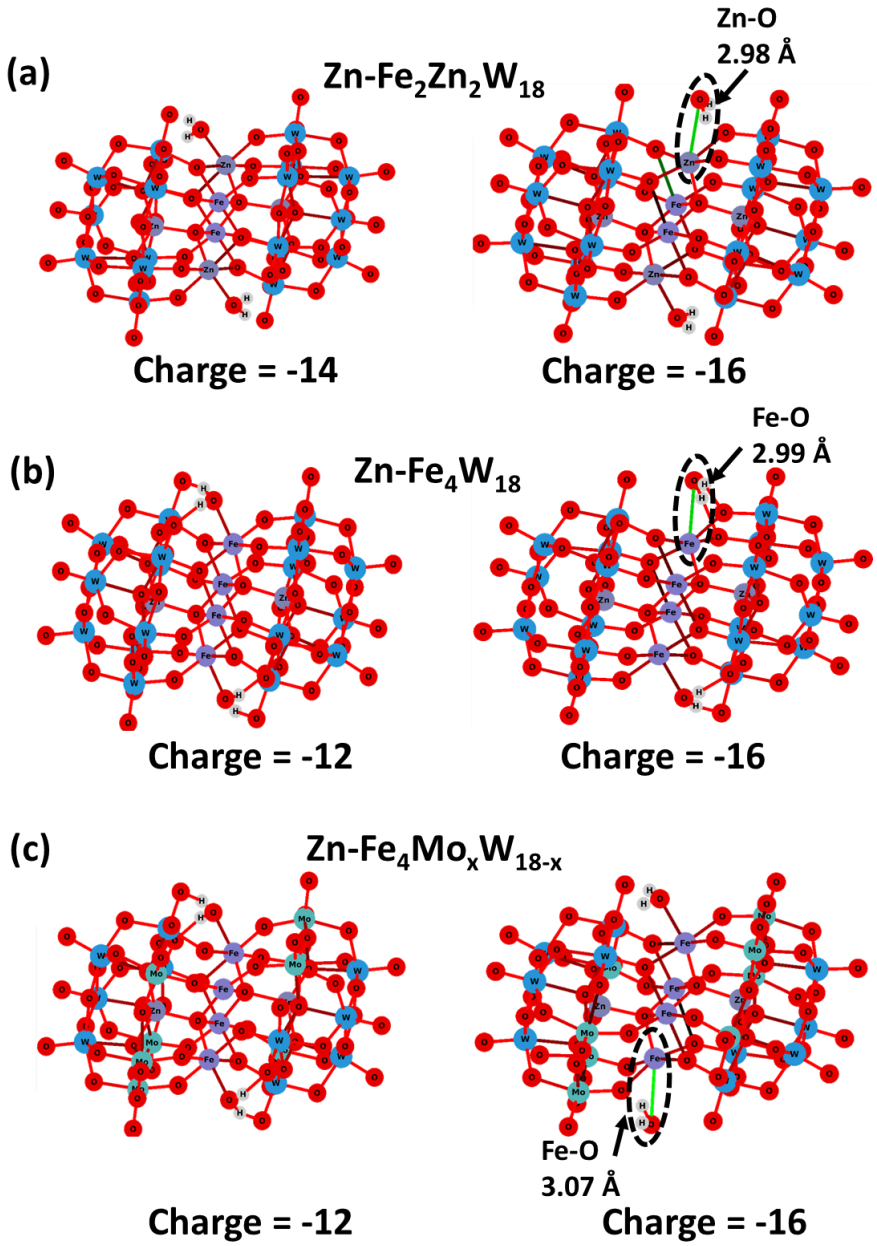

Figure S60. DFT optimized auxiliary structure of sandwich POMs with the general formula (a) $[Zn_2Fe_2(H_2O)_2(ZnW_9O_{34})_2]^{n-}$ where n=14/16 (b) $[Fe_4(H_2O)_2(ZnW_9O_{34})_2]^{n-}$ where n=12/16 (c) $[Fe_4(H_2O)_2(ZnMo_xW_{9-x}O_{34})_2]^{n-}$ where n=12/16 showing elongated bond lengths (shown in green color).

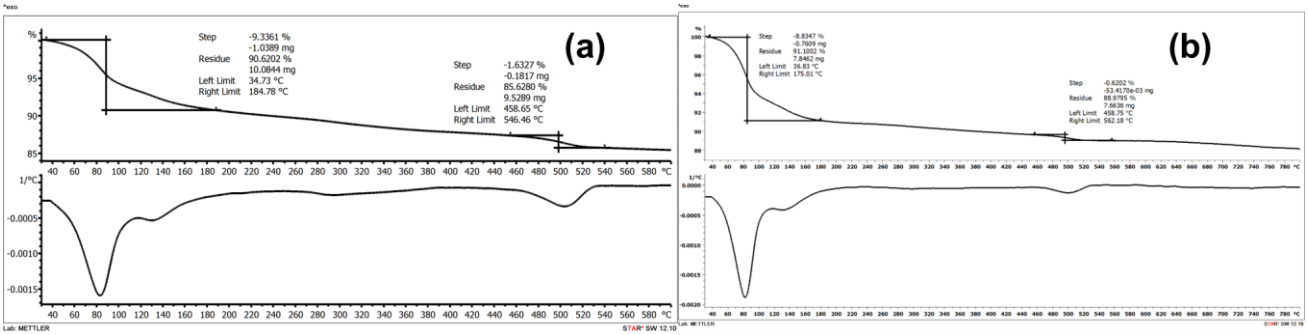

Figure S61. TGA curve along with corresponding first derivative of (a) **6** (b) **6-M**.

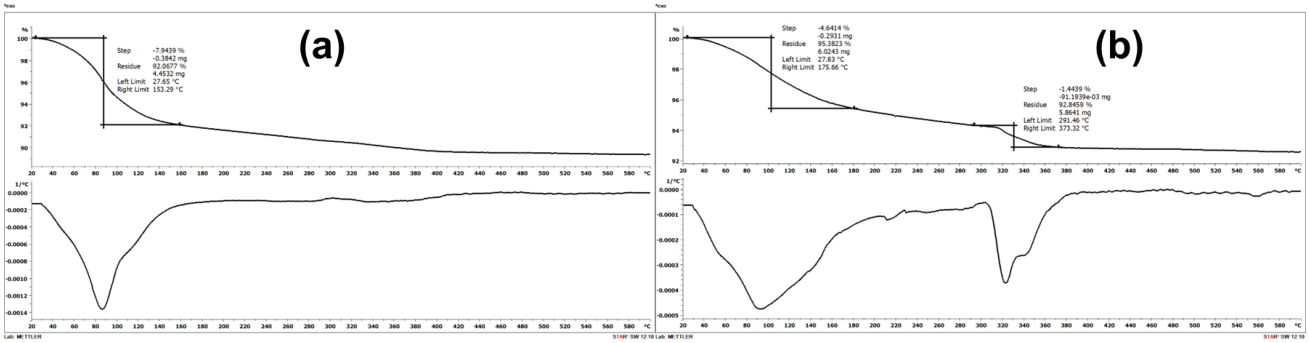

Figure S62. TGA curve along with corresponding first derivative of (a) **7** (b) **8**.

Characterization analysis of 6, 6-M, 7 and 8

Compounds **6-M, 7** and **8** were characterized using SC-XRD, FT-IR, ESI-MS, PXRD, and UV-vis spectroscopy (Figure S47-S62). The framework structure was confirmed by SC-XRD (**CCDC 2330256, 2330257 and 2330261).** All these crystallize in triclinic lattice with $P\overline{1}$ space group (Table S22). The optical image of **6** and **6-M** shows light yellow colored crystals with rectangular shapes, however, it was observed that data collection at room temperature was not feasible for **6** as it gives poor diffractions (Figure S47a/S47b). Compound **6** was characterized using FT-IR and ESI-MS. The crystal structure of **6-M** shows that the trilacunary Keggin moiety contains a tetrahedrally bound Zn atom in the center as a templating agent to triads of addenda W/Mo atoms. The tetrasubstituted sandwich core consists of four Fe atoms (Figure S48b). The crystal structure of 6-M shows that it forms a three-dimensional network structure with POM frameworks connected using transition metal ligands with the formula $ZnMo_2O_{10}$ (Figure S49). Interestingly, the Mo atom of the ligand connects to the oxygen of the Fe atom in the sandwich position in a tetrahedral way, thus making it coordinatively saturated. The two tetrahedrally bound Mo atoms further connect to the Zn atom (octahedrally connected between the two POM frameworks), thus forming the linker between the two POM frameworks. The octahedrally bound Zn atom connects two sides with the Mo atom through oxygen, two water molecules, and two sides are directly connected to the W of the POM framework through oxygen atoms. From the comparison of **6-M** with the reference structure (Figure S1), Mo incorporation is favorable at all belt positions except position 7; however, positional occupancy is very low (less than 15%) (Figure S48b). The other positions in the cap are not favorable for Mo incorporation. The distance between Fe_e and Fe_i and between two Fe_i is 3.13 Å. BVS indicates W/Mo in +6, Zn in +2, and Fe at internal as well as external positions in +3 oxidation state (Table S23).

ESI-mass spectrum of **6** in shows the envelope of peaks at m/z 1587.17 (z=-3) due to the presence of $H_9Fe_4(Zn_2W_{18}O_{68})$ while ESI-mass spectrum of analog mixed addenda POMs **6-M** (Figure S55, Table S24) shows the multiple envelopes of peaks attributed to varying ratios of Mo to W towards low m/z values. The **6-M** shows the envelopes of peaks in the range of *m/z* 1500-1630 for $H_9[\{Fe_4(H_2O)_2(ZnMo_xW_{9-x})_2\}^{3-}]$, and *m/z* 1150-1200 for $H_8[\{Fe_4(H_2O)_2(ZnMo_xW_{9-x})\}^{4-}]$. The most abundant anion in $[\{Fe_4(H_2O)_2(ZnMo_xW_{9-x})_2\}^{12-}]$ has the composition without Mo addenda in the formula, i.e., formation of **6** dominates in the synthesis of **6-M**. However, the highest Mo/W ratio in **6-M** was found to be 2/16 with a constant charge of the cluster, i.e., -12. Further, pH plays a crucial role in tuning the amount of Mo addenda incorporation. Hence, to understand the factor controlling the Mo/W ratio in the **6-M**, a systematic synthetic study was performed at different pH. It was

observed **6-M** forms only at a particular pH, and lowering the pH does not incorporate more Mo addenda however, it results in the formation of Keggin POMs as observed in ESI-MS.

The FT-IR spectra of **6** show the characteristics peaks at 927 cm^{-1} ($W=O_{term}$), 841, 680 cm^{-1} (W-O-W) cm^{-1} while **6-M** show the charcateristics peaks at 920 cm^{-1} ($M=O_{term}$), 836, 680 cm^{-1} (M-O-M) cm^{-1} (Figure S57a) with slight shifting due to Mo incorporation in the framework. **6-M** exhibits broad absorption bands in the UV-vis region due to ligand-to-metal charge transfer (LMCT) (O2p → W5d), while very weak absorption in the visible region is due to the forbidden d-d transition. Moreover, a significant absorption peak at 484 was observed due to metal-to-POM framework charge transfer (MMCT) in **6-M** (Figure S57b). DRS indicates two different band gaps in **6-M** at 2.43 eV and 2.30 eV due to LMCT and MMCT (Figure S57b/S57c). The phase purity of **6-M** was obtained from PXRD. The experimental PXRD patterns are consistent with their simulated pattern, indicating the phase purity of all compounds (Figure S56a).

The SC-XRD structure of **7** (green colored rhombic crystals) and **8** (light yellow rhombic crystals) shows the formation of 1-D structure connected by 3d transition metals (Figure S42c/S50-S54). The 3D SC-XRD structure of **7** shows that the trilacunary Keggin moiety contains a tetrahedrally bound Co atom in the center as a templating agent to triads of addenda W atoms. The tetrasubstituted sandwich core consists of Fe:W (80:20) at internal $\{TM_i\}$ position and Co as external atoms $\{TM_e\}$ and Fe atoms as a countercation coordinates to POMs structures to form 1-D network structure (Figure S50-S52). BVS indicates W in +6, Co in +2, and Fe at internal in +3 while at countercation position in +2 oxidation state (Table S23). The 3D SC-XRD structure of **8** shows that the trilacunary Keggin moiety contains a tetrahedrally bound Zn atom in the center as a templating agent to triads of addenda W atoms. The tetrasubstituted sandwich core consists of Zn:W (50:50) at internal $\{TM_i\}$ position and Zn:Mn (50:50) as external atoms $\{TM_e\}$, and Mn as well as Zn atoms act as a countercation, thus coordinating POMs structures to form 1-D structure (Figure S53-S54). BVS indicates W in +6, Zn and Mn in +2 oxidation state (Table S24). The experimental PXRD patterns are consistent with their simulated pattern, indicating the phase purity of **7** and **8** (Figure S56c/S56d).

DFT study indicates the decrease in the band gap when we go from **6** to **6-M** due to incorporation of Mo as an addenda, similar to **2**/**2-M**. Apart from this, the overall charge of these POMs significantly affects the properties of these POMs, e.g. in case of **6** (Figure S60b) and **6-M** (Figure S60c), when we go from charge -12 to -16 within the same POM, the elongation of TM-O(H_2O) bond take place due to increase in overall charge density of POM thus making it susceptible to substitution which was observed in **6-M** experimentally also. Thermal stability was determined by TGA analysis from 30 to 600 °C for **6**/**6-M**/**7**/**8** (Figure S61-S62). The TGA curve shows that frameworks **6**/**6-M** are highly stable up to 480 °C (Figure S61). The first weight loss observed below 200 °C was attributed to the release of water of crystallization. Stepwise weight loss indicates lattice and hydrated water molecules in the range of 30-180 °C. Slight weight loss at 480 °C is attributed to the release of coordinated transition metal oxides between two sandwich POMs, thus indicating that these 1-D frameworks are stable up to 480 °C. However, in the case of **8**, weight loss at 300 °C indicates less stability of 1-D framework, which might be due to the presence of W at the sandwich position as well as transition metals between sandwich POMs.

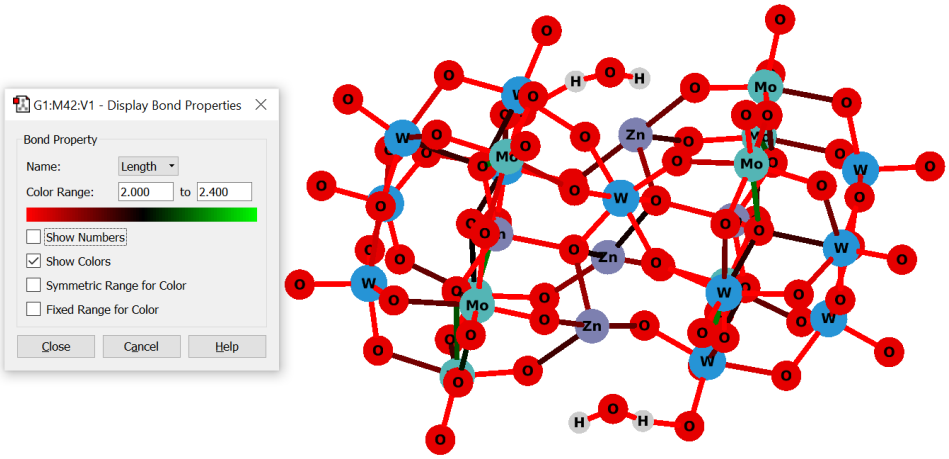

Figure S63. DFT optimized auxiliary structure of sandwich POMs with the general formula $[Zn_3W(H_2O)_2(ZnMo_xW_{9-x}O_{34})_2]^{12-}$ showing bond length in the range of 2.0 to 2.4 Å.

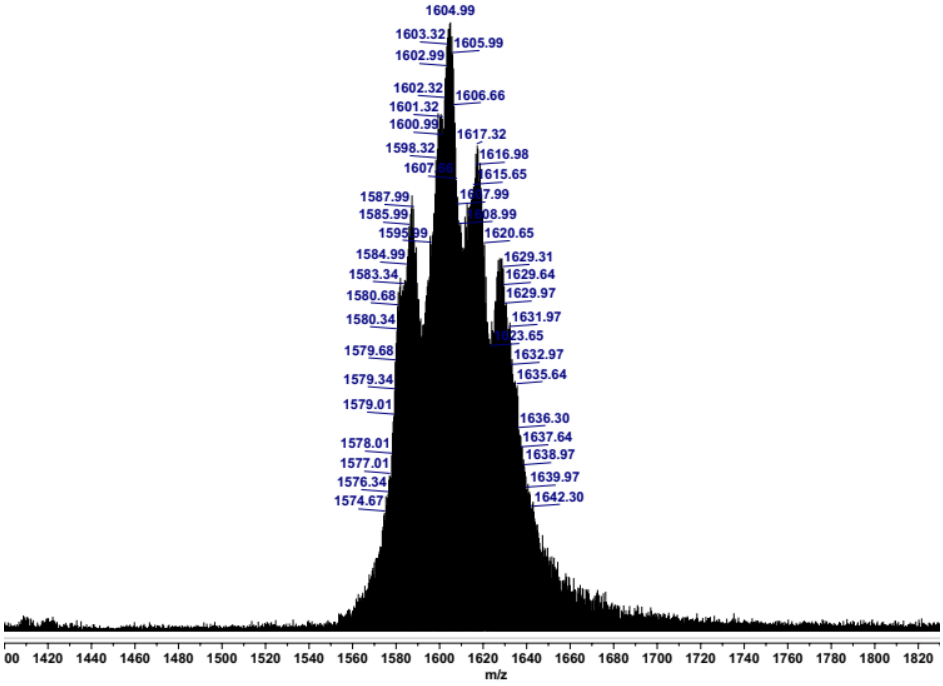

Figure S64. ESI-MS spectra of crystals obtained after side substitution of **2**, showing multiple peaks in the range of m/z 1400-1820 (z = –3).

Table S25. Assignment of ESI-mass peaks **2** after substitution

Charge	m/z (obs.)	m/z (calc.)	Mol. Wt.	Assigned probable formula
-3	1587.99	1587.13	4761.40	$H_{11}MnFe_3(Zn_2W_{18}O_{68})$
-3	1604.99	1605.12	4815.35	$H_9Na_2ZnFe_3(Zn_2W_{18}O_{68})$
-3	1617.32	1616.77	4850.32	$H_7Na_4Fe_4(Zn_2W_{18}O_{68})$
-3	1629.31	1629.13	4887.40	$H_{11}Mn_3W(Zn_2W_{18}O_{68})$

Characterizations of 2a/2b/2c/2d for TM_e = Mn/Co/Ni/Cu and 2c-M

Table S26. Crystal data, data collection, and refinement parameters for **2c, 2c-M** and **2d**

	2c	**2c-M**	**2d**
CCDC number	**2330244**	**2330254**	**2330258**
empirical formula	$FeNa_{13.5}Ni_3O_{109}W_{18}Zn_2$	$Fe_2Mo_{0.4}Na_{12}Ni_2O_{108}W_{17.6}Zn_2$	$Cu_2FeNa_{12}O_{109}W_{18}Zn_3$
formula weight	5726.15	5637.88	5708.22
temp (K)	273.15	273.15	273.15
crystal system	triclinic	monoclinic	Monoclinic
space group	$P\bar{1}$	$P2_1/n$	$P2_1/n$
unit cell dimension			
a (Å)	12.3582(8)	13.1561(7)	13.106(3)
b (Å)	13.7895(9)	17.7357(10)	17.783(3)
c (Å)	14.8800(10)	21.1008 (12)	21.154(5)
α (deg)	99.217(2)	90	90
β (deg)	104.045(2)	93.482(2)	93.607(10)
γ (deg)	102.158(2)	90	90
V (Å^3)	2344.3(3)	4914.4(5)	4921(2)
Z	1	2	2
ρ (calculated) (g/cm^3)	4.056	3.810	3.853
μ/mm^{-1}	23.411	21.866	22.402
F (000)	2522.0	4966.0	5020.0
crystal size (mm^3)	0.33 × 0.28 × 0.12	0.24 × 0.17 × 0.15	0.37 × 0.26 × 0.22
2Θ range for data collection/°	4.038 to 52.918	3.864 to 52.842	4.406 to 50.052
index ranges	-15 ≤ h ≤ 15, -17 ≤ k ≤ 17, -18 ≤ l ≤ 18	-16 ≤ h ≤ 16, -22 ≤ k ≤ 22, -26 ≤ l ≤ 26	-15 ≤ h ≤ 15, -21 ≤ k ≤ 21, -25 ≤ l ≤ 25
no. of reflection collected /unique	40294/9630	66489/10060	64566/8618
GOF on F^2	1.023	1.049	1.084
R(int)	0.070	0.064	
final *R* indices ($I > 2\sigma(I)$)	R_1 = 0.0354, wR_2 = 0.0776	R_1 = 0.0364, wR_2 = 0.0890	R_1 = 0.0307, wR_2 = 0.0.0810
R indices (all data)	R_1 = 0.0489, wR_2 = 0.0842	R_1 = 0.0452, wR_2 = 0.0941	R_1 = 0.0326, wR_2 = 0.0823
data/restraints/param	9630/0/713	10060/0/668	8618/0/668
Largest diff. peak/hole / e Å^{-3}	1.99/-1.68	3.33/-2.25	2.52/-2.38

Table S27. Bond valence parameter of selected atoms calculated from the SC-XRD structure of **2c**/**2d** and **2c-M**			
POMs	Transition metal	Bond valence sum value	Oxidation state
2c-M	Mo	6.15	+6
	W	6.07	+6
	Zn	2.46	+2
	Fe	3.09	+3
	Ni	2.06	+2
2c	W	6.05	+6
	Zn1	2.31	+2
	Fe1	3.09	+3
	Ni2	2.06	+2
2d	W	6.04	+6
	Zn	2.41	+2
	Fe2	3.01	+3
	Cu1	2.05	+2

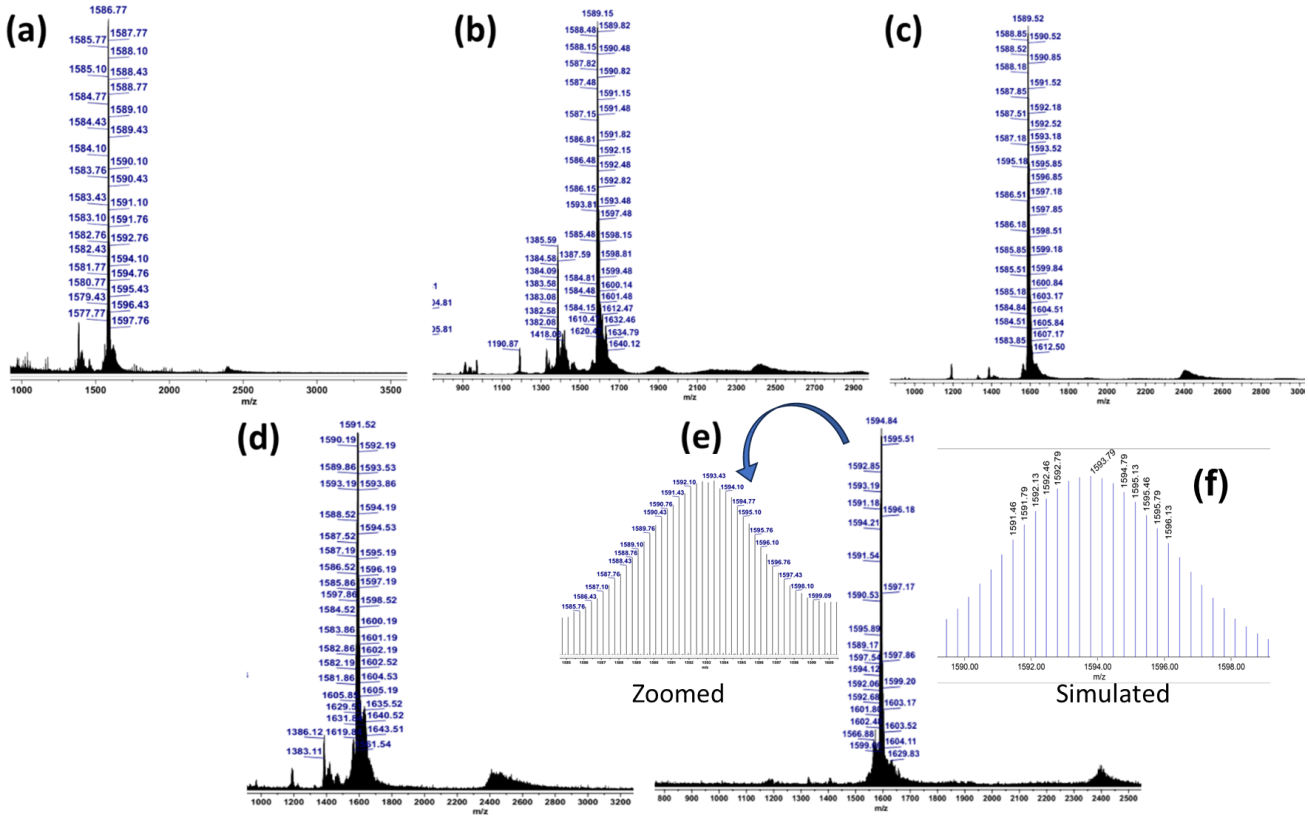

Figure S65. (a-e) Full ESI-MS spectra of a series of POMs (z = –3) for **2a/2b/2c/2d/2**. (f) Zoomed part of the highest intensity peak of **2** (m/z= 1593.43 with z= –3) and its corresponding simulated ESI-MS spectra.

Table S28. Assignment of ESI-mass peaks of Zn-Fe_2M_2 POMs where M = Mn/Co/Ni/Cu/Zn

Charge	m/z (obs.)	m/z (calc.)	Mol. Wt.	Assigned probable formula
-3	1586.81	1586.79	4760.39	$H_{11}Mn_2Fe_2(ZnW_9O_{34})_2$
-3	1589.48	1589.46	4768.38	$H_{11}Co_2Fe_2(ZnW_9O_{34})_2$
-3	1589.52	1589.12	4767.38	$H_{11}Ni_2Fe_2(ZnW_9O_{34})_2$
-3	1591.52	1592.46	4777.39	$H_{11}Cu_2Fe_2(ZnW_9O_{34})_2$
-3	1593.43	1593.79	4781.37	$H_{11}Zn_2Fe_2(ZnW_9O_{34})_2$

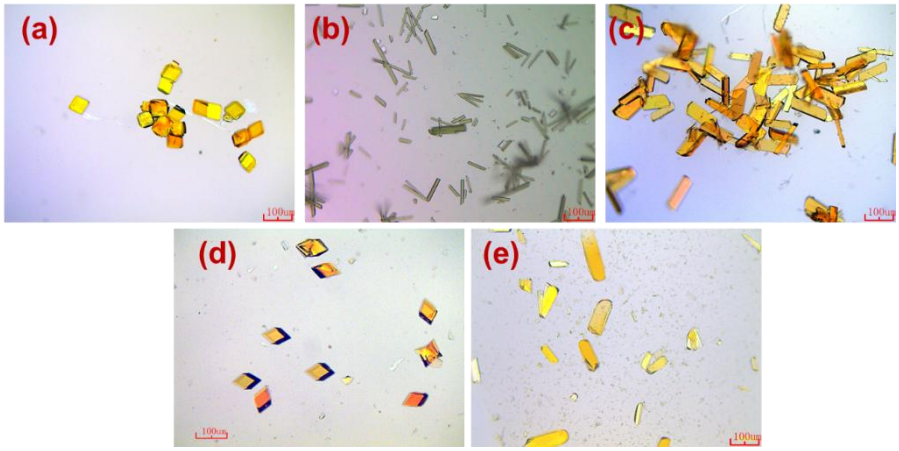

Figure S66. Optical images of sandwich POMs; (a) **2a** (b) **2b** (c) **2c** (d) **2d** (e) **2.**

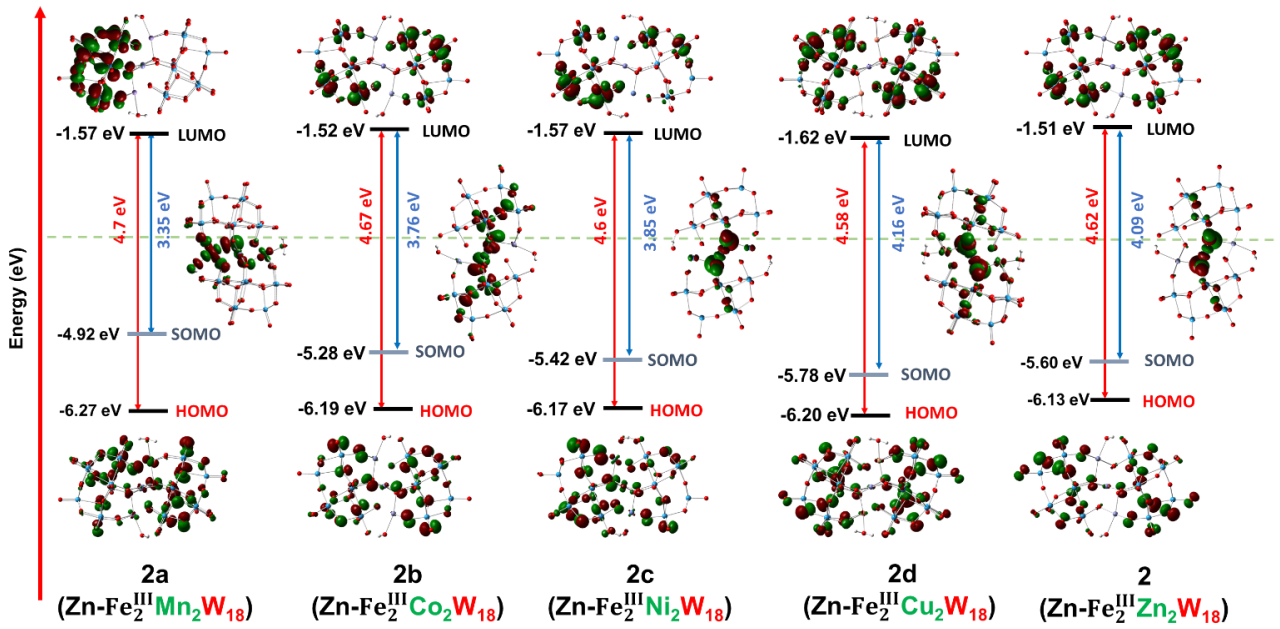

Figure S67. Frontier molecular orbitals of tetrasubstituted sandwich POMs showing band gaps as well as electron density on addenda atoms in **2a/2b/2c/2d/2**.

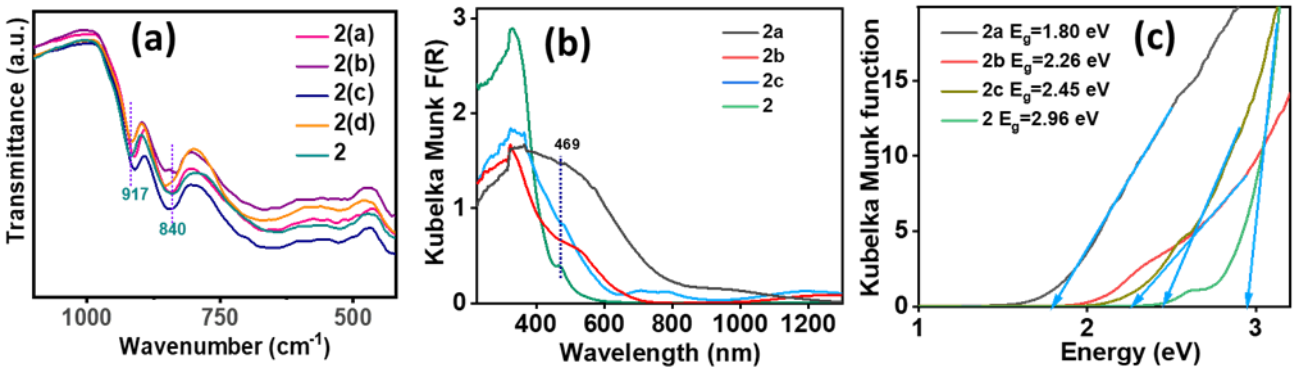

Figure S68. (a) FT-IR spectra of **2a/2b/2c/2d/2** (b) solid-state UV-vis spectra and corresponding (c) optical band-gap shifting derived from the Kubelka-Munk equation in **2a/2b/2c/2.**

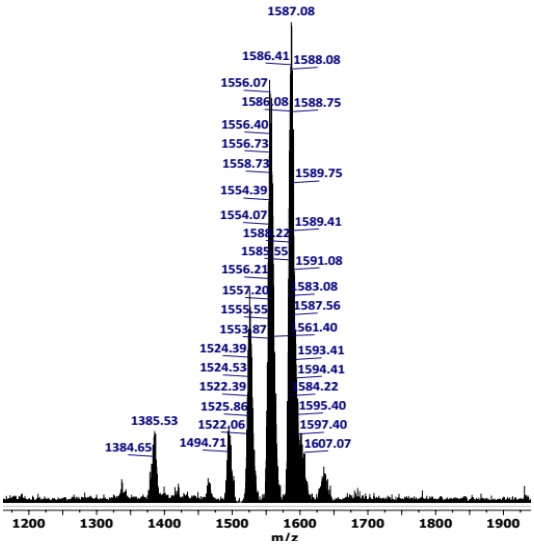

Figure S69. ESI-MS spectra of **2c-M** in the range of m/z 1200-1900 (z = –3).

Table S29. Assignment of ESI-mass peaks of **2c-M**

Charge	m/z (obs.)	m/z (calc.)	Mol. Wt.	Assigned probable formula
-3	1587.08	1587.13	4761.39	$H_{11}Ni_3Fe(ZnFeW_{18}O_{68})$
-3	1556.07	1556.45	4669.35	$H_{10}Ni_2Fe_2(ZnFeMoW_{17}O_{68})$
-3	1525.72	1525.76	4577.30	$H_9NiFe_3(ZnFeMo_2W_{16}O_{68})$
-3	1495.72	1496.75	4490.26	$H_9NiFe_3(ZnFeMo_3W_{15}O_{68})$

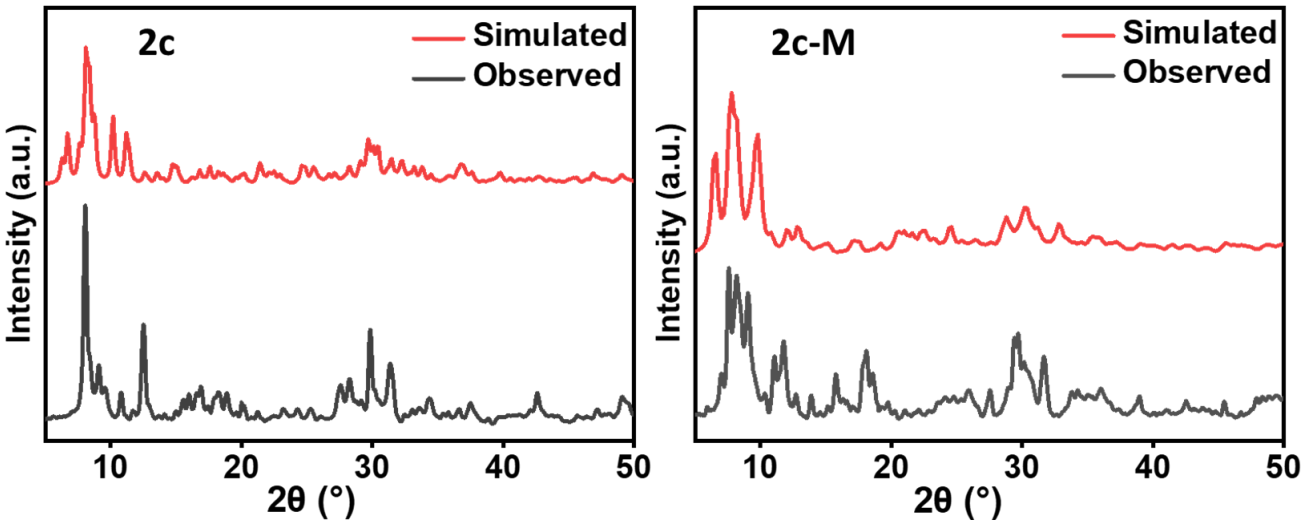

Figure S70. Observed PXRD pattern and comparison with the simulated data obtained from single crystal XRD for **2c** and **2c-M.**

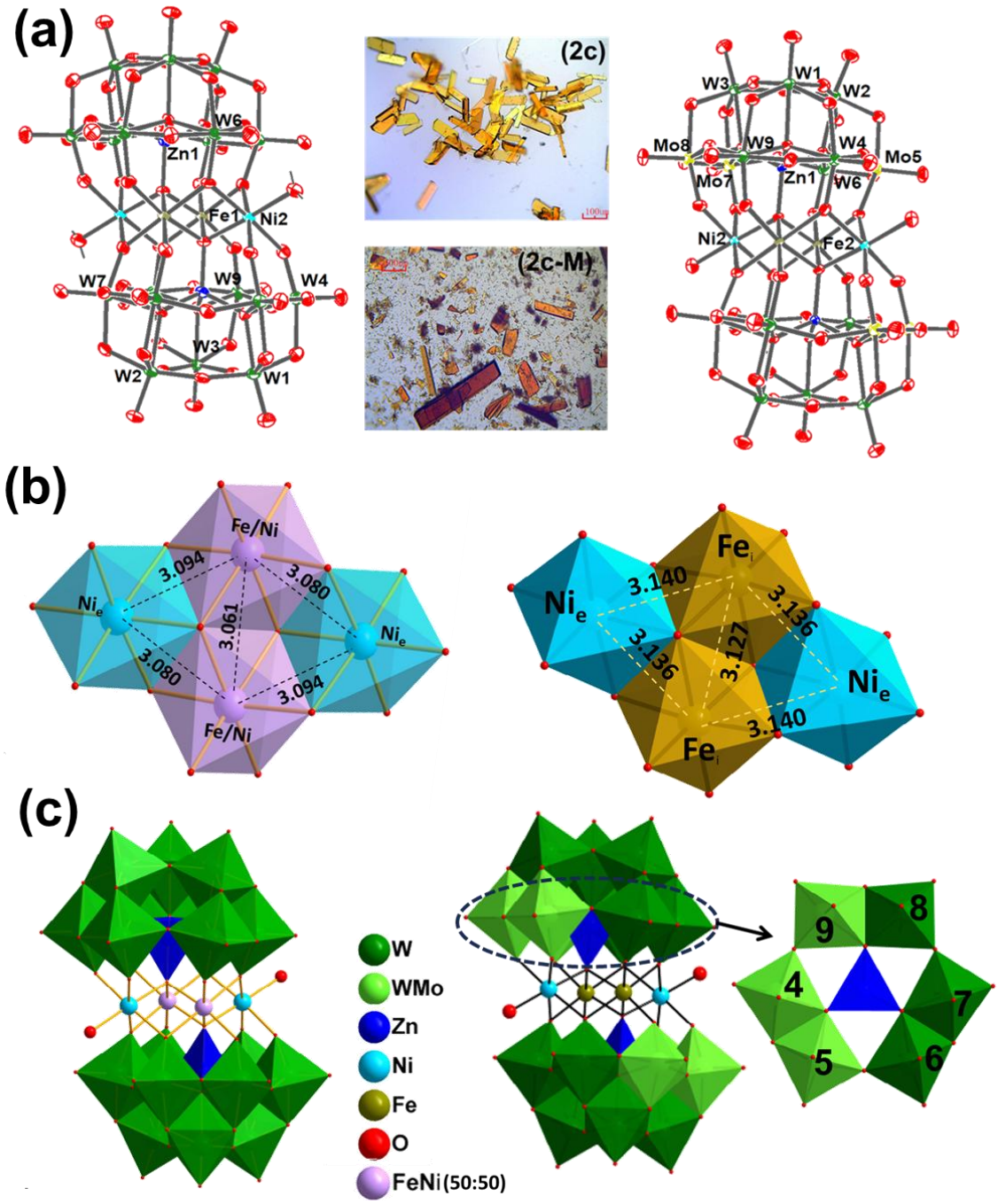

Figure S71. (a) ORTEP drawing (with 60% ellipsoid probability) and Optical images of sandwich POMs; **2c** (left) and **2c-M** (right); (b) Cubane core showing the interatomic distance between transition metals in **2c** (left) and **2c-M** (right); (c) combined polyhedral/ball and stick representation of the single-crystal X-ray structure of polyoxometalate **2c** (left) and **2c-M** (right), belt 2 depicting different ratios of molybdenum to tungsten in **2c-M**;**.** Countercations and hydrogen atoms are omitted for clarity.

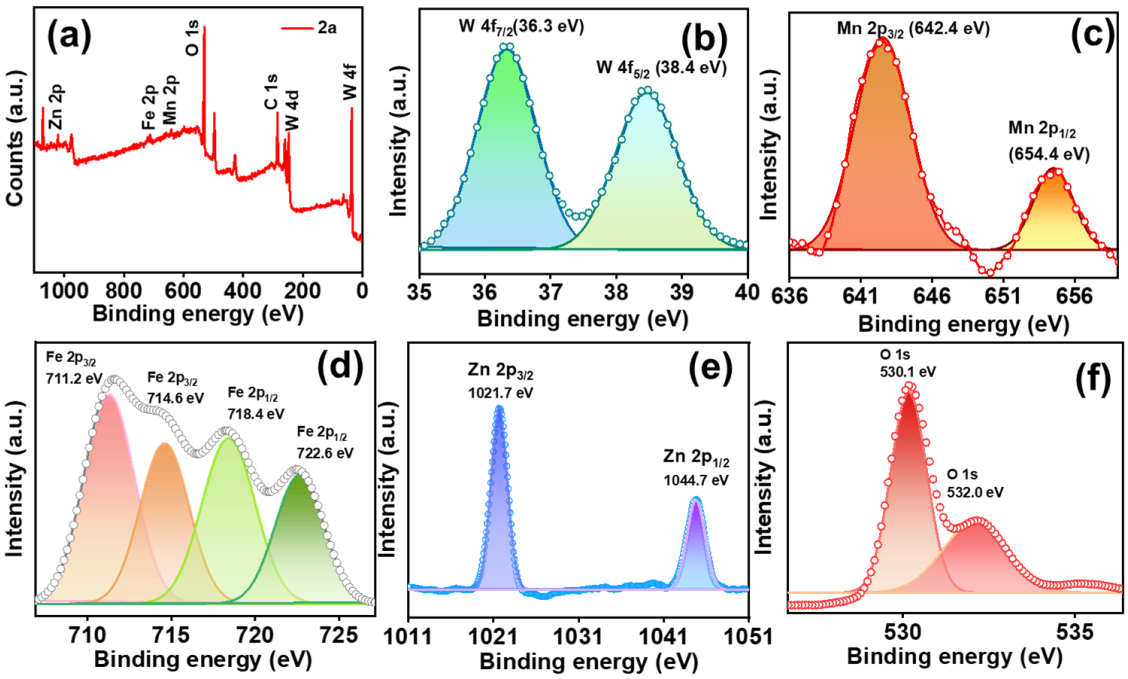

Figure S72. XP spectra of **2a** (a) Survey spectra, (b) W $4f_{7/2}$ and $4f_{5/2}$, (c) Mn $2p_{3/2}$ and $2p_{1/2}$, (d) Fe $2p_{3/2}$ and $2p_{1/2}$, (e) Zn $2p_{3/2}$ and $2p_{1/2}$, and (f) O 1s.

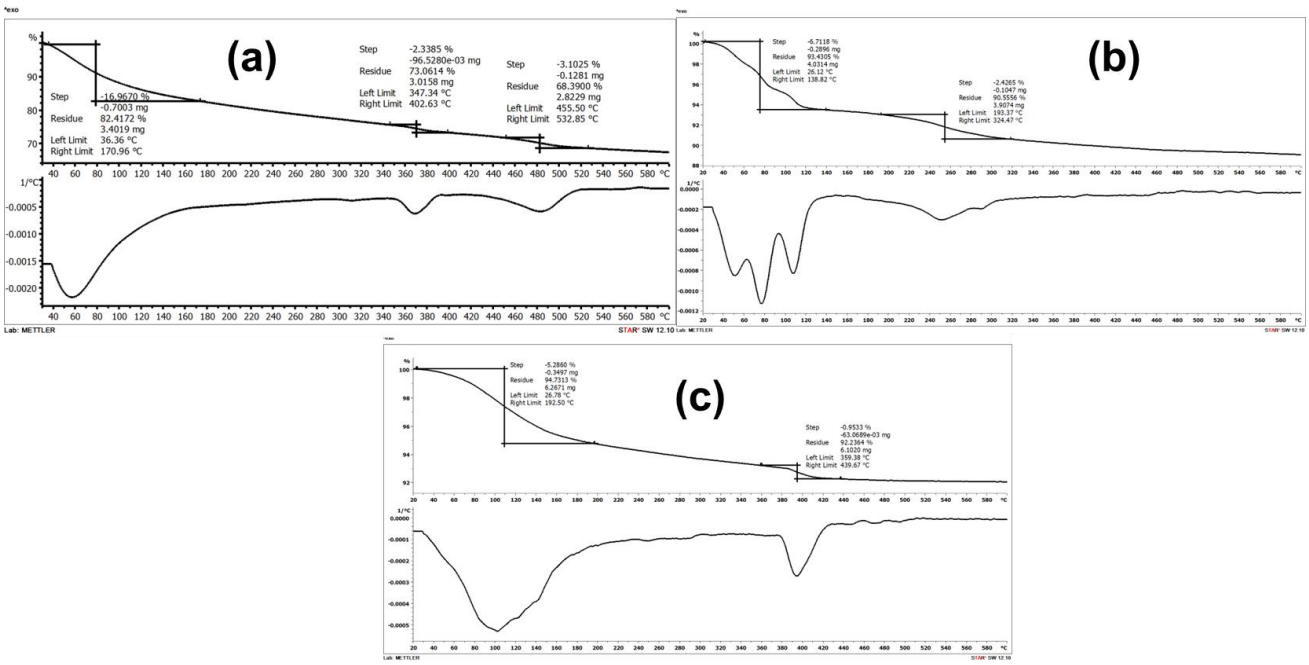

Figure S73. TGA curve along with corresponding first derivative of (a) **2c**, (b) **2d**, (c) **2c-M**.

Characterizations analysis of **2a/2b/2c/2d and 2c-M**

Compounds **2a/2b/2c/2d** and **2c-M** were characterized using SC-XRD, FT-IR, ESI-MS, XPS, and UV-visible spectroscopy (Figure S65-S73). The framework structure of **2c**/**2d**/**2c-M** was confirmed by SC-XRD (**CCDC 2330244, 2330254 and 2330258)**. **2c** crystallizes in a triclinic lattice with $P\bar{1}$ space group while its analog mixed addenda **2c-M** and **2d** crystallizes in a monoclinic lattice with a $P2_1/n$ space group (Table S26). The 3D SC-XRD structure of **2c/2d** and **2c-M** shows that the tri lacunary Keggin moiety contains a tetrahedrally bound zinc atom in the center as a templating agent to triads of addenda W/Mo atoms. The tetrasubstituted sandwich core consists of Fe at the internal $\{TM_i\}$ position and Ni as external atoms $\{TM_e\}$ in **2c**/**2c-M**, while in **2d**, Cu is at the external transition position (Figure S71a). The optical image shows that the substitution of external transition metals in **2** completely changes the size and shape of the crystals (Figure S66).

The ESI-MS spectrum of parent **2** shows one envelope of peaks at a *m*/*z* of 1593.43 assigned for a $\{H_{11}[Zn_2Fe_2(ZnW_9O_{34})_2]^{3-}$ cluster anion. Transition metal substitutes analog of **2** shows the envelope of peaks at m/z 1591.52 for $\{H_{11}[Cu_2Fe_2(ZnW_9O_{34})_2]^{3-}$, 1589.52 for $\{H_{11}[Ni_2Fe_2(ZnW_9O_{34})_2]^{3-}$, 1589.46 for $\{H_{11}[Co_2Fe_2(ZnW_9O_{34})_2]^{3-}$ and 1586.91 for $\{H_{11}[Mn_2Fe_2(ZnW_9O_{34})_2]^{3-}$ thus indicating that these POMs cluster anions have high hydrolytic stability in the solution (Figure S65, Table S28). The **2c-M** shows the envelopes of peaks (Figure S69, Table S29) in the range of *m*/*z* 1490-1630 for $H_{11}[\{Ni_2Fe_2(H_2O)_2(ZnMo_xW_{9-x})_2\}^{3-}]$. The most abundant anion in **2c-M** has the composition without Mo addenda in the formula, i.e., formation of **2c** dominates in the synthesis of **2c-M**. However, the highest Mo/W ratio in **2c-M** was found to be 3:15 with a constant -14 charge of the cluster. From the comparison of **2c-M** with the reference (Figure S1) structure, a small amount of Mo incorporation is favorable at 4/7 positions of the belt, while other positions in the belt, as well as in the cap are less favorable for the incorporation of Mo addenda in the tetrasubstituted framework (Figure S71c). The experimental PXRD patterns are consistent with their simulated pattern (Figure S70a-b), indicating the phase purity of **2c** and **2c-M**.

The distance between Ni atoms at the external and Ni/Fe (50:50) at the internal positions is 3.08-3.09 Å, however, the distance between Ni/Fe atoms in the internal positions is 3.06 Å in **2c.** The distance between Ni atoms at the external and Fe at the internal positions is 3.11 Å, and the distance between internal Fe atoms is 3.11 Å in **2c-M** (Figure S71b). The FT-IR spectra of all these POMs show the characteristics peaks in the region 650-920 cm^{-1} e.g. the FT-IR spectra of **2c** show characteristics peaks at 910 cm^{-1} ($W{=}O_{term}$), 845, 679 cm^{-1} (W-O-W) cm^{-1} (Figure S68a) while the FT-IR spectra of **2c-M** show characteristics peaks similar to **2c** in the region 650-920 cm^{-1} with slight shifting due to Mo incorporation in the framework. BVS calculation indicates that all addenda atoms are in their highest oxidation state (+6) and Fe, Ni, Cu, and Zn in +3, +2, +2, and +2 oxidation states, respectively (Table S27). Apart from the BVS, the oxidation states of all of the atoms in **2c-M** were determined from XPS analysis. The XP spectra of **2c-M** revealed the presence of W, Mo, Fe, Ni, Zn, and oxygen (Figure S72). The two peaks at 713.4 and 719.6 eV in **2c-M** can be attributed to the presence of Fe in a +3 oxidation state. The W 4f doublet appears between 36.3 and 38.4 eV, corresponding to W $4f_{7/2}$ and $4f_{5/2}$ in +6 oxidation state.

In UV-visible spectroscopy, all these POMs show a strong and broad absorption band between 280-350 nm, as expected, due to LMCT ($O_{2p} \rightarrow W_{5d}$) transitions for ZnW_9O_{34} units. Apart from this, all these POMs show a

feeble peak due to MPCT around 469 nm. The absorbance spectra as well as the band gap of these TMSP are highly influenced by the substituted transition metals and show shifts in the absorption band, e.g., the LMCT band shifts to a lower wavelength for **2a**/**2b**/**2c**/**2d** than the parent **2**. Similarly, the HOMO-LUMO gap increases with the increase in the atomic number of transition metals except for 3d. The trend of the band gap is **2c** > **2b** > **2a** > **2** (Figure S68c). This increase in band gap was further supported by the DFT study, which indicates that the band gap (highest SOMO to LUMO) increases when we go from **2a** to **2d** (Figure S67). Interestingly, the LUMO of all these POMs lies at the internal transition atom, i.e., Fe(3+). Thermal stability was determined by TGA analysis from 25 to 600 °C (Figure S73). The TGA curve of **2c/2d/2c-M** shows high thermal stability up to 600 °C. The first weight loss was observed in the range of 30-200 °C, which is attributed to the release of water of crystallization and water of hydration. Further, slight weight loss (<2%) was observed in the range of 240-450 °C, which is attributed to the release of water molecules coordinated to the counter cations outside the POM framework.

Characterizations of 3a/3/3b/3c/3d for TM_e = Mn/Co/Ni/Cu/Zn and 3b-M

Table S30. Crystal data, data collection, and refinement parameters for **3c** and **3b-M**

	3c	**3b-M**
CCDC number	**2330250**	**2330249**
empirical formula	$Co_2Cu_3FeNa_{11}O_{108}W_{18}$	$H_{8.4}CoFe_2Mo_{3.2}Na_{10}Ni_3O_{107.2}W_{14.8}$
formula weight	5654.52	5328.31
temp (K)	273.15	293.15
crystal system	Monoclinic	monoclinic
space group	$P2_1/n$	$P2_1/n$
unit cell dimension		
a (Å)	13.203(7)	13.1444(8)
b (Å)	17.793(9)	17.7309(10)
c (Å)	21.113(11)	20.9862(13)
α (deg)	90	90
β (deg)	93.335(18)	93.532(2)
γ (deg)	90	90
V (Å^3)	4951(4)	4881.8(5)
Z	2	2
ρ (calculated) (g/cm^3)	3.793	3.625
μ/mm^{-1}	22.080	18.937
F (000)	4968.0	4737.0
crystal size (mm^3)	0.44 × 0.25 × 0.18	0.35 × 0.29 × 0.29
Radiation	MoKα (λ = 0.71073)	MoKα (λ = 0.71073)
2Θ range for data /°	3.86 to 51.35	3.86 to 52.92
index ranges	-16 ≤ h ≤ 16, -21 ≤ k ≤ 21, -25 ≤ l ≤ 25	-16 ≤ h ≤ 16, -22 ≤ k ≤ 22, -26 ≤ l ≤ 26
no. of reflection collected /unique	45120/9378	58526/10053
GOF on F^2	1.077	1.039
R(int)	0.051	0.054
final R indices ($I > 2\sigma(I)$)	R_1 = 0.0332, wR_2 = 0.0740	R_1 = 0.0346, wR_2 = 0.0877
R indices (all data)	R_1 = 0.0403, wR_2 = 0.0787	R_1 = 0.0442, wR_2 = 0.0935
data/restraints/param	9378/0/659	10053/0/637
Largest diff. peak/hole / e Å^{-3}	2.02/-1.76	2.17/-1.21

Table S31. Bond valence parameter calculated from the SC-XRD structure of sandwich POMs in **3c** and **3b-M**			
POMs	Transition metal	Bond valence sum value	Oxidation state
3b-M	W	6.07	+6
	Mo	6.79	+6
	Ni1	3.19	+3
	Ni2	2.03	+2
	Fe1	3.12	+3
	Co2	2.61	+2
3c	W	6.07	+6
	Fe1	3.07	+3
	Cu1	3.26	+3
	Cu2	2.07	+2
	Co2	2.32	+2

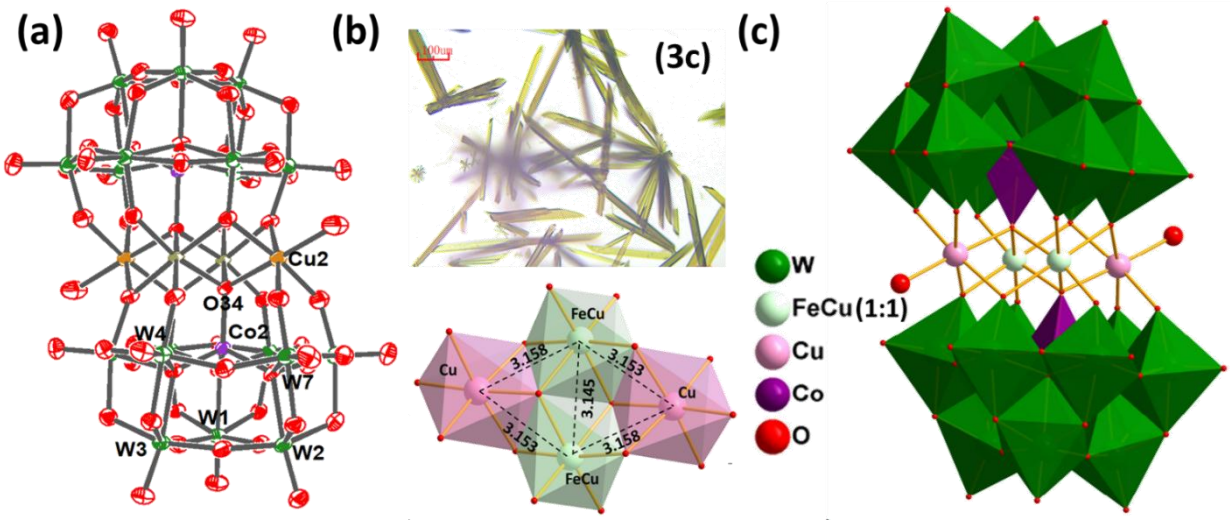

Figure S74. (a) ORTEP drawing (with 60% ellipsoid probability) (b) Optical images and Cubane core showing the interatomic distance between transition metals in **3c** (c) combined polyhedral/ball and stick representation of the single-crystal X-ray structure of polyoxometalate **3c.** Countercations and hydrogen atoms are omitted for clarity.

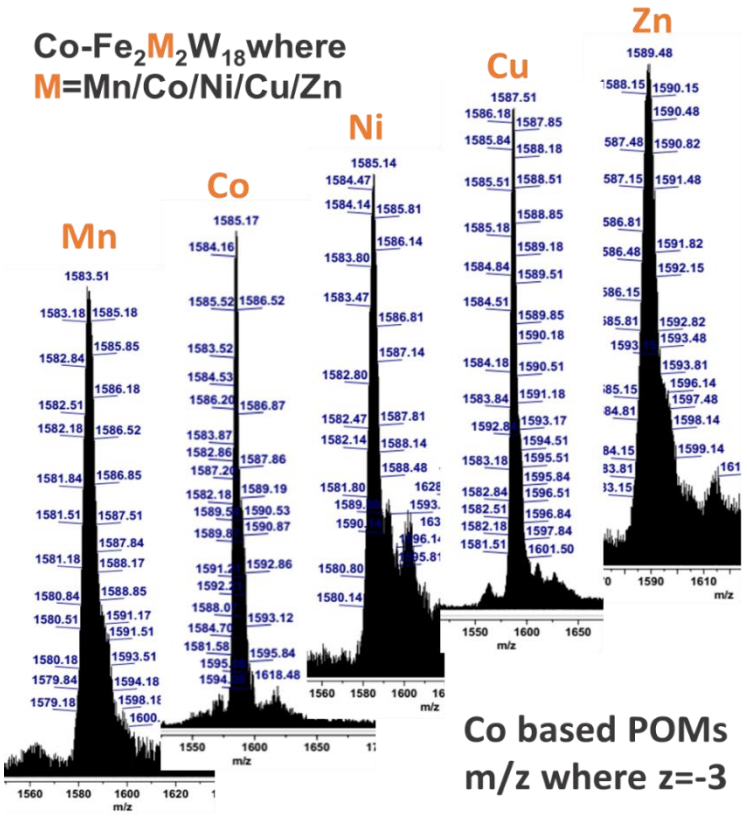

Figure S75. ESI-MS spectra of **3a/3/3b/3c/3d** in the range of m/z 1500-1650 (z = –3).

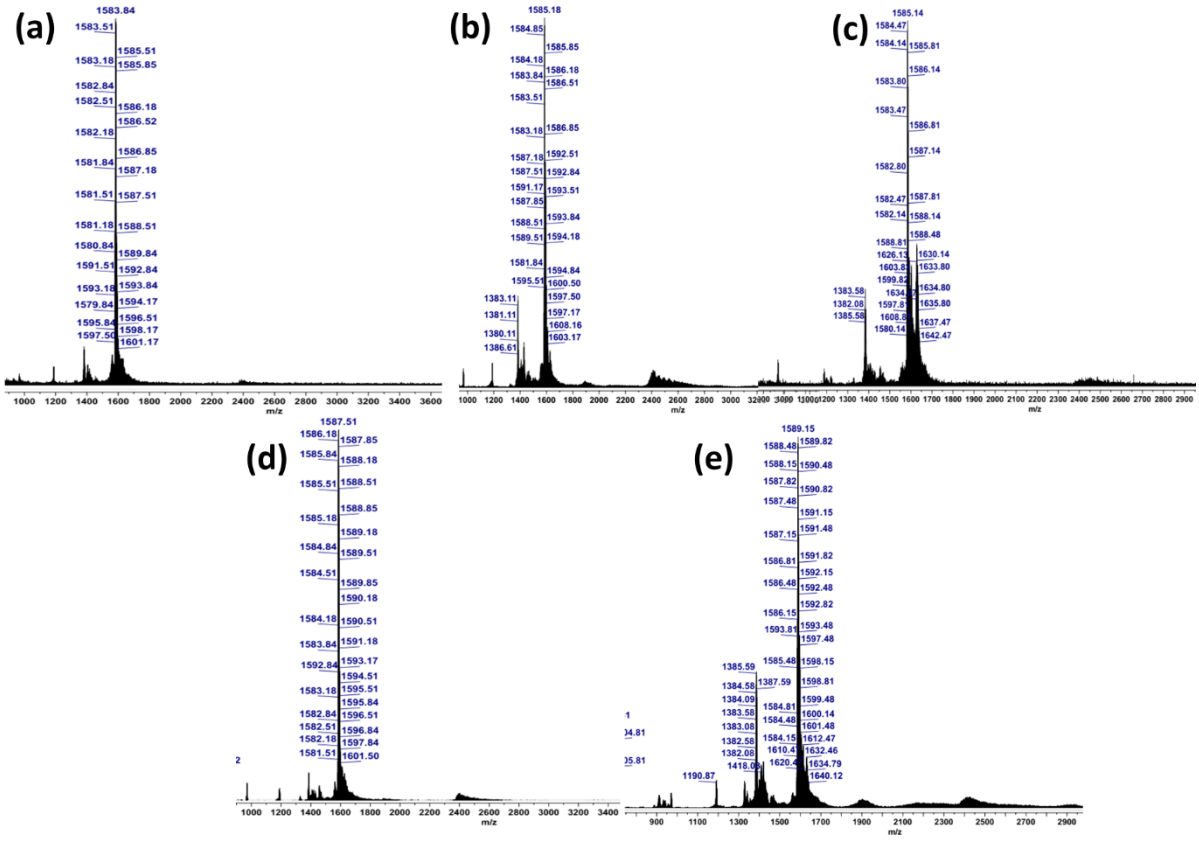

Figure S76. ESI-MS spectra of **3a/3/3b/3c/3d** in the full range of m/z 1000-3000 (z = –3).

Table S32. Assignment of ESI-mass peaks of **3a/3/3b/3c/3d**

Charge	m/z (obs.)	m/z (calc.)	Mol. Wt.	Assigned probable formula
-3	1583.51	1582.56	4747.40	$H_{11}Mn_2Fe_2(CoW_9O_{34})_2$
-3	1585.17	1585.13	4755.39	$H_{11}Co_2Fe_2(CoW_9O_{34})_2$
-3	1585.14	1585.13	4755.39	$H_{11}Ni_2Fe_2(CoW_9O_{34})_2$
-3	1587.51	1588.13	4764.40	$H_{11}Cu_2Fe_2(CoW_9O_{34})_2$
-3	1589.48	1589.46	4768.38	$H_{11}Zn_2Fe_2(CoW_9O_{34})_2$

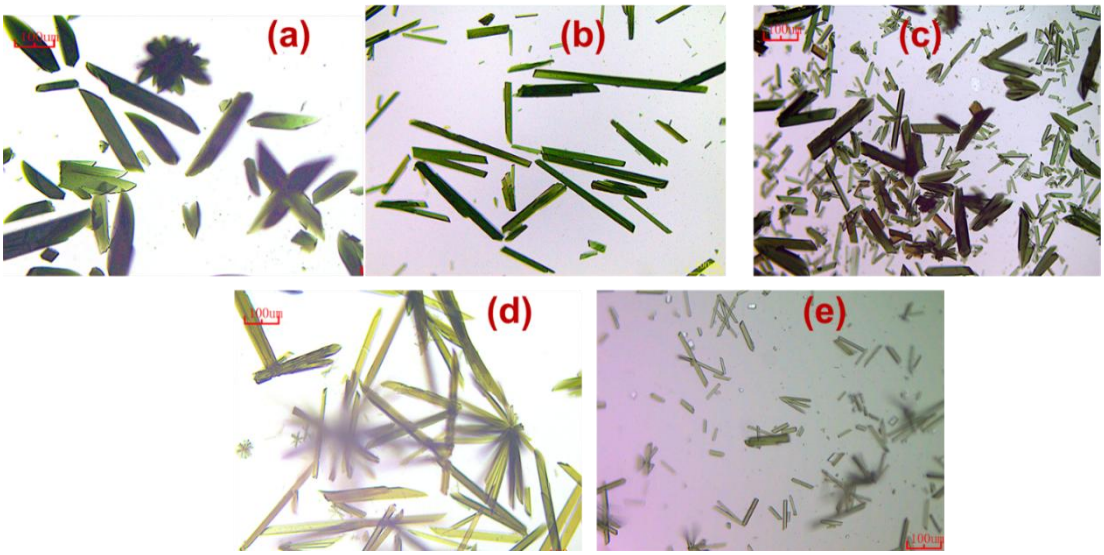

Figure S77. Optical images of sandwich POMs; (a) **3a** (b) **3** (c) **3b** (d) **3c** (e) **3d**

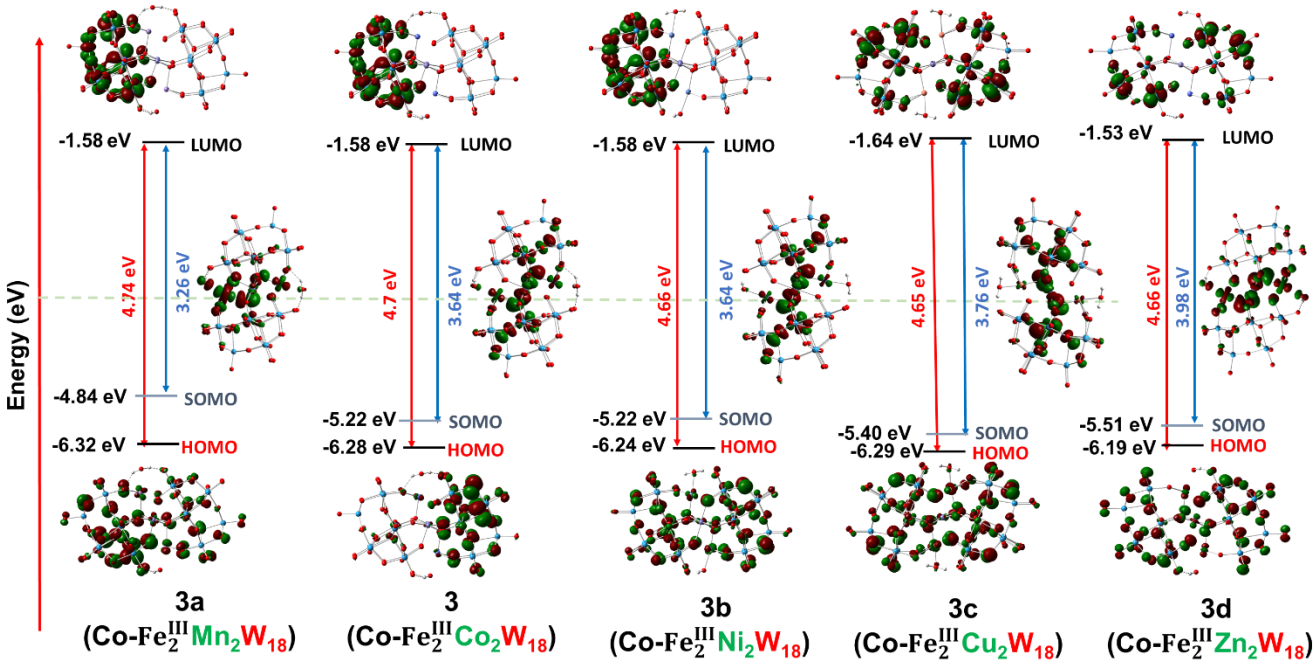

Figure S78. FMOs of tetrasubstituted sandwich POMs showing band gaps as well as electron density on addenda atoms in **3a/3/3b/3c/3d**.

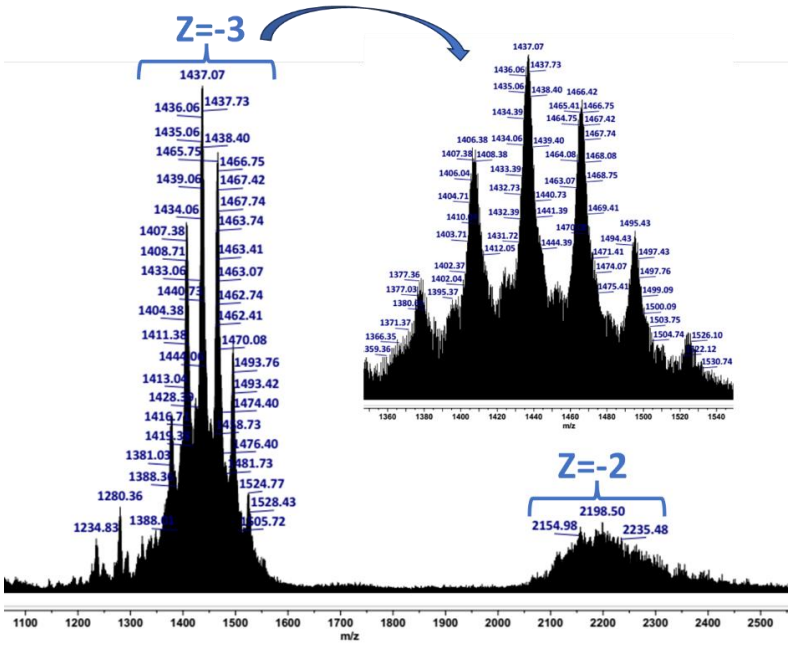

Figure S79. ESI-MS spectra of **3b-M** in the range of m/z 1100-2500 (z = –3).

Table S33. Assignment of ESI-mass peaks of 3b-M

Charge	m/z (obs.)	m/z (calc.)	Mol. Wt.	Assigned probable formula
-3	1495.43	1495.75	4487.27	$H_{10}Ni_2Fe_2(FeCoMo_3W_{15}O_{68})$
-3	1466.42	1466.41	4399.23	$H_{10}Ni_2Fe_2(FeCoMo_4W_{14}O_{68})$
-3	1437.07	1437.06	4311.19	$H_{10}Ni_2Fe_2(FeCoMo_5W_{13}O_{68})$
-3	1406.38	1406.38	4219.15	$H_{10}Ni_2Fe_2(Fe_2Mo_6W_{12}O_{68})$

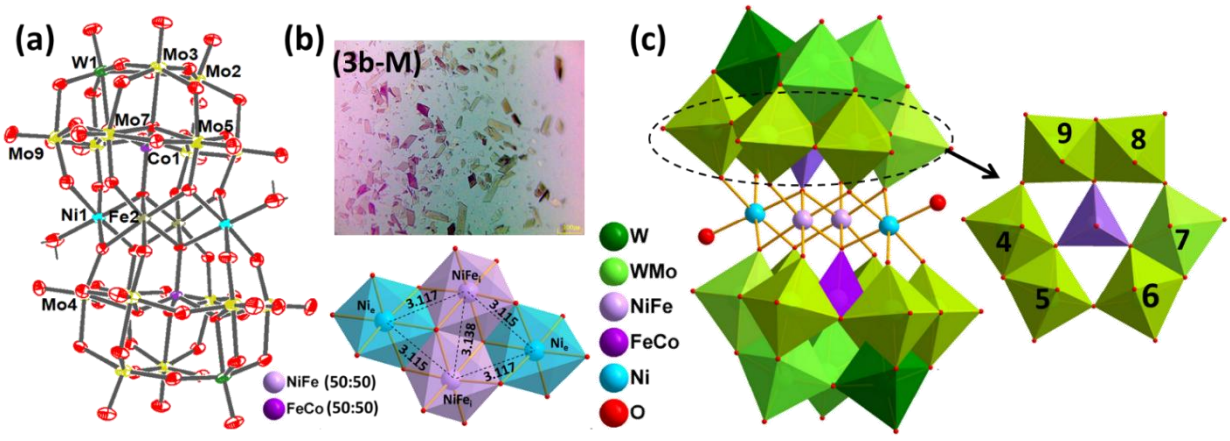

Figure S80. (a) ORTEP drawing (with 60% ellipsoid probability) (b) Optical images and Cubane core showing the interatomic distance between transition metals in **3b-M** (c) combined polyhedral/ball and stick representation of the single-crystal X-ray structure of polyoxometalate **3b-M.** Countercations and hydrogen atoms are omitted for clarity; belt 2 depicts different ratios of Mo to W in **3b-M.** Countercations and hydrogen atoms are omitted for clarity.

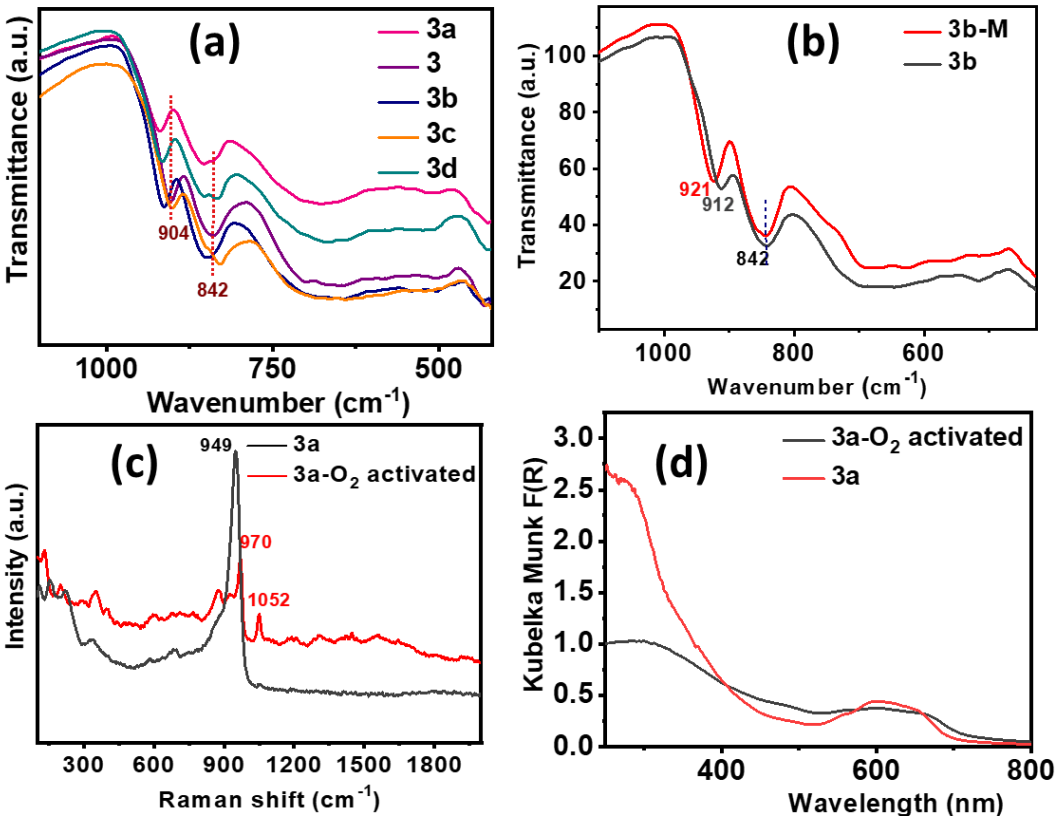

Figure S81. (a) FT-IR spectra of **3a/3/3b/3c/3d** showing the impact of external transition metal substitution in terms of shifting from parent **3**; (b) shift in FT-IR indicating Mo-doping in **3b** and **3b-M**, and (c) Raman spectra and (d) corresponding UV-vis spectra of **3a** before and after dioxygen activation.

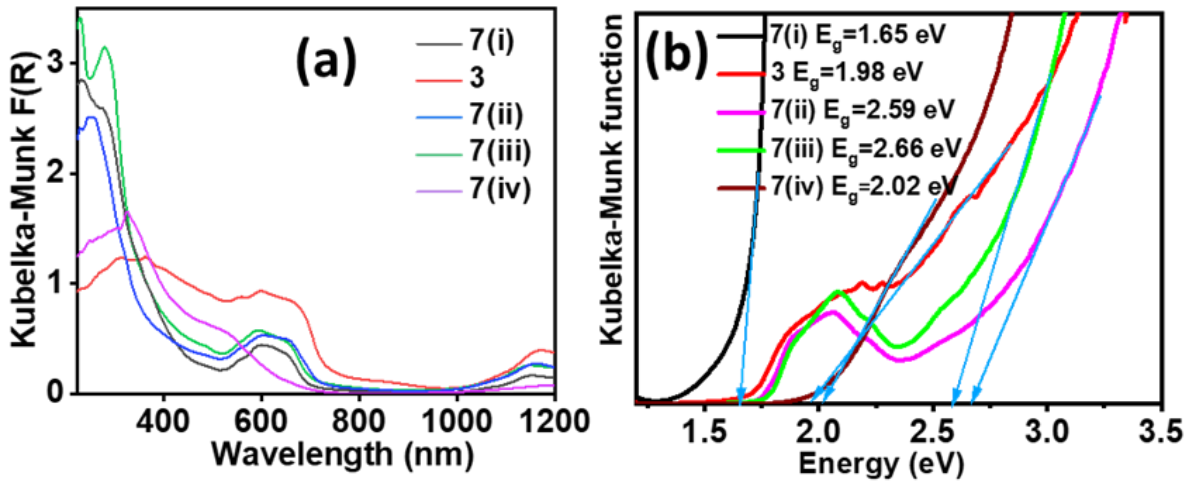

Figure S82. (a) solid-state UV-vis spectra and (b) optical band-gap shifting derived from the Kubelka-Munk equation in **3a/3/3b/3c/3d.**

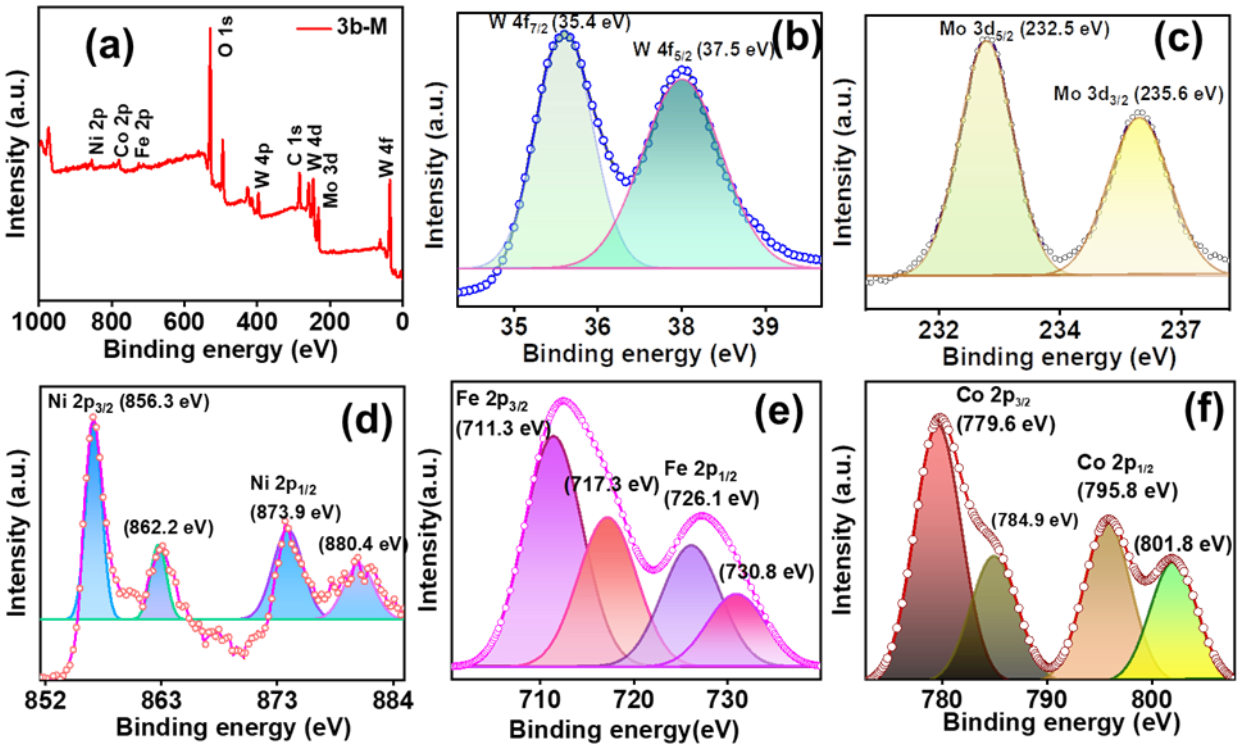

Figure S83. XP spectra of **3b-M** (a) Survey spectra, (b) W 4f, (c) Mo 3d, (d) Ni 2p, (e) Fe 2p, and (f) Co 2p.

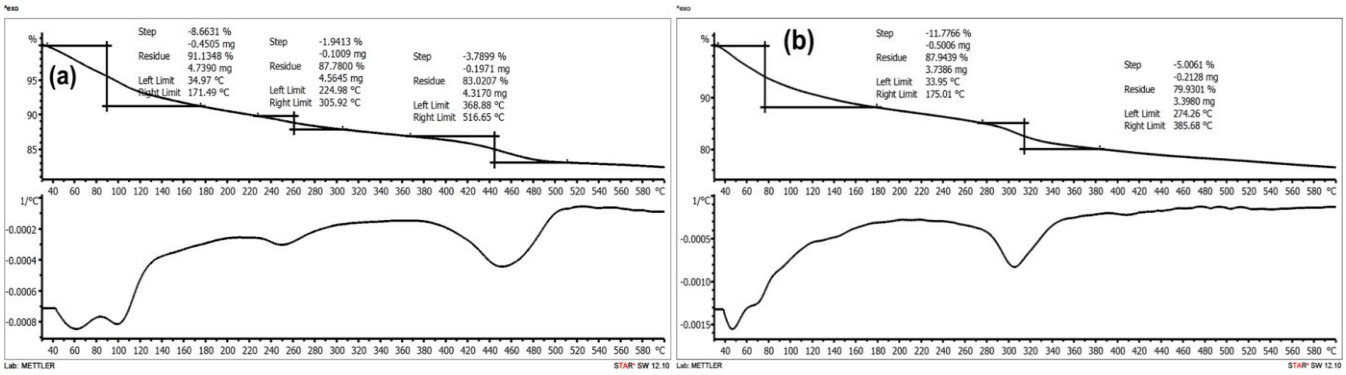

Figure S84. TGA curve along with the corresponding first derivative of (a) **3c**, (b) **3b-M**.

Characterizations analysis of 3a/3b/3c and 3b-M

Compounds **3a/3b/3c/3d** and **3b-M** were characterized using SC-XRD, FT-IR, ESI-MS, XPS, and UV-visible spectroscopy (Figure S74-S84). The framework structure was confirmed by SC-XRD (**CCDC 2330249, 2330250)** for **3b, 3c,** and **3b-M.** 3b crystallize in triclinic lattice with $P\bar{1}$ space group while its analog mixed addenda **3b-M** crystallizes in monoclinic lattice with $P2_1/n$ space group (Table S30). The 3D SC-XRD structure of **3b, 3c,** and **3b-M** shows that the trilacunary Keggin moiety contains a tetrahedrally bound Co atom in the center as a templating agent to triads of addenda W/Mo atoms. The tetrasubstituted sandwich core consists of Fe at internal $\{TM_i\}$ position and Ni as external atoms $\{TM_e\}$ in **3b, 3b-M**, while in **3c,** Fe at internal position and Cu as external atoms (Figures S74, S80). The optical image shows that the substitution of external transition metals in **3** completely changes the size and shape of the crystals (Figure S77).

All these POMs (**3a**/**3b**/**3c**/**3d**) show similar IR patterns to the parent **3** because of their similar structural geometry. The characteristic W = O_t (904 cm^{-1}) and W-O_c-W (842 cm^{-1}) bond stretching frequencies of **3** remain almost identical even after substitution of first-row transition-metal atoms, as shown in Figure S81a. The ESI-MS spectrum of the parent **3** shows one envelope of peaks at a *m*/*z* of 1585.17 assigned for a $\{H_{11}[Co_2Fe_2(CoW_9O_{34})_2]^{3-}$ cluster anion. Transition metal substitutes analogs of **3** show the envelope of peaks at m/z 1587.51 for $\{H_{11}[Cu_2Fe_2(CoW_9O_{34})_2]^{3-}$, 1585.14 for $\{H_{11}[Ni_2Fe_2(ZnW_9O_{34})_2]^{3-}$, and 1583.51 for $\{H_{11}[Mn_2Fe_2(ZnW_9O_{34})_2]^{3-}$ (Figure S75/S76, Table S32). The most abundant anion in **3b-M** has a composition without Mo addenda in the formula, i.e., the formation of **2c** dominates the synthesis of **2c-M**. ESI-mass spectrum of **3** in shows the envelope of peaks at m/z 1585 (z= –3) while the analog mixed addenda POMs structure shows the isotopic multiple envelopes of peaks attributed to varying ratios of molybdenum to tungsten. The mixed addenda sandwich POMs **3b-M** show the envelopes of peaks (Figure S79, Table S33) in the range of *m*/*z* 1370-1490 for $[H_{11}\{Ni_2Fe_2(H_2O)_2(CoMo_xW_{9-x})_2\}^{3-}]$ for z=-3 and *m*/*z* 2100-2300 for $[H_{12}\{Ni_2Fe_2(H_2O)_2(CoMo_xW_{9-x})_2\}^{2-}]$ for z=-2. The most abundant anion in **3-M** has the composition of Mo/W (5:13) with the formula $[H_{10}\{Ni_2Fe_2(H_2O)_2(CoFeMo_5W_{13}O_{68}\}^{3-}]$, while the Mo/W ratio varies from 1:5 to 7:11 with a constant charge of the cluster, i.e., -14. From the comparison of **3b-M** with the reference structure (Figure S1), it is clear that only a small amount of Mo incorporation is favorable at all belt positions, while other positions in the cap do not favor the incorporation of Mo addenda in the tetrasubstituted framework. (Figure S80c). BVS indicates W/Mo in +6, Co, Ni, Cu in +2 and Fe in +3 oxidation state in **3b, 3c** and **3b-M** (Table S31). Apart from the BVS, the oxidation states of all of the atoms in **3b-M** were determined from XPS analysis. The XP spectra of **3b-M** revealed the presence of W, Mo, Fe, Ni, Co, and oxygen (Figure S83). The two peaks at 712.4 and 726.7 eV in **3b-M** can be attributed to the presence of Fe in a +3 oxidation state. The W 4f doublet appears between 35.4 and 37.5 eV, corresponding to W $4f_{7/2}$ and $4f_{5/2}$, and Mo 3d doublet appears between 232.5 and 235.6 eV, corresponding to Mo $3d_{5/2}$ and $3d_{3/2}$, indicating the presence of W/Mo in +6 oxidation state.

In UV-visible spectroscopy, all these POMs show a strong and broad absorption band between 280-350 nm, as expected due to LMCT (O2p to W5d) transitions for CoW_9O_{34} units (Figure S82a). The HOMO-LUMO energy gaps of these TMSP are highly influenced by the substituted transition metals and show shifts in the absorption band, e.g. the LMCT band shifts to a lower wavelength for **3a**/**3b**/**3c**/**3d** than the parent **3**. Similarly, the band gap of **3** and its TM-substituted POMs is remarkably influenced by the substituted TM, and HOMO-LUMO gap increases with the increase in the atomic number of transition metals except for 3d. The trend of the band gap is **3c** > **3b** > **3** > **3a** (Figure S82b). The anomalous behavior of **3d** might be due to competition between Zn and Co to the heteroposition. This increase in band gap was further supported by the DFT study, which indicates that band gap (highest SOMO to LUMO) increases when we go from **3a** to **3d** (Figure S78). Thermal stability was determined by thermogravimetric analysis from 25 to 600 °C (Figure S84). The first weight loss of ~7% was observed in the range of 30-180 °C, which was attributed to the release of water of crystallization. Further, weight loss (<5.5%) was observed in the range of 280-500 °C, which is attributed to the release of water molecules coordinated to the counter cations outside the POM framework.

Characterizations of 4a and 4a-M.

Table S34. Crystal data, data collection, and refinement parameters for **4a**	
	4a
CCDC number	**2330246**
empirical formula	$Fe_{3.2}Na_{24}O_{216}W_{36.8}Zn_6Mn_2$
formula weight	11454.26
temp (K)	273.15
crystal system	monoclinic
space group	$P2_1/n$
unit cell dimension	
a (Å)	13.1455(17)
b (Å)	17.670(3)
c (Å)	21.115(4)
α (deg)	90
β (deg)	93.528(5)
γ (deg)	90
V (Å^3)	4895.2(13)
Z	1
ρ (calculated) (g/cm^3)	3.885
μ/mm^{-1}	22.770
F (000)	5028.0
crystal size (mm^3)	0.24 × 0.13 × 0.05
2Θ range for data collection/°	3.87 to 52.89
index ranges	$-16 \le h \le 16$, $-22 \le k \le 22$, $-26 \le l \le 26$
no. of reflection collected /unique	45968/10054
GOF on F^2	1.053
R(int)	0.080
final *R* indices ($I > 2\sigma(I)$)	$R_1 = 0.0424$, $wR_2 = 0.0951$
R indices (all data)	$R_1 = 0.0665$, $wR_2 = 0.1077$
data/restraints/param	10054/0/659
Largest diff. peak/hole / e Å^{-3}	2.85/-1.79

Table S35. BVS calculated from the SC-XRD structure of sandwich POMs in **4a**			
POMs	Transition metal	Bond valence sum value	Oxidation state
4a	W	6.17	+6
	Mn1	3.25	+3
	Fe2	2.37	+2
	Zn1	2.35	+2

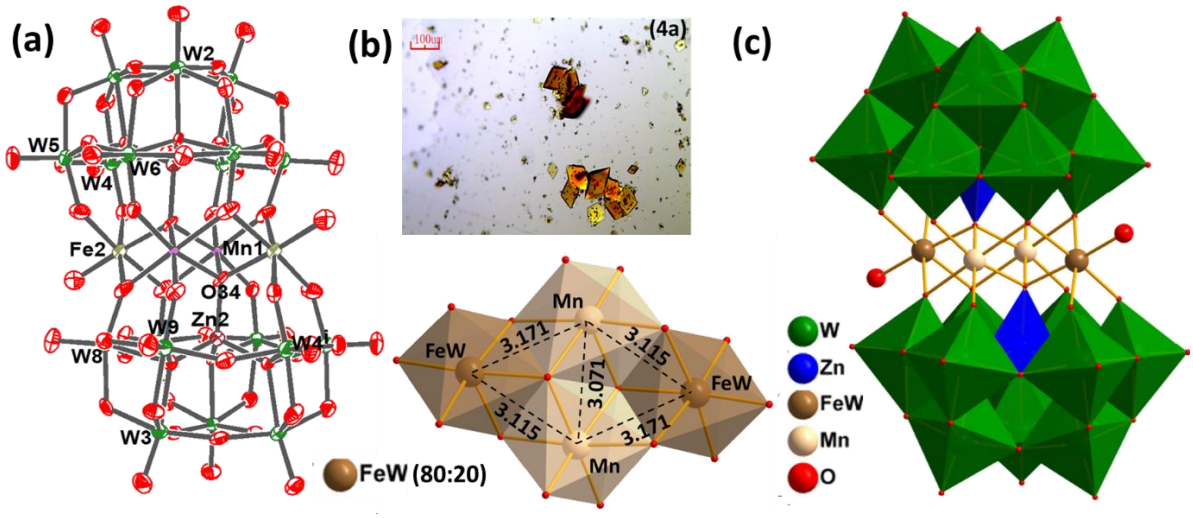

Figure S85. (a) ORTEP drawing (with 60% ellipsoid probability) (b) Optical images and Cubane core showing the interatomic distance between transition metals in **4a** (c) combined polyhedral/ball and stick representation of the single-crystal X-ray structure of polyoxometalate **4a.** Countercations and hydrogen atoms are omitted for clarity.

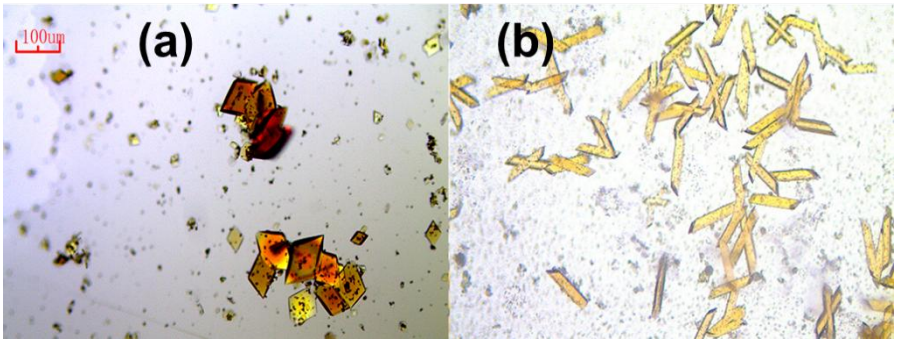

Figure S86. Optical images of sandwich POMs; (a) **4a** and (b) **4a-M**.

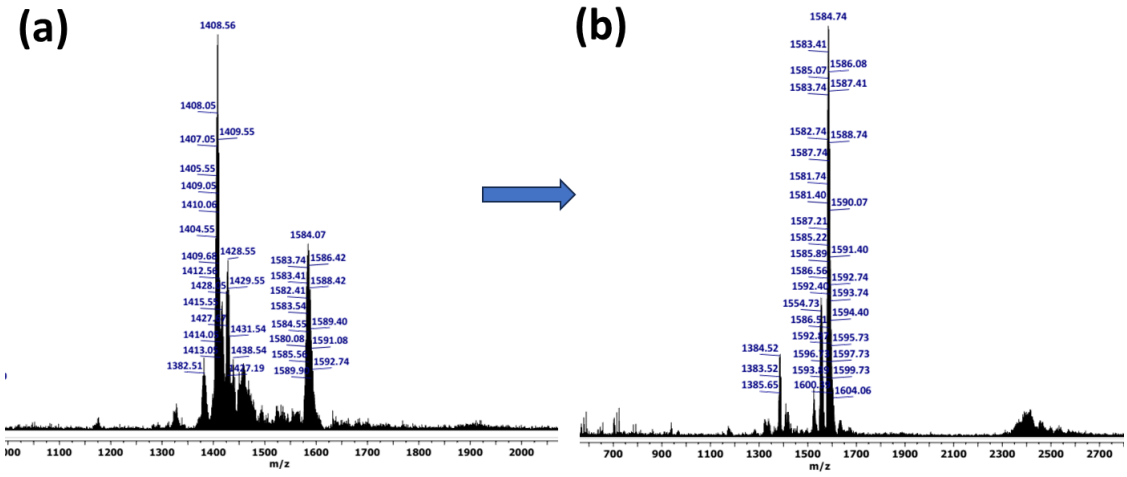

Figure S87. ESI-MS spectra of (a) **4a** (b) **4a-M** in the range of m/z 1000-2700 (z = –3).

Table S36. Assignment of ESI-mass peaks of **4a/4a-M**

Charge	m/z (obs.)	m/z (calc.)	Mol. Wt.	Assigned probable formula
-3	1584.07	1583.46	4750.40	$H_{11}Mn_2Fe_2(ZnFeW_{18}O_{68})$
-3	1554.73	1554.45	4663.36	$H_{11}Mn_2Fe_2(ZnFeMoW_{17}O_{68})$

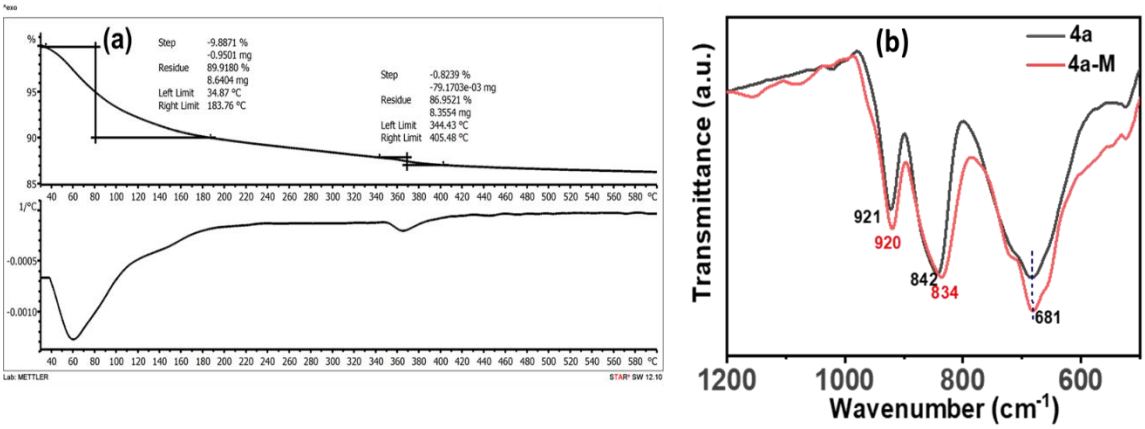

Figure S88. (a) TGA curve along with corresponding first derivative of **4a** (b) and effect of molybdenum incorporation in the framework of tetrasubstituted sandwich POMs in terms of shifting of characteristic peaks in FT-IR of **4a** and **4a-M.**

Characterization analysis of 4a and 4a-M

Compounds **4a** and **4a-M** were characterized using SC-XRD, FT-IR, and ESI-MS (Figure S85-S87). The framework structure of **4a** was confirmed by SC-XRD (**CCDC 2330246)** (Table S34), however, crystals of **4a-M** give poor diffractions. The dark orange-colored octahedral crystals (Figure S86b) of **4a** crystallize in monoclinic with $P2_1/n$ space group. The 3D SC-XRD structure of **4a** shows that the trilacunary Keggin moiety contains a tetrahedrally bound zinc atom in the center as a templating agent to triads of addenda W atoms. The tetrasubstituted sandwich core consists of Mn at the internal $\{TM_i\}$ position and Fe/W (80:20) as external atoms $\{TM_e\}$. The distance between Fe/W atoms at the external and Mn at the internal positions is 3.11-3.17 Å, however, the distance between Mn atoms in the internal positions is 3.07 Å in **4**a (Figure S79a/S79c). BVS calculation indicates that all addenda atoms are in their highest oxidation state (+6) and Zn, Fe, Mn in +2, +2 and +3 oxidation states, respectively (Table S35).

The FT-IR spectra of **4a** show the characteristics peaks at 921 cm^{-1} ($W{=}O_{term}$), 842, 681 cm^{-1} (W-O-W) cm^{-1} while **4a-M** show the characteristics peaks at 920 cm^{-1} ($M{=}O_{term}$), 834, 681 cm^{-1} (M-O-M) cm^{-1} (Figure S88b) with slight shifting thus indicating very less Mo incorporation in the framework which was further confirmed in ESI-MS. The ESI-MS spectrum of the parent **4a** shows one envelope of peaks at a *m/z* of 1584.07 assigned for a $\{H_{11}[Fe_2Mn_2(ZnW_9O_{34})_2]^{3-}$ cluster anion. The analogue mixed addenda **4a-M** shows the envelopes of peaks (Figure S87) for the most abundant anion at *m/z* 1584.74 for $\{H_{11}[Fe_2Mn_2(ZnFeW_{18}O_{68})]^{3-}$ cluster anion, thus indicating equal probability for Zn and Fe at heteroposition, which was also observed in **2-M** and **3-M**. The highest Mo/W ratio in **4a-M** was found to be 2:16 with z=-3 and further pH variation does not improve the Mo/W ratio. Thermal stability was determined by TGA analysis from 30 to 600 °C (Figure S88). The TGA curve

of **4a** shows high thermal stability up to 600 °C. The first weight loss was observed in the range of 30-180 °C, which was attributed to the release of water of crystallization. The small weight loss in 340-380 °C range are attributed to the release of water molecules coordinated to the counter cations outside the POM framework.

Table S37. Inductively coupled plasma mass spectrometry (ICP-MS) data for mixed addenda sandwich POMs

1-M	W%	Mo%	Fe%		Na%	K%
	50.05	7.51	6.56		4.05	2.68
2-M	W%	Mo%	Fe%	Zn%	Na%	K%
	51.23	5.56	3.03	4.89	5.87	1.91
3-M	W%	Mo%	Fe%	Co%	Na%	
	55.55	3.99	2.32	4.45	6.72	
4-M	W%	Mo%	Mn%	Zn%	Na%	
	58.03	0.73	2.07	3.70	6.59	
5-M	W%	Mo%	Mn%	Co%	Na%	
	57.82	1.60	2.04	5.02	6.51	

Table S37a. Bulk composition formula obtained from ICP-MS and comparison with formula from SC-XRD

POM Composition	For ICP-MS	For SC-XRD
$Na_{10}[Fe_4(H_2O)_2(FeMo_xW_{9-x}O_{34})_2].20H_2O$ (**1-M**)	$Na_9K_{3.4}Fe_6Mo_4W_{14}O_{68}$ $(22H_2O)$	$Fe_6K_4Mo_{3.4}Na_{10}O_{98}W_{14.6}$
$Na_{14}[Zn_2Fe_2^{+3}(H_2O)_2(ZnMo_xW_{9-x}O_{34})_2].23H_2O$ (**2-M**)	$Na_{14}K_{2.6}Fe_{2.9}Zn_4Mo_{3.1}W_{14.9}O_{68}$ $(25H_2O)$	$Fe_6H_{56}K_4Mo_{5.4}Na_{24}O_{196}W_{30.6}Zn_6$
$Na_{14}[Co_2Fe_2^{+3}(H_2O)_2(CoMo_xW_{9-x}O_{34})_2].19H_2O$ (**3-M**)	$Na_{15.5}Co_4Fe_{2.2}Mo_{2.2}W_{16}O_{68}$ $(21H_2O)$	$Co_4Fe_2Mo_{2.84}Na_{13}O_{109}W_{15.16}$
$Na_{14}[Zn_2Mn_2^{+3}(H_2O)_2(ZnMo_xW_{9-x}O_{34})_2].22H_2O$ (**4-M**)	$Na_{15}Mn_2Zn_3Mo_{0.4}W_{17.4}O_{68}$ $(24H_2O)$	$Mn_2Mo_{0.24}Na_{15}O_{104}W_{18.16}Zn_{3.6}$
$Na_{14}[Co_2Mn_2^{+3}(H_2O)_2(CoMo_xW_{9-x}O_{34})_2].19H_2O$ (**5-M**)	$Na_{15.2}Mn_2Co_{4.6}Mo_{0.9}W_{17.6}O_{68}$ $(21H_2O)$	$Co_{3.8}Mn_2Mo_{0.4}Na_{13}O_{108}W_{17.8}$

Electrochemistry of sandwich POMs (2 and 2-M)

Cyclic voltammetry (CV) for POM **2**/**2-M** was performed in an aqueous solution at pH 2.5, as these POMs do not show redox peaks at pH > 5.5, and only a few feeble peaks were observed at pH 3.0. At lower pH (typically pH < 1.5), these POMs show hydrogen evolution potential due to proton-coupled electron transfer. Hence, all electrochemical studies were performed at pH 2.5, where **2**/**2-M** POMs show mostly quasi-reversible redox characteristics (Figure 6a,b). These POMs exhibit quasi-reversible redox couples in CV, characterized by their half-wave potentials ($E_{1/2}$) and peak separations ($\Delta E_p=|E_{pc} - E_{pa}|$) (Figure 6a,b, Table S38). The CV of **2** shows quasi-reversible redox peaks of W, mainly on the negative side, while the 3d transition metals at the sandwich

position show quasi-reversible peaks toward the positive side vs Ag/AgCl/3 M KCl. In mixed addenda analogues, it is difficult to designate the peaks of Mo and W due to the similar redox potentials of Mo/W as well as the presence of several variables. The only way to assign Mo peaks is to compare the cyclic voltammogram of W-only POMs (**2**) with that of mixed addenda (**2-M**), where all other variables are the same except Mo.

Table S38. Cyclic voltammetry data of **2** and **2-M**, (pH 2.5).

Mixed addenda POMs **(2-M)**		W-only POMs **(2)**	
3d TMs $E_{1/2}$ [V]	**W/Mo peaks** $E_{1/2}$ (ΔE_p) [V] [mV]	**3d TMs** $E_{1/2}$ [V]	**W peaks** $E_{1/2}$ (ΔE_p) [V] [mV]
0.87[a], 0.78[a]	-1.37 (106), -1.33[b], -1.02 (61), -0.65 (90), -0.54[b], -0.27 (145*), 0.02 (160*), 0.13 (62)	1.08[a], 0.83[a],	-1.40 (61), -1.18 (68), -0.92 (109), -0.61 (61), -0.48 (66), -0.31 (62)

[a]values refer to E_{pa}, [b]values refer to E_{pc} *faint peaks, possible merge of two peaks

References.

1. Brown, I. D.; Altermatt, D., Bond-valence parameters obtained from a systematic analysis of the inorganic crystal structure database. *Acta. Crystallogr. B. Struct. Sci. Cryst. Eng.* 1985**, 41** (4), 244-247.
2. Zheng, S.-T.; Yang, G.-Y., Recent advances in paramagnetic-TM-substituted polyoxometalates (TM= Mn, Fe, Co, Ni, Cu). *Chem. Soc. Rev.* 2012**, 41** (22), 7623-7646.
3. Singh, G.; Mandal, D., Modulation of the Band Gap and Redox Properties by Mixed Addenda in Sandwich Polyoxometalates. *Inorg. Chem.* 2023**, 62** (48), 19648-19663.
4. Zhao, J.-W.; Zheng, S.-T.; Yang, G.-Y., Hydrothermal synthesis and structural characterization of three inorganic–organic composite sandwich-type phosphotungstates. *J. Solid State Chem.* 2007**, *180*** (12), 3317-3324.
5. Chai, D.-F.; Ma, Z.; Yan, H.; Qiu, Y.; Liu, H.; Guo, H.-D.; Gao, G.-G., Synergistic effect of sandwich polyoxometalates and copper–imidazole complexes for enhancing the peroxidase-like activity. *RSC Adv.* 2015**, 5** (96), 78771-78779.